Alluvial Stratigraphic Response to Astronomical Climate Change
Numerical modelling and outcrop study in the Bighorn Basin, Wyoming, USA

Wang, Y.

Important note
To cite this publication, please use the final published version (if applicable).
Please check the document version above.

Alluvial Stratigraphic Response to Astronomical Climate Change

Numerical modelling and outcrop study in the Bighorn Basin, Wyoming, USA

Alluvial Stratigraphic Response to Astronomical Climate Change

Numerical modelling and outcrop study in the Bighorn Basin, Wyoming, USA

Dissertation

for the purpose of obtaining the degree of doctor
at Delft University of Technology,
by the authority of the Rector Magnificus prof. dr. ir. T.H.J.J. van der Hagen,
Chair of the Board for Doctorates,
to be defended publicly on
Thursday 28 October 2021 at 15.00 o'clock

by

Youwei WANG

Master of Engineering in Geological Resources and Geological Engineering,
China University of Petroleum (Beijing), China
born in Weihai, China.

This dissertation has been approved by the promotor and the copromotor.

Promotor: Prof. dr. A.W. Martinius
Copromotor: Dr. H.A. Abels

Composition of the doctoral committee:

Rector Magnificus,	Chairman
Prof. dr. A.W. Martinius,	Delft University of Technology/Equinor
Dr. H.A. Abels,	Delft University of Technology

Independent members:

Prof. dr. G. Bertotti,	Delft University of Technology
Prof. dr. G.J. Hampson,	Imperial College London
Prof. dr. C.R. Fielding,	University of Connecticut
Prof. dr. K.F. Kuiper,	Vrije Universiteit Amsterdam
Dr. E. Stouthamer,	Utrecht University

Reserved member:

Prof. dr. E.C. Slob,	Delft University of Technology

Dr. J.E.A. Storms has, as supervisor, contributed significantly to the preparation of this dissertation.

To my parents, sister, and girlfriend.

Contents

Summary

Alluvial stratigraphy is influenced by both allogenic and autogenic factors, which are difficult to be distinguished from each other because they operate at overlapping spatial and temporal scales. Moreover, it remains uncertain whether autogenic dynamics can result in sedimentary cyclicity that resembles allogenically-driven stratigraphic products. In order to undertake this challenge and address the uncertainty, we first test what sedimentary processes can produce the alluvial cyclicity observed in outcrops by designing comparable scenarios in the process-based numerical modelling. In the meantime, we systematically characterize floodplain aggradation cycles, channelized sandstone bodies, and the configurative stratigraphic relationships between them by detailed outcrop analysis.

In Chapter 2, we design several numerical modelling scenarios to mimic the possible inputs at the basin inlet to observe how the alluvial sedimentation responds to changes in boundary conditions. Specifically, we vary the amplitude and wavelength of water discharge (Q_w) and sediment supply (Q_s) that are defined to be cyclic. We find cyclic alluvial stratigraphic patterns to occur when the Q_s/Q_w ratio has sufficiently large amplitudes and long, but not very long, wavelengths. Each alluvial stratigraphic cycle consists of two phases: an aggradation phase characterized by rapid sedimentation due to frequent channel shifting and a non-deposition phase characterized by channel belt stability and, depending on Q_s/Q_w amplitudes, incision. Larger Q_s/Q_w ratio amplitudes contribute to weaker downstream signal shredding by stochastic components in the model. Floodplain topographic differences are found to be compensated by autogenic dynamics at certain compensational timescales in fully autogenic runs, while the presence of allogenic forcing clearly impacts the compensational stacking patterns.

Based on the findings gained in the numerical modelling work, we extend our investigations into outcrops that are digitally mapped by UAV-based photogrammetry substantiated by detailed sedimentary logs produced in trenched sections (Chapter 3). The stratigraphy with an accumulative thickness of 300 m contains a total of 44 cycles with an average thickness of 6.8 m. Most cycles are consistently traceable over the entire photogrammetric model, indicating spatial consistency and in line with allogenic climate forcing by the astronomical precession cycle. Individual floodplain aggradation cycles may change in thickness rapidly when traced laterally, with rates up to 1 m over a lateral distance of 100 m and a maximum of 4 m. Detailed mapping of seven successive cycles reveals differences in their regionally-averaged thicknesses of 3.7 m to 9.7 m, with their coefficients of variation ranging between 17% and 28%. Variogram analysis demonstrates that the thickness of a cycle at one locality is statistically related to that at another locality over an average distance of 1.3 km in the paleoflow direction and 0.6 km perpendicular to the paleoflow direction. These different directional trends are interpreted to result from morphological elements oriented in paleoflow directions in the fluvial landscapes shaping more consistency of the sedimentary elements in paleoflow direction. Two different metrics suggest that full compensational stacking occurs after deposition of 6 to 7 cycles, or timescales

of ca. 120 to 140 kyr, although strong thickness compensation is shown to start at the subsequent one and two floodplain aggradation cycles, so at 40-60 kyr time scales.

In Chapter 4, a total of 92 channelized sandstone bodies are documented in the field and in the georeferenced UAV photogrammetric model. Channelized sandstone bodies are interpreted to be sedimentary products of four planform styles of rivers based on detailed sedimentological descriptions: crevasse channel, massive trunk-shaped channel, braided channel, and sinuous channel, with the latter two styles more abundant. Braided and sinuous channel sandstone bodies differ significantly in the thickness (on average 6.1 m vs 9.0 m) according to the t-test results. Meanwhile, they differ insignificantly in the width (on average 231 m) and in paleoflow directions (on average 3°N). Frequent alternations between braided and sinuous rivers are seen and reveal no spatial dependence. Based on results of previous studies and observation in this study, the changing river styles are attributed to axial and transverse fluvial systems mixing their influences in the central segment of the basin under study.

Next, we combine the floodplain and sandstone body data to investigate possible links between fluvial styles and climatically-controlled floodplain stratigraphy (Chapter 5). We find that braided and sinuous channels occur in different stratigraphic positions. Sinuous channels are initiated at the end of the avulsion phase and continue growing through the whole overbank phase until the next avulsion phase starts. In contrast, braided channels are initiated in the avulsion phase and stopped before the overbank phase starts. Moreover, a dominant sinuous channel interval is found to relate to the eccentricity maxima in the proxy curve of marine records, while a dominant braided channel interval is seen to relate to the eccentricity minima in that curve. These phenomena are attributed to impacts of eccentricity-modulated precession. The genetic links between river style and orbital climate forcing provide important predictive values for exploring and exploiting subsurface resources in orbitally-forced alluvial basins.

In Chapter 6, we synthesize the data, analysis, and interpretations gained in this dissertation, and we propose lines of future research and possible applications of the findings in related fields. Particularly, the more extensive study of orbital forcing in a source-to-sink perspective will be an important subject of future research.

Samenvatting

Alluviale stratigrafie wordt beïnvloed door zowel allogene als autogene factoren, die moeilijk van elkaar te onderscheiden zijn, omdat ze op overlappende ruimtelijke en temporele schalen werken. Bovendien blijft het onzeker of autogene dynamiek kan resulteren in sedimentaire cycliciteit die lijkt op allogeen aangedreven stratigrafische producten. Om deze uitdaging aan te gaan en de onzekerheid aan te pakken, testen we eerst welke sedimentaire processen de alluviale cycliciteit kunnen produceren die wordt waargenomen in ontsluitingen door vergelijkbare scenario's te ontwerpen in proces-gebaseerde numerieke modellering. In de tussentijd karakteriseren we systematisch de agggradatiecycli van uiterwaarden, gekanaliseerde zandsteenlichamen en hun stratigrafische relaties door gedetailleerde analyse van ontsluitingen in de Verenigde Staten van Amerika.

In Hoofdstuk 2 ontwerpen we verschillende numerieke modelleringsscenario's om de mogelijke inputs bij de bekkeninlaat na te bootsen om te observeren hoe de alluviale sedimentatie reageert op veranderingen in randvoorwaarden. In het bijzonder variëren we de amplitude en golflengte van waterafvoer (Q_w) en sedimenttoevoer (Q_w) die als cyclisch zijn gedefinieerd. We vinden met dit onderzoek dat cyclische alluviale stratigrafische patronen optreden wanneer de Q_s/Q_w-verhouding voldoende grote amplitudes en lange, maar niet erg lange golflengtes heeft. Elke alluviale stratigrafische cyclus bestaat uit twee fasen: een aggregatiefase die wordt gekenmerkt door snelle sedimentatie als gevolg van frequente kanaalverschuivingen en een fase die wordt gekenmerkt door stabiliteit van de kanalen en, afhankelijk van Q_s/Q_w-amplitudes, gekenmerkt door weinig sedimentatie of incisie. Grotere Q_s/Q_w-verhoudingsamplitudes dragen bij aan sterker stroomafwaarts voortzetten van bovenstroomse signalen door stochastische componenten in het model. Topografische verschillen in overstromingsvlakten blijken te worden gecompenseerd door autogene dynamiek op bepaalde, langere tijdschalen in volledig autogene runs, terwijl de aanwezigheid van allogene forcering duidelijk deze tijdschalen van topografische compensatie beïnvloedt.

Gebaseerd op de bevindingen die zijn opgedaan in het numerieke modelleringswerk, breiden we ons onderzoek uit naar ontsluitingen die digitaal in kaart zijn gebracht door UAV-gebaseerde fotogrammetrie, onderbouwd door gedetailleerde sedimentaire logs geproduceerd in het veld (Hoofdstuk 3). De stratigrafie met een cumulatieve dikte van 300 m bevat in totaal 44 overstromingsvlakte agradatie cycli met een gemiddelde dikte van 6,8 m. De meeste cycli zijn consistent traceerbaar over het gehele fotogrammetrische model, wat wijst op ruimtelijke consistentie wat in lijn is met allogene klimaatforcering door de astronomische precessiecyclus. Afzonderlijke sedimentaire cycli op de uiterwaarden kunnen snel in dikte veranderen wanneer ze lateraal worden gevolgd, met snelheden tot 1 m over een zijafstand van 100 m en maximaal 4 m. Gedetailleerde kartering van zeven opeenvolgende cycli onthult verschillen in hun regionaal gemiddelde diktes van 3,7 m tot 9,7 m, met hun variatiecoëfficiënten tussen 17% en 28%. Variogramanalyse toont aan dat de dikte van een cyclus op de ene plaats statistisch gerelateerd is aan die op een andere plaats

over een gemiddelde afstand van 1,3 km in de paleostroomrichting en 0,6 km loodrecht op de paleostroomrichting. Deze verschillende richtingstrends worden geïnterpreteerd als het resultaat van morfologische elementen die zijn georiënteerd in paleostromingsrichtingen in de rivierlandschappen, waardoor meer consistentie van de sedimentaire elementen in paleostromingsrichting wordt gevormd. Twee verschillende statistieken suggereren dat volledige compensatie van topografische verschillen tussen verschillende plekken optreedt na depositie van 6 tot 7 cycli, of op tijdschalen van ca. 120 tot 140 duizend jaar, hoewel we ook aantonen dat sterke diktecompensatie begint bij de opeenvolgende sedimentaire cyclus dus op tijdschalen van 40-60 duizend jaar.

In Hoofdstuk 4 worden in totaal 92 gekanaliseerde zandsteenlichamen gedocumenteerd in het veld en in het gegeorefereerde UAV-fotogrammetrische model. Gekanaliseerde zandsteenlichamen worden geïnterpreteerd als sedimentaire producten van vier rivierstijlen op basis van gedetailleerde sedimentologische beschrijvingen, waarbij de gevlochten kanalen en meanderende kanalen het meest voorkomen. Gevlochten en meanderende zandsteenlichamen verschillen aanzienlijk in dikte (gemiddeld 6,1 m versus 9,0 m) volgens de t-testresultaten. Ondertussen verschillen ze onbeduidend in de breedte (gemiddeld 231 m) en in paleostroomrichtingen (gemiddeld 3°N). Frequente afwisselingen tussen gevlochten en bochtige rivieren worden gezien en onthullen geen ruimtelijke afhankelijkheid. Op basis van resultaten van eerdere studies en observaties in deze studie, worden de veranderende rivierstijlen toegeschreven aan axiale en transversale riviersystemen in het bestudeerde bekken die hun invloeden vermengen in het centrale segment van het stroomgebied.

Vervolgens combineren we de gegevens over uiterwaarden en zandstenen om mogelijke verbanden tussen rivierstromingen en klimaatgecontroleerde stratigrafie van uiterwaarden te onderzoeken (Hoofdstuk 5). We vinden dat gevlochten en bochtige kanalen voorkomen in verschillende stratigrafische posities. Bochtige kanalen worden gestart aan het einde van de avulsiefase en blijven groeien gedurende de hele overbankfase totdat de volgende avulsiefase begint. Daarentegen worden gevlochten kanalen gestart in de avulsiefase en gestopt voordat de overbankfase begint. Bovendien blijkt een dominant bochtig kanaalinterval verband te houden met de excentriciteitsmaxima in de proxycurve van mariene records, terwijl een dominant gevlochten kanaalinterval verband houdt met de excentriciteitsminima in die curve. Deze verschijnselen worden toegeschreven aan effecten van excentriciteit-gemoduleerde precessie. De genetische verbanden tussen rivierstijl en orbitale klimaatforcering bieden belangrijke voorspellende waarden voor het verkennen en exploiteren van ondergrondse hulpbronnen in alluviale bekkens.

In Hoofdstuk 6 synthetiseren we de gegevens, analyses en interpretaties die in dit proefschrift zijn verkregen, en stellen we lijnen voor toekomstig onderzoek en mogelijke toepassingen van de bevindingen in verwante gebieden voor. Vooral de meer uitgebreide studie van orbitale forcering in een source-to-sink perspectief zal een belangrijk onderwerp zijn voor toekomstig onderzoek.

1

Introduction and hypothesis

In this chapter, we first introduce the general topics of the dissertation, then present scientific questions that are of our interest, and eventually develop ideas and methodologies to seek answers to these questions.

1

1.1 Introduction

1.1.1 Alluvial stratigraphic records

Alluvial stratigraphic records are notoriously vulnerable to stratigraphic incompleteness (Figure 1.1) (Foreman and Straub, 2017), which has been referred to as "Sadler effect" (Sadler, 1981). This phenomenon results from frequently occurring periods of erosion and non-deposition in geological time. Consequently, alluvial stratigraphic records are much more incomplete and bear more gaps than their marine counterparts (Hilgen et al., 2015). In this context, it is challenging to extract the imprint of a certain event from the rock records. As a countermeasure, stratigraphic analysis can be implemented at certain timescales depending on the area of investigation, where the stratigraphic record can be regarded as pseudo-complete (Miall et al., 2021). This renders it difficult to properly allocate time distribution in the alluvial stratigraphy.
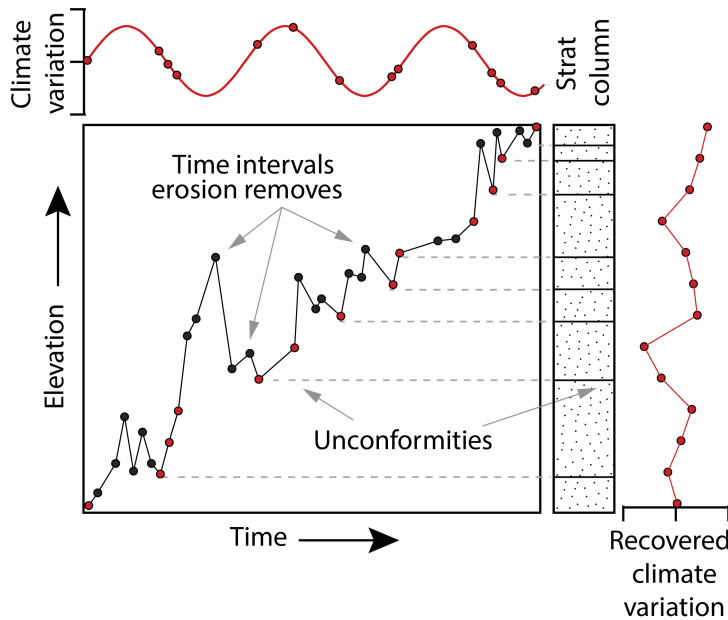
Figure 1.1: Construction of stratigraphic column from individual depositional and erosional events of varying magnitudes and rates (reproduced from Foreman and Straub (2017), with all rights reserved). Red circles are time periods represented in the recovered climate change record (the very right panel), while black circles stand for time intervals whose deposits are later reworked and thus not represented in the recovered climate change record.

Moreover, alluvial sedimentation responds to various autogenic and allogenic forcings (Box 1) and thus the corresponding stratigraphic record is a mixture of autogenic and allogenic imprints operating at different spatial and time scales. Specifically, deposition over a short time scale ($<10^3$ years) is more impacted by local topography and hydrodynamics, which are highly stochastic (Sheets et al., 2002). In contrast, longer-time scale deposition is more controlled by basin subsidence and/or base level variation (Jerolmack and Paola,

2007; Romans et al., 2016), which contributes to deterministic stratigraphic features (Foreman and Straub, 2017). Efforts to extract the deterministic allogenic forcing from the rock record can in many cases fail due to the presence of the stochastic component, namely autogenic dynamics, including splaying, channel migration, avulsion, bifurcation, overbank flooding, and so on. Nonetheless, success can still be achieved by meeting certain requirements, including persistent regularity in the hierarchical stacking pattern, three-dimensional lateral persistence of the depositional sequences, bracketing of the studied interval by numerical ages, and correspondence of the estimated periodicities to those of the orbital cycles (Miall et al., 2021; Tresch and Strasser, 2011).

> Box 1: Allogenic and autogenic processes
>
> *Autogenic processes*
> Processes that are inherent to the sedimentary system and arise solely as a consequence of the interaction of the components within the system (e.g. progradation or lateral migration of sedimentary bodies, compensational stacking) (Hajek and Straub, 2017). These processes depend on local parameters (e.g. local topography and hydrodynamics), and are thus not regionally persistent (Straub et al., 2009; Tresch and Strasser, 2011).
>
> *Allogenic processes*
> Processes that are driven by factors outside the landscape or sedimentary system (Hajek and Straub, 2017). These factors are commonly referred to as the external boundary conditions (e.g., an event, step change, periodic change, or change in environmental variability) (Romans et al., 2016; Tresch and Strasser, 2011), and they can generate sedimentary products of regional consistency.

1.1.2 Orbital forcing and Milankovitch cycles

Orbital forcing refers to the climatic influence of changes in Earth's axis tilt and orbital plane shape by determining the total amount of sunlight reaching the Earth. In this context, the term "forcing" signifies a physical process that affects the Earth's climate. An important contribution to this field is made by Serbian geophysicist and astronomer Milutin Milanković. He attributed the cyclical variation in the insolation reaching the Earth to variations in precession, obliquity, and eccentricity (see Box 2 and Figure 1.2), and cycles of periods below 400 kyr have been now commonly termed as Milankovitch cycles. Areas on different parts of the earth are differentially influenced by solar radiation. Specifically, low-latitude areas are subjected to the impact of eccentricity modulated precession, while high-latitude areas are more influenced by obliquity (Hays et al., 1976).

These astronomical solution-based hypotheses are later proven by geological studies in various marine and continental sedimentary systems all over the world (Olsen et al., 1996), due to the availability of continuous records in ice, rock, and deep ocean cores, the development of new dating tools, such as magnetostratigraphy and radiometric dating (Hays et al., 1976), and the advancement of astronomical solution (Laskar et al., 2011). These geological studies significantly help constrain the uncertainties back into the deep geological past.

1
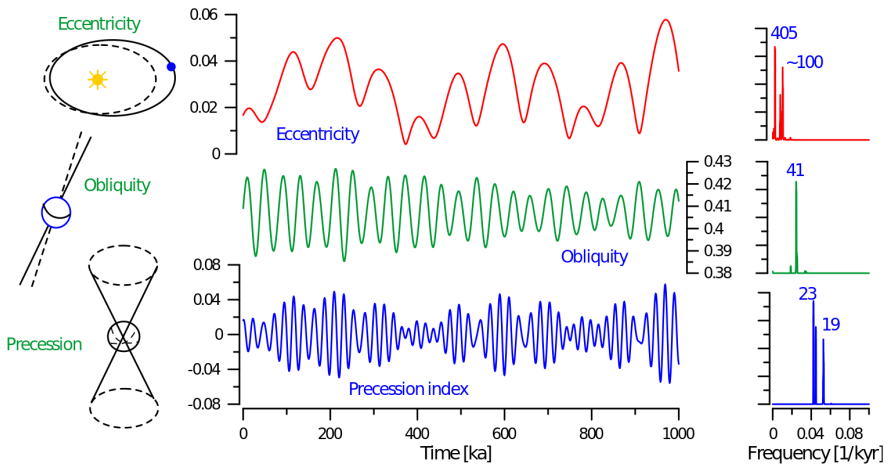
Figure 1.2: Eccentricity, obliquity, precession, and their evolution over the last 1 million year. Source: teaching material on www.cyclostratigraphy.org.

Box 2: Orbital forcing

Precession
Earth's axial precession refers to the slow movement of Earth's rotational axis that depicts a cone, which currently occurs over a full cycle of ca. 26 kyr. In comparison, its perihelion precession refers to the precession of the major axis of Earth's elliptical orbit due to changing gravitational forces exerted by other planets, which combine with the axial precession to work as the "climatic precession" that has an average period of 21.7 kyr at present day becoming shorter back in the geological past (Hays et al., 1976).

Obliquity
Earth's obliquity, also referred to as axial tilt, is the angle between Earth's rotational axis and orbital axis, and it varies between 22.1° and 24.5° over ca. 41 kyr at present day becoming short back in the geological past (Hays et al., 1976). It is currently 23.4° and slowly decreasing in its 41 kyr cycle. Obliquity determines the seasonality and it has the same effect on both hemispheres.

Eccentricity
Earth's orbital eccentricity describes how the Earth's elliptical orbit deviates from a perfect circle over main periods of 100 and 400 kyr (Hays et al., 1976). It modulates precession and determines the seasonality on Earth. Specifically, the precession minimum in the case of a large eccentricity results in hotter summer and colder winter in the northern hemisphere, while conditions are opposite in the southern hemisphere.

1.1.3 Cyclostratigraphy

Cyclostratigraphy aims to investigate cyclic patterns archived in the rock record and thus reconstruct the paleoenvironment that has been influenced by the paleoclimate, which is influenced by the varying solar radiation at the top of the atmosphere (Hilgen, 1991a,b). It generally requires the sedimentary record to be relatively continuous since the sedimentation rate over a certain timescale is commonly assumed to be constant. If the absolute age of the studied interval is known, it is feasible to correlate featured patterns in the rock record with computed astronomical target curves under the precondition that the interval should be relatively young, no older than the Cretaceous-Paleogene boundary for the current astronomical solution (Laskar et al., 2011). In this way, the age resolution can be enhanced to 20-kyr scale, which is much higher than the precision of other dating methods.

There have been many successful case studies that apply cyclostratigraphic analysis in marine and lacustrine realms where sedimentation rate is generally low and relatively continuous (Hilgen, 1991a). However, the application in fluvial successions has been hindered by the complicated response of rivers to autogenic and allogenic forcing, which commonly generate the notorious stratigraphic incompleteness.

1.1.4 Fluvial cyclostratigraphy

Several recent studies demonstrate the feasibility of cyclostratigraphic analysis in fluvial successions. For instance, Abdul Aziz et al. (2008) reveal significant spectral peaks using redness data, and the corresponding cycles closely match the 21 kyr climatic precession cycle. An example of the Paleocene cyclicity is shown in Figure 1.3. Abels et al. (2013) developed a quantitative method, which is termed "soil development index", and based on this index, to differentiate regularly alternating overbank and avulsion cycles with a thickness of 7.1 m that corresponds to an estimated period of ca 21.6 kyr. Noorbergen et al. (2018, 2020) pinpointed the key roles of long- and short-term eccentricity in shaping the fluvial record. However, most of these studies are based on 1-D data, and fail to intuitively reconstruct the fluvial processes that result in these fluvial cycles.

Despite these successes, it is gradually realized that allogenic signals can be destroyed and completely shredded if the sedimentary basin has a very long compensational time scale relative to the allogenic forcing wavelength (Straub et al., 2009). Based on this idea, efforts have been made to calculate the compensational time scale, which is defined as the time needed for a channel to visit every part of a basin and for subsidence to bury the alluvial deposits and prevent them from reworking (Foreman and Straub, 2017). This has been demonstrated to work well in both experimental and field studies (Trampush et al., 2017; Wang et al., 2011). In experimental basins where precise age constraints are available, the basin-scale standard deviation of sedimentation can well describe the spatial landscape heterogeneity, and it presents a power-law decaying trend with longer time intervals averaged (Wang et al., 2011). In contrast, precise age constraints are in many cases not available in the field cases, yet the same power-law decaying trend is still present with thicker stratigraphic intervals averaged (Trampush et al., 2017). After doing this kind of research, we know whether an environmental signal (Box 3) can be distinguished from the background stochastic depositional events, depending on their relative wavelength and amplitude to the compensational timescale (Foreman and Straub, 2017).

Figure 1.3: Fluvial cyclicity and PETM boundary sandstone in the Sand Coulee area. People at the bottom are for scale. Photo credit: Prof. Allard Martinius.

1.2 Hypothesis

Orbital control on alluvial stratigraphic records is difficult to test as a result of above mentioned stratigraphic incompleteness and poor chronostratigraphic age control. However, it is still feasible to separate the allogenic from the autogenic forcing by setting up very strong allogenic signals to imprint the autogenic signatures in the process-based numerical model. Moreover, quantitative measurements should be carried out to characterize the relative importance between allogenic forcing and autogenic variability using the stratigraphic record that has been demonstrated to be orbitally driven. The Bighorn Basin provides an opportunity to investigate this relation. Specifically, we investigate the 3D persistency and variability of the regionally extensive and traceable paleosol layers as the stratigraphic framework, while we also decipher the dynamic information archived in the channelized sandstone bodies as the fillings of the framework. Based on this, we should be able to build a link between paleosols and channelized sandstone bodies by observing their stratigraphic configuration. Finally, we aim to define predictive interactions between orbital forcing and river styles by exploring the stratigraphic organizations of alluvial sediments. Given above hypotheses, four main chapters are presented for corresponding purposes.

1.2.1 Numerical forward modelling

Numerical forward modelling provides an opportunity to "isolate" allogenic from autogenic controls, because we know exactly what we put in as the boundary conditions (see Box 3). In this context, we can expect what we would obtain if there is only allogenic forcing. Meanwhile, there are stochastic components in the numerical model that result in variability, which mimics the role of autogenic factors. The eventual sedimentary product of the numerical modelling therefore reflects the influences of both allogenic and auto-

genic factors when a cyclic boundary condition is acted. In Chapter 2, we explore the alluvial response to cyclic and non-cyclic climate forcing through a processed numerical model developed by Karssenberg and Bridge (2008) by mainly varying the amplitude and wavelength of the main inputs (i.e. water discharge and sediment supply), which are coupled with the constant base level rise that provides accommodation. Then we visualize the fluvial processes that consist of a non-deposition phase with channel belt stability and an aggradation phase with channel belt instability. By varying the amplitude and wavelength, this pattern can become either more striking or more vague, which can be statistically analysed using sedimentation rate as the proxy. It is demonstrated that acted allogenic peaks disappear in the power spectra when the amplitude is too small or the wavelength is too short or too long. In this way, we depict how upstream signals get transmitted or shredded in the downstream propagation. Moreover, we, for the first time, calculated compensational timescales in both autogenic and allogenic scenarios, and observed the interference of allogenic forcing on autogenic dynamics. The generated dataset is rich in many aspects, since it provides various perspectives to look into the field data (Chapter 3 to Chapter 5).

Box 3: Numerical modelling

Boundary condition
Boundary conditions are constraints necessary for the solution of a boundary value problem. In the process-based numerical alluvial modelling context, they could be climate, base level, and tectonic that determine the environmental signal as the model input.

Environmental signal
It is typically defined as changes in the amount of produced, transported, and deposited sediment (Q_s) in response to a change in boundary conditions (Romans et al., 2016).

Signal shredding
Modification or obliteration of an allogenic signal by sediment-transport dynamics in a landscape and/or by dynamics of stratigraphic preservation (Hajek and Straub, 2017; Jerolmack and Paola, 2010).

1.2.2 Importance of floodplain deposits and paleosols

Floodplain deposits and paleosols are important components that can act as the framework of the alluvial architecture, and they should be analysed with the same importance as channel or channel-belt deposits. Their formation carries important signatures of the rivers in terms of channel form and behaviour, and their linkage to the associated channels could be in various forms, determining the 3-D spatial features of the floodplain deposits. In Chapter 3, we extensively map 44 paleosol layers as the precession-driven cycle boundaries in a georeferenced photogrammetric model, followed by detailed statistical analysis. The floodplain aggradation cycles bounded by these paleosol layers exhibit both spatial consistency and variability, which are attributed to the superimposition of allogenic and autogenic forcing. Specifically, allogenic forcing contributes to the high traceability of these cycles in the study area, while autogenic forcing brings variability in the lateral ex-

1

tent. Spatial continuity is suggested to coincide the paleoflow direction using both field data of this chapter and model data of Chapter 2, which reflects the role of fluvial processes in shaping the geometry of the fluvial deposits. Moreover, we investigate the compensational stacking over the precession timescale, which provides consistent results with hypothesis derived from our model data.

1.2.3 Channel deposits and hydrodynamics

Miall (2014) posed a question in his book "Fluvial Depositional Systems" for the petroleum geologists: why do we worry about fluvial deposits and styles? His answer is: we worry because reservoir architecture is the key to reservoir performance. Fluvial architecture is well known for its orders of hierarchy and heterogeneity which significantly impact resource exploration and exploitation. In this study, it is very "rewarding" to characterize and classify the fluvial deposits through investigating variability in three-dimensional sandstone body connectivity specifically because of the framework that was established using paleosol layers (Chapter 3). In this context, we obtain a glimpse of how rivers behave stochastically and sometimes predictably over a certain timescale in a precession-driven cycle (Chapter 4). We characterize facies and facies associations throughout a ca. 300 m stratigraphy in a 10 km² georeferenced photogrammetric model, which is based on a detailed field survey of 108 sandstone bodies in the field. Four channel facies associations are classified, corresponding to four planform river styles: crevasse channel, massive trunk-shaped channel, braided channel, and sinuous channel. These different channel styles are associated with different geometries, hydrodynamics, and potential reservoir properties (e.g. porosity, permeability, connectivity, etc). The frequent alternation between different river styles is attributed to possible climate regimes that result in varying water discharge and sediment calibre in the axial and transverse fluvial systems. Based on a comprehensive literature review, we reconstruct the paleogeography of the Bighorn Basin during the Eocene, which supports our field observations.

1.2.4 Channel-floodplain configuration

After characterizing the fluvial framework defined by palaeosols as cycle boundaries (Chapter 3) and populating the framework with sandstone bodies (Chapter 4), now it is time to investigate how channelized sandstone bodies relate to floodplain aggradation cycle boundaries in the stratigraphic context (Chapter 5). Braided channel deposits are initiated in the avulsion phase, in most cases cutting the lower cycle boundary. Sinuous channel deposits are initiated at the end of the avulsion phase and continue developing in the whole overbank phase by first eroding and then sedimentation. Trunk channel deposits might be ascribed to deeper erosion that concentrates flows in the channels. Importantly, Chapter 5 investigates the fluvial styles from the perspective of cyclically varying external controls, which is different from the traditional scheme that highlights geomorphic zonation. We illustrate the important role of eccentricity that modulates precession cycles in determining the climatic transition, and we offer predictive values of sandstone body distribution and occurrence in the orbitally forced stratigraphic framework.

2

Numerical modelling of alluvial response to orbital forcing

Formation of alluvial stratigraphy is controlled by autogenic processes that mix their imprints with allogenic forcing. In some alluvial successions, sedimentary cycles have been linked to astronomically-driven, cyclic climate changes. However, it remains challenging to define how such cyclic allogenic forcing leads to sedimentary cycles when it continuously occurs in concert with autogenic forcing. Accordingly, we evaluate the impact of cyclic and non-cyclic upstream forcing on alluvial stratigraphy through a process-based alluvial architecture model, the Karssenberg and Bridge (2008) model (KB08). The KB08 model depicts diffusion-based sediment transport, erosion and deposition within a network of channel belts and associated floodplains, with river avulsion dependent on lateral floodplain gradient, flood magnitude and frequency, and stochastic components. We find cyclic alluvial stratigraphic patterns to occur when there is cyclicity in the ratio of sediment supply over water discharge (Q_s/Q_w ratio), in the precondition that the allogenic forcing has sufficiently large amplitudes and long, but not very long, wavelengths, depending on inherent properties of the modelled basin (e.g. basin subsidence, size, and slope). Each alluvial stratigraphic cycle consists of two phases: an aggradation phase characterized by rapid sedimentation due to frequent channel shifting and a non-deposition phase characterized by channel belt stability and, depending on Q_s/Q_w amplitudes, incision. Larger Q_s/Q_w ratio amplitudes contribute to weaker downstream signal shredding by stochastic components in the model. Floodplain topographic differences are found to be compensated by autogenic dynamics at certain compensational timescales in fully autogenic runs, while the presence of allogenic forcing clearly impacts the compensational stacking patterns.

2.1 Introduction

Alluvial deposition is controlled by both autogenic and allogenic controls (Abels et al., 2013; Hajek et al., 2012), which are difficult to be disentangled since they act at overlapping spatial and temporal scales (Bridge, 1993; Stouthamer and Berendsen, 2007). Moreover, it remains to be answered whether autogenic variability can produce cyclicity that resembles allogenic stratigraphic products (Feng et al., 2019; Hajek and Straub, 2017). Allogenic controls on a fluvial depositional environment refer to changes in upstream and downstream conditions, such as climatically-driven water discharge and sediment supply variation, tectonically-driven basin subsidence and exhumation, and climatically- and/or tectonically-driven base-level fluctuation. Some of these controls may have cyclic origins when they are related to Earth's orbital cycles that play important roles in past climate changes. Astronomically-driven climate cycles may therefore cause cyclicity in alluvial depositional records (Abels et al., 2013). Autogenic controls refer to internally generated dynamics that can produce complex, relatively large-scale stratigraphic patterns even while allogenic forcing remains constant (Hajek and Straub, 2017). Practical examples are channel migration, channel bifurcation and avulsion, crevasse splay formation, levee breaching, consolidation of previously deposited sediments, and interaction with local flora and fauna.

Regularly distributed paleosols alternating with avulsion belt deposits in the Bighorn Basin, Wyoming, USA, have been ascribed to astronomical climate forcing (Abdul Aziz et al., 2008; Abels et al., 2013, 2016; van der Meulen et al., 2020). Abels et al. (2013) produced a qualitative depositional model for the observed cyclic floodplain successions within the frame of astronomical climate forcing. In this model, each cycle consists of an avulsion phase featured by thick, laterally-extensive heterolithic intervals and an overbank phase characterized by a few stable channels and fine sediments in which strong palaeosols have developed. These intervals of floodplain stability during the overbank phase alternating with episodes of large–scale fluvial system reorganization during the avulsion phase could be entirely autogenic; however, the remarkable regularity and the close match in time scales with precession forcing indicate these sedimentary cycles to be likely paced by allogenic, astronomically–forced climate changes (Abels et al., 2013, 2016; van der Meulen et al., 2020). In this case and other similar cases, uncertainties remain, such as how an alluvial system reacts to cyclic upstream climate changes, and in which conditions these climate changes have higher chances of being preserved as sedimentary cycles. In this context, a process-based numerical alluvial architecture model may help to elucidate the response of an alluvial system to cyclic upstream climate changes through vividly illustrating the interaction between allogenic and autogenic forcing.

Process-based numerical models are suitable for exploring, explaining, and predicting river behaviour in response to changing environmental parameters. They are employed to compare the arguably distant relationship between numerical modelling and field observation, namely sedimentary processes and sedimentary products (Hajek and Wolinsky, 2012). There are several basin-scale models for fluvial stratigraphy simulation (Jerolmack and Paola, 2007; Karssenberg and Bridge, 2008; Mackey and Bridge, 1995), amongst others. Some models that highlight short-scale fluvial dynamics incorporate complex physical processes, such as Delft3D. However, these are not yet able to simulate a basin-scale alluvial system at the long time scale we wish to analyse. In this context, we choose the Karssen-

berg and Bridge (2008) (hereafter referred to as KB08) model as an appropriate tool to solve our research questions. The KB08 model is primarily diffusion-based, in which the rate of diffusion is a function of discharge of individual channels and thus varies in space and time. This, together with stochastic components relating to channel bifurcation and avulsion, produces dynamic and unpredictable model behaviour that could be to a large extent comparable to autogenic processes in reality (Karssenberg and Bridge, 2008).

The objectives of this study are four–fold: (1) to elucidate impacts of cyclic and non-cyclic upstream climate forcing, including their amplitude and wavelength, on the modelled alluvial deposition, (2) to investigate conditions that can lead to cyclic stratigraphic records, (3) to gain insights into compensational time scales and mechanisms related to interaction between allogenic and autogenic controls, and (4) to illustrate allogenic signal propagation downstream in the alluvial basin.

2.2 Methods

2.2.1 Process representation in the KB08 model

The process-based numerical model presented by Karssenberg and Bridge (2008) is applicable to target basin-scale stratigraphy. It considers sediment transport, erosion and deposition within a network of channel belts, floodplain, and topographic slope based on the earlier work by Mackey and Bridge (1995). Boundary conditions at the upstream inlet are mean annual water discharge (Q_w) and sediment load (Q_s) that includes both bedload and suspended load. Boundary condition in the downstream is the base level change over the width of the modeled basin. Basin subsidence is absent in the model, but is mimicked by base-level rise.

In the model, sediment and water are transported through a network of channel belts according to the diffusion equation, the rate of which is a function of discharge of individual channels and thus varies in space and time. The width of a channel belt increases over time, while the depth of it depends on water discharge. Channel-belt aggradation and degradation are calculated using the sediment continuity equation. Floodplain aggradation is a function of channel-belt aggradation rate and distance from channel belts, and it occurs only when the topographical elevation of a floodplain cell is less than that of the nearest channel-belt cell. while floodplain degradation is treated using a sediment diffusion-advection approach. Sediment conservation occurs in the channel belt system, but not in the floodplain, where sufficient sediment is assumed to be available.

There are two ways for channel belt bifurcation to occur in the model. The first is stochastic bifurcation, both location and frequency of which are determined randomly. The second is dependent bifurcation, which is a function of cross-valley slope (S_{cv}) advantage over the down-valley slope (S_{dv}) as well as return period of flood discharge exceeding a certain threshold value (Q_a). The probability of an dependent bifurcation, $P(B)$, is calculated at each grid at each time step according to Equation (2.1):

$$P(B) = (\frac{Q_w}{Q_a})^{e_Q} (k_S \frac{S_{cv}}{S_{dv}})^{e_S} \tag{2.1}$$

where k_S is is the slope proportionality constant, e_Q is threshold discharge component, and e_s is slope exponent (Karssenberg and Bridge, 2008; Mackey and Bridge, 1995).

Whether a bifurcation is initiated or not depends on Equation (2.2):

$$\textbf{if } P(B)_{x,y,t} > U(0,1) :$$
$$\text{A bifurcation is initiated;}$$
$$\textbf{else:}$$
$$\text{No bifurcation is initiated.} \tag{2.2}$$

where $P(B)_{x,y,t}$ is the bifurcation probability at a location with the coordinate of (x,y) at time t, and $U(0,1)$ is a random number chosen from a uniform distribution of 0 to 1.

At bifurcations, water is distributed over two channels according to Equation (2.3):

$$\frac{q_1}{q_2} = \sqrt{\frac{s_1\, n_1(1,\sigma^2)}{s_2\, n_2(1,\sigma^2)}} \tag{2.3}$$

where q_1 and s_1 are, respectively, the water discharge (m3/year) and the gradient of the first bifurcating channel, q_2 and s_2 are the same variables for the second bifurcating channel. The sum of q_1 and q_2 is constant and termed as q_0. $n_1(1,\sigma^2)$ and $n_2(1,\sigma^2)$ generate random variables that have normal distributions with mean zero and variance σ^2. These noise terms are included to represent local random effects on channel gradients at the bifurcation point. If q_1/q_0 or q_2/q_0 falls below a critical value u_{crit} (herein 0.4, Table 2.1), a bifurcation turns into an avulsion.

Presence of the random number in Equation (2.2) and noise terms in Equation (2.3) result in the fact that outputs of KB08 model are not deterministic. Given this, we run 10 realizations for each scenario to statistically confirm our findings, accompanied by full post-processing for all of them.

2.2.2 Model set up and scenarios

Formation of alluvial stratigraphy is controlled by autogenic processes that mix their imprints with allogenic forcing. In some alluvial successions, sedimentary cycles have been linked to astronomically-driven, cyclic climate changes.

The modelled rectangular basin has a down-valley length of 60 km and a cross-valley width of 40 km, and it is discretized by square raster cells with a constant cell length of 200 m (Figure 2.1). The initial basin slope is set to be 0.00011 (0.11 m/km), and it matches a constant water discharge (Q_{w0}) of 7.9 × 10¹⁰ m³/year and a constant sediment supply (Q_{s0}) of 1.0 × 10¹⁰ m³/year to produce graded fluvial profiles (Karssenberg and Bridge, 2008). The total simulation is 40 kyr with a time step of 1 year. Other parameters not specified here are listed in Table 2.1.

(1) The equilibrium scenario

The equilibrium scenario is to generate graded fluvial profiles that result from matching water discharge, sediment supply and basin slope. The base level is set at 0 m at the downstream boundary of the basin throughout the 40-kyr simulation.

(2) The autogenic scenario

Based on the equilibrium scenario, we create long-term accommodation through steadily rising the base level at a rate of 0.4 m/kyr, which matches the long-term depositional rate

that can be approximated by dividing Q_{s0} (1.0 × 10⁶ m³/year) over the basin size (60 km by 40 km). In this scenario, stratigraphy is built up under full autogenic controls, since there are no variations in the water discharge and sediment supply at the basin inlet. This scenario will be referred to as Scenario NC (abbreviated for non-cyclic) in the following part.

(3) The allogenic scenarios
The relation between water discharge and sediment flux has been widely studied and discussed. In general, water discharge presents a quasi-instantaneous response to precipitation and evaporation changes, despite that multiple catchment parameters have their impacts, such as ground water levels and vegetation cover. The response of sediment flux to water discharge is more complex, and that could be highly non-linear and different at various time scales (Allen, 2008; Forzoni et al., 2014; Métivier and Gaudemer, 1999; Whipple and Tucker, 2002). Larger catchments tend to strengthen the inertia and the non-linear response of sediment transport systems to external forcing (Allen, 2008; Métivier and Gaudemer, 1999).
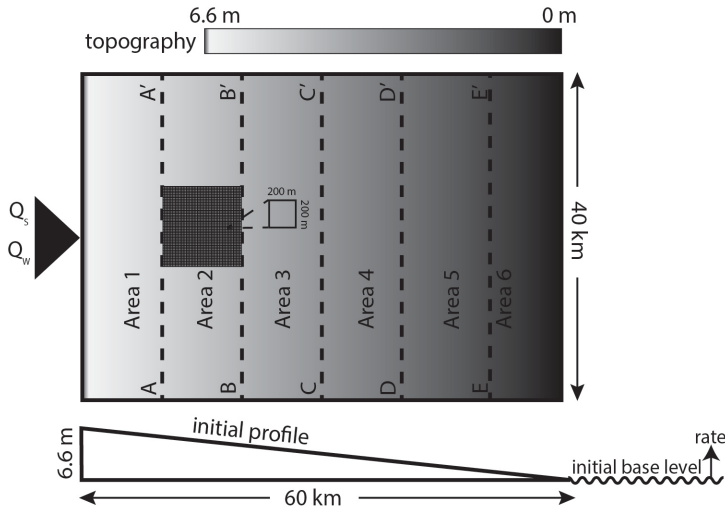
Figure 2.1: Initial alluvial plain in map view (top) and longitudinal view along basin axis (below). Raster size is 200 m by 200 m. Five dash lines (e.g. AA') divide the basin into six areas, respectively denoted as Areas 1-6.

Our objective is to evaluate the effect of cyclic and non-cyclic upstream forcing on alluvial stratigraphy, and we follow a simple relation between sediment load and water discharge based on Syvitski et al. (2000):

$$Q_{st} = aQ_{wt}^{b+1} \tag{2.4}$$

where $Q_{st}(m^3/s)$ is the sediment load at time step t, a is a constant related to long-term water discharge, basin relief and temperature, $Q_{wt}(m^3/s)$ is the water discharge at time step t, and b is a constant related to long term suspended load, basin relief and temperature (Syvitski et al., 2000). Constants a and b are adjusted to 9 × 10⁻⁹ and 0.925, respectively,

Table 2.1: Parameters used in this study

Parameter	Value	Explanation
a	0.0127	Parameter in slope-dependent sediment transport equation
A	0.2	Parameter in hill slope degradation equation
b	2000	Floodplain aggradation exponent (m)
β	1.5	Parameter in hill slope degradation equation
BF	200.0	Floodplain aggradation exponent (m)
c_1	200	Cell length (m)
c	0.0003	The bank erodibility (year^{-1})
C	0.2	Sedimentation rate at infinite distance from the channel belt
e	0.02	Upper bound of uniform distribution for noise term (m)
γ	14	Parameter in hill slope degradation equation
j	32×10^6	Conversion constant (m³/year to m³/s)
k	0.055	Slope ratio proportionality constant
l	6×10^4	Down-valley length of modelling area (m)
μ	5	Slope ratio exponent
n	0.04	Manning's n ($s/m^{\frac{1}{3}}$)
P	0.5	Net precipitation (m/year)
Q_{s0}	1×10^6	Sediment supply (m³/year) at the inflow point
Q_{w0}	7.9×10^{10}	Water discharge (m³/year) at inflow point
s_f	0.00011	Initial slope of floodplain
σ^2	0.0036	Variance of noise term in slope calculation of bifurcating streams
t_{end}	40000	Time at end of model run (year)
t_{st}	0	Time at start of model run (year)
Δt	1	Duration of one time step (year)
$u(0,e)$		Uniform noise term (m) for initial floodplain topography
U_{crit}	0.4	Critical discharge ratio
W	2×10^4	Cross-valley width of modelling area (m)
z	1.0	Channel side slope

based on sensitivity tests in our model to have sediment and water volumes in balance with basin size, basin slope and base level rise rate. We first design two scenarios, where Q_w is in the simple sinusoidal form and varies in amplitude (A = 0.1 or 0.2, Equation (2.5)), and Q_s is dependent on Q_w following Equation (2.4).

$$Q_{wt} = ASin(\frac{2\pi}{T}t + \pi) + Q_{w0} \tag{2.5}$$

where A is 0.1 or 0.2, T is 10 kyr, and Q_{w0} (m³/s) is water discharge at t = 0, which is 7.9×10^{10} m³/year, as mentioned above. These two scenarios with Q_s/Q_w ratio amplitudes of 0.1 and 0.2 will be hereinafter referred to as Scenarios C10 and C20, respectively.

The Q_s/Q_w ratio is cyclic when Q_w is cyclic, as can be clearly seen if we divide Q_{wt} on both sides of Equation 4, yielding:

$$Q_{st}/Q_{wt} = aQ_{wt}^b \tag{2.6}$$

Table 2.2: Model parameters varied in scenarios with different themes. A_w and T denote amplitude and wavelength of Q_w variation, A_s and A_c represent amplitudes of Q_s and Q_s/Q_w variations, and c stands for base level rise rate. Wavelengths of Q_s and Q_s/Q_w, if they are cyclic, are identical to that of Q_w.

Theme	Scenarios	A_w (%)	T (kyr)	A_s (%)	A_c (%)	c (m/kyr)
Equilibrium	E	0	0	0	0	0
Non-cyclic	NC	0	10	0	0	0.4
Q_w-dependent Q_s	C10	10	10	20	9	0.4
	C20	20	10	40	18	0.4
Q_w-independent Q_s	A5	5	10	0	5	0.4
	A10	10	10	0	11	0.4
	A20	20	10	0	22	0.4
	A40	40	10	0	53	0.4
	W1.25	20	1.25	0	22	0.4
	W2.5	20	2.5	0	22	0.4
	W5	20	5	0	22	0.4
	W10	20	10	0	22	0.4
	W20	20	20	0	22	0.4
Constant Q_w, varied Q_s	CW	0	10	20	20	0.4

As Q_s responds exponentially to Q_w changes in the relation proposed by Syvitski et al. (2000), the Q_s variability will be extremely large when the amplitude of Q_w is large. However, the KB08 model is not able to deal with such extremely large Q_s variability. Since one of our goals is to test the impact of cyclic Q_s/Q_w forcing amplitude on the alluvial stratigraphy, we choose to keep Q_s stable while varying Q_w to result in cyclic Q_s/Q_w ratios, which shares high consistency with the model choices by Zhang et al. (2018). Specifically, we design a set of amplitude-themed scenarios, with constant Q_w wavelengths of 10 kyr and variable Q_w amplitudes from 0.05 to 0.4 (referred to as Scenarios A5, A10, A20, and A40, respectively, Table 2.2). Similarly, we design wavelength-themed scenarios with constant Q_w amplitudes of 20% and varied Q_w wavelengths from 1.25 kyr to 20 kyr (referred to as Scenarios W1.25, W2.5, W5, W10, and W20, respectively, Table 2.2). Meanwhile, we also design a scenario with constant Q_w and variable Q_s (referred to as Scenario CW, Table 2.2), which is to validate the role of Q_s/Q_w ratio.

2.2.3 Post-processing

All numerical simulations are run on a Linux computer with an Intel i7 eight-core processor at 2.93 GHz using a RAM of 16 GB, and the operation system is Ubuntu 18.04.2 LTS. For each scenario, it takes 10-15 hours to run one 40 kyr-long realization with a basin size of 40 km by 60 km. A series of topographic maps at different time steps are generated, and they are post-processed using Anaconda Spyder (Python 3.6), including calculation of regionally-averaged depositional rates, time series analysis of regionally-averaged depositional rates, and identification of compensational time scales. These calculations are all implemented in the upstream realm at the cross-section topography along line BB' with its location shown in Figure 2.1, if not otherwise specified. This decision is based on consideration of the fact that line BB' has a certain distance from the basin inlet, which prevents

from overwhelming upstream influence, while it is also relatively far from the basin outlet, minimizing the effect of the base level variation. For all realizations, base-level locations are monitored to ensure they remain in the downstream portions of the modelled basin.

2

Calculation of regionally-averaged depositional rates

We calculate the 1D deposition rate ($D_{x,y,t}$) at a certain location using Equation (2.7):

$$D_{x,y,t} = \frac{h_{x,y,t+\Delta t} - h_{x,y,t}}{\Delta t} \tag{2.7}$$

where $h_{x,y,t}$ is surface elevation at the location with coordinates (x,y) at time t, Δt is the sampling interval, and $D_{x,y,t}$ is the depositional rate at the location with coordinate (x,y) during the time interval from t to t + Δt.

The average depositional rate over the floodplain width $\overline{D_{x,y,t}}$ is calculated in order to analyse regional-scale depositional patterns. This is done on cross-section topography along the line BB' (location shown in Figure 2.1), unless otherwise specified.

Time series analysis

The REDFIT protocol in the software PAST 3 version 3.14 (Hammer et al., 2001) for time series analysis is deployed on the $\overline{D_{x,y,t}}$ calculated in Section 2.3.1. The method is run with n = 1,000 Monte Carlo simulations of the autoregressive (AR1) process, oversampling and segmentation intervals of 1, and a Blackman-Harris window. All 90%, 95%, and 99% level χ^2 and the theoretical AR1 are displayed. To focus on long-wavelength signals (>1,000 years), the upper cut-off frequency is set to be 1 kyr^{-1} in all analyses. Given the good time control in these numerical exercises, we only regard peaks with their confidence levels higher than 99% as reliable signals present in the stratigraphic record (Kemp, 2016; Vaughan et al., 2011).

Compensational time scale identification

We use the standard deviation of sedimentation/subsidence (σ_{ss}) (Wang et al., 2011) to characterize the compensational timescale (Equation (2.8)), which is a dimension-reduced term of that by Straub et al. (2009):

$$\sigma_{ss}(T) = \{\int_a^b [\frac{r(T;x)}{\hat{r}(x)} - 1]^2 dL\}^{1/2} \tag{2.8}$$

where $r(T;x)$ is the average deposition rate at a horizontal coordinate of x along line BB' during a time interval of T, which ranges from 100 to 40,000 years in this study, L is the cross-basin length, which is 20 km in this study and $\hat{r}(x)$ is the local long-term sedimentation (or subsidence) rate, herein 0.4 m/kyr. σ_{ss} is expected to decrease as T increases, following a power-law trend:

$$\sigma_{ss} = a' T^{-\kappa} \tag{2.9}$$

where a' is a coefficient, and the exponent, κ, is termed the compensation index. At a certain time scale when κ exceeds 0.5, the stratigraphic stacking transits from random/anti-compensational form to compensational form, and when it reaches 1.0, the stacking is

purely compensational (Straub et al., 2009). In other words, a transport system is able to visit every spot in a basin repeatedly during an interval longer than this time scale.

2.3 Results

2.3.1 Alluvial stratigraphy in the equilibrium scenario

Over the 40 kyr simulations, the surface topography of Scenario Equilibrium reveals very small changes. Specifically, the cross-section topography varies in a very small range (Figure 2.2A and 2.2B), and the longitudinal topography indicates long-term graded fluvial profiles (Figure 2.2C). Correspondingly, slow deposition sporadically occurs at certain locations and certain time moments, accompanied by very small-scale erosion at certain locations and certain time moments (Figure 2.2D and 2.2E). The REDFIT power spectrum shows no peaks with their confidence levels higher than 99% (Figure 2.2F).
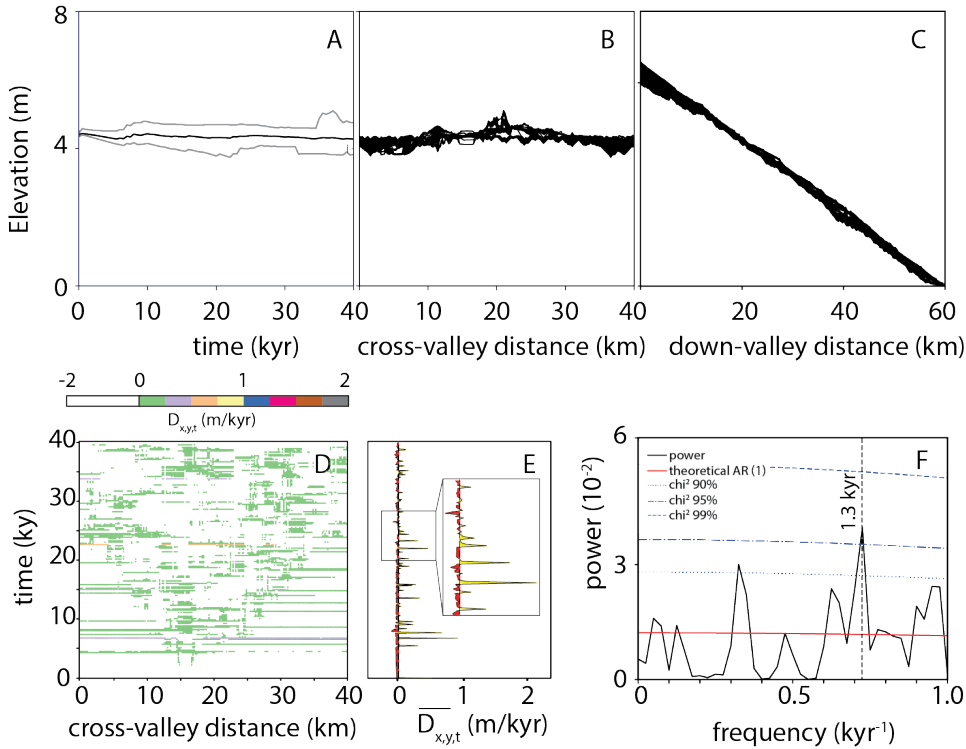
Figure 2.2: Alluvial stratigraphic patterns of Scenario Equilibrium. (A) Temporal range of surface topography (bounded by two grey lines) and average topography (solid line) for cross-section along line BB' (position shown in Figure 2.1); (B) Cross-section surface topography along line BB' of multiple moments with a time interval of 500 years; (C) Longitudinal surface topography along the basin axis of multiple moments with a time interval of 500 years; (D) Chronostratigraphic diagram showing spatial and temporal variability in depositional rates $\overline{D_{x,y,t}}$ for cross-section along line BB', white areas indicate degradation and colored dots indicate aggradation (m/kyr); (E) Time series of average depositional/erosional rate $\overline{D_{x,y,t}}$, with positive deposition rate marked with yellow color and negative red; (F) REDFIT power spectrum of $\overline{D_{x,y,t}}$.

2

2.3.2 Alluvial stratigraphy in the autogenic scenario

Scenario NC presents long-term topographic build-up (panels A1 and B1, Figure 2.3), because of long-term accommodation created by base level rise. Depositional and erosional patterns occur randomly in time and space, with deposition taking the dominance both temporally and spatially (panels C1 and D1, Figure 2.3). There are no peaks with their confidence levels higher than 99% (panel E1, Figure 2.3). Since there is no allogenic forcing in this scenario, this peak is speculated to result from autogenic processes, although it might be fully spurious. We apply the method of Straub et al. (2009) in analyzing the cross-section topography (panel B1, Figure 2.3), and identify a transition from anti-compensational to compensational stacking at a time scale of 2.0 kyr (Figure 2.4A). Above this compensational timescale, σ_{ss} decays in the temporal domain following a power law with a nearly identical value of κ.

2.3.3 Alluvial stratigraphy in the allogenic scenario

Impact of cyclic Q_s/Q_w ratio

Scenarios C10 and C20 present regularly alternating episodes of depositional and erosional non-depositional patterns (e.g. panels A2-D2 and A3-D3, Figure 2.3), which are not shown in Scenario NC. Specifically, we refer to the episode with low/negative average depositional rates as the non-deposition phase, as manifested by the near-horizontal average elevation profile (e.g. panel A3, Figure 2.3), clustered timelines in the cross-section topography (e.g. panel B3, Figure 2.3), and zero/negative average depositional rates (e.g. panels C3 and D3, Figure 2.3). In comparison, we refer to the other episode with positive depositional rates as the aggradation phase, which is embodied by the rapidly increasing average elevation profile (e.g. panel A3, Figure 2.3), separated timelines in the cross-section topography (e.g. panel B3, Figure 2.3), and positive and in many cases very high depositional rates (e.g. panels C3 and D3, Figure 2.3). We observe peaks at periodicities of exact 10 kyr in the power spectra (panels E2 and E3, Figure 2.3), which coincide with the allogenic forcing wavelength. We find σ_{ss} in Scenarios C10 and C20 behaves very differently when compared to Scenario NC. The compensational time scales in Scenarios C10 and C20 are similarly prolonged to 5.1 kyr (Figure 2.3B and 2.3C), if we only look at the data interval with the time window smaller than 10 kyr. Fluctuation of σ_{ss} in the > 10 kyr time window presents slightly cyclic features in Scenario C10 (Figure 2.3B) and strongly cyclic features in Scenario C20 (Figure 2.3B and 2.3C), which could be ascribed to the fact that we are estimating compensational time scales across the aggradation/non-deposition phases that comprise allogenic cycles (S. Trampush, personal communication, June 14, 2019).

For Scenario C20, the alluvial system is in a non-deposition phase (Points a to c in Figure 2.5A) when the Q_s/Q_w ratio decreases or is low. A few active channel belts are present in the model during this phase, and they constantly widen and gradually build up the topography (Figure 2.5B and 2.5C). The aggradation phase occurs when the Q_s/Q_w ratio increases or is high (Points d to f in Figure 2.5A). This phase is initiated with a first avulsion that results from super-elevation of the channel belt over the floodplain (panel d in Figure 2.5C). After that, frequent channel avulsion causes rapid aggradation over the entire width of the modelled basin (Figure 2.5C). In the aggradation phases, channel belts are narrow due to their short life times, and water discharge in individual channel belts is also relatively low (Figure 2.5B).

The KB08 model is stochastic, meaning different outcomes for different realizations of the same scenario. However, based on 10 realizations of Scenario C20, consistency is seen when it comes to regular alternation of aggradation and non-deposition phases (Figure 2.6). Their initiation timing lags the (Q_s/Q_w)min by 0.6-1.2 kyr in a 10-kyr cycle, while their termination timing lags the (Q_s/Q_w)max by 0.3-1.6 kyr in a 10-kyr cycle (Figure 2.6A). Correspondingly, the relative duration of an aggradation phase is 40%-61% of an allogenic cycle wavelength (Figure 2.6B).

The downstream propagation of the cyclic upstream forcing is analyzed via the average depositional rate across the modelled basin in Scenario C20. As the distance from the basin inlet increases, alternation of aggradation and non-deposition phases become less distinct, as reflected by the shortened duration of non-deposition phases (red-colored part in panels A1-E1, Figure 2.7) and lowered spectra power and confidence levels of the dominant peaks (panels A2-E2, Figure 2.7). No >99% confidence level peaks are observed at cross-section along line DD' (panel D2, Figure 2.7), though the most dominant peak is still at a periodicity of 10 kyr. In comparison, no peaks are present at the allogenic wavelength at cross-section along line EE' (panel E2, Figure 2.7), which indicates full shredding of the upstream Q_s/Q_w signal. The location where the base level reaches the alluvial plain is shown in Figure 2.8.
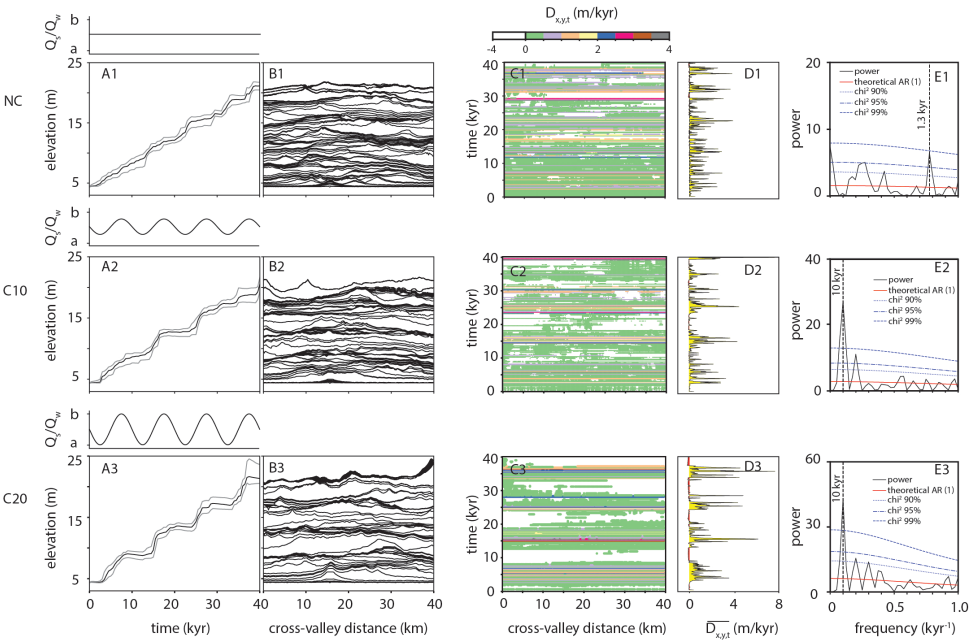

Figure 2.3: Alluvial stratigraphic patterns of non-cyclic (Scenario NC) and cyclic scenarios (Scenarios C10 and C20). Curves of Qs/Qw ratios are displayed above panel A of each scenario, and a in the y axis equals 1.0×10-5 and b equals 1.5 ×10-5. For other legends, see details in Figure 2.2.

Impact of Q_s/Q_w ratio amplitude

Scenario A5 presents similar depositional patterns to Scenario NC that has zero Q_s/Q_w ratio amplitude (panels A1-D1, Figure 2.9), and there are no peaks with >95% confidence levels at the forcing wavelength in the power spectrum (panel E1, Figure 2.9). In comparison, cyclic patterns start to emerge in Scenario A10, reflected in the elevation profile, cross-section topography, chronostratigraphic diagram, and average depositional/erosional rate (panels A2-D2, Figure 2.9), accompanied by a >99% confidence level peak at 10 kyr that coincides with the allogenic forcing wavelength (panel E2, Figure 2.9). Scenarios A20 and A40 present clearer alternations of aggradation and non-deposition phases (panels A3-D3 and A4-D4, Figure 2.9), accompanied by peaks at 10 kyr with higher power and confidence levels (panels E3 and E4, Figure 2.9). Time lines for the non-deposition phase in cross-section topography of Scenario A40 are extremely clustered, indicating very low sedimentation over a long time period, associated with greatly confined channel belts (e.g. red eclipse marked in panel B4, Figure 2.9) that are later filled (e.g. red eclipse marked in panel C4, Figure 2.9). Note that the aggradation phase is defined as the moment in time when channel belt avulsion and rapid aggradation occurs on the alluvial plain. Aggradation within the confined channel belts, until the moment when super-elevation is reached and avulsion is triggered, is also defined as part of the non-deposition phase. Scenario CW presents highly similar features to Scenarios C20 and A20, and they share very similar Q_s/Q_w ratio amplitudes and exactly the same Q_s/Q_w ratio wavelengths.

Impact of Q_s/Q_w ratio wavelength

With a Q_s/Q_w ratio amplitude of 20%, even a very small Q_s/Q_w ratio wavelength can lead to clear cyclicity in the temporal domain, as reflected in the chronostratigraphic diagram (e.g. panels C1 and C2, Figure 2.10), the deposition rate time series (e.g. panels D1 and D2, Figure 2.10), and the >99% confidence level peaks at the forcing wavelength in the power spectra (e.g. panels E1 and E2, Figure 2.10). However, many cycles with their wavelengths shorter than 5 kyr are overprinted by subsequent cycles (e.g. panels B1 and B2, Figure 2.10). Interestingly, some seemingly regular large-scale aggradation occurs at a longer wavelength than the forcing wavelength in Scenario W1.25 (panels A1 and D1, Figure 2.10). In other words, there seem to be 4-5 larger-scale cycles in Scenario W1.25, besides 16 smaller-scale cycles with wavelengths of 1.25 kyr.

As the allogenic forcing wavelength increases from 1.25 kyr to 10 kyr, the aggradation and non-deposition phases become more and more clearly separated topographically, reflected in the average elevation profile, cross-section topography and chronostratigraphic diagram (Figure 2.10). However, when the allogenic forcing wavelength is as long as 20 kyr, some regional aggradation occurs in its non-deposition phase (e.g. the peak at around 19 kyr in panel D5, Figure 2.10), which has smaller magnitudes than that in its aggradation phase. This relatively smaller-scale aggradation occurring in the non-deposition phase makes the resultant depositional patterns less obviously cyclic, despite the fact that the spectral power peak at the forcing wavelength crosses the 99% confidence level (panel E5, Figure 2.10).

2
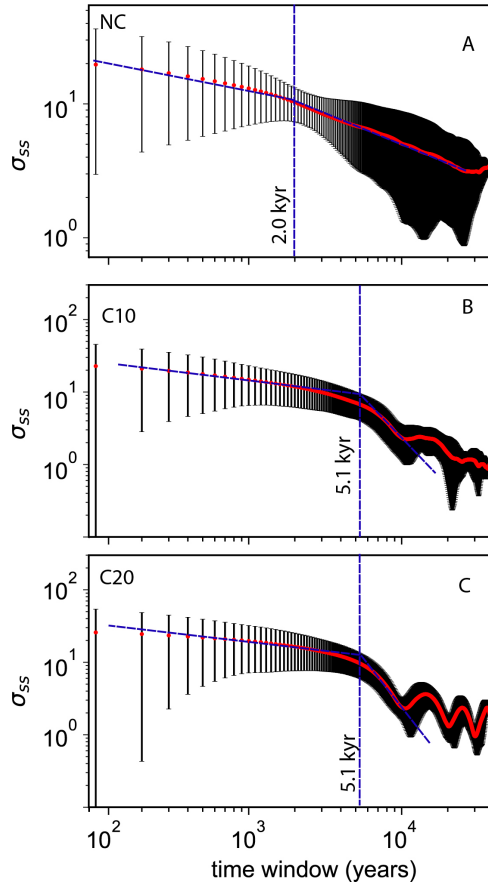
Figure 2.4: Decay of σ_{ss} with increasing time window for Scenarios NC (A), C10 (B), and C20 (C). Error bars represent geometric standard deviation of σss, while red dots indicate the average σss at corresponding time window, blue dashed trend lines represent best-fit linear regression to log-log data, and vertical blue dashed lines, passing through the intersection points of two blue trend lines, indicate the predicted compensational time scales, over which the stratigraphic stacking transits from random/anti-compensational to compensational form.

2
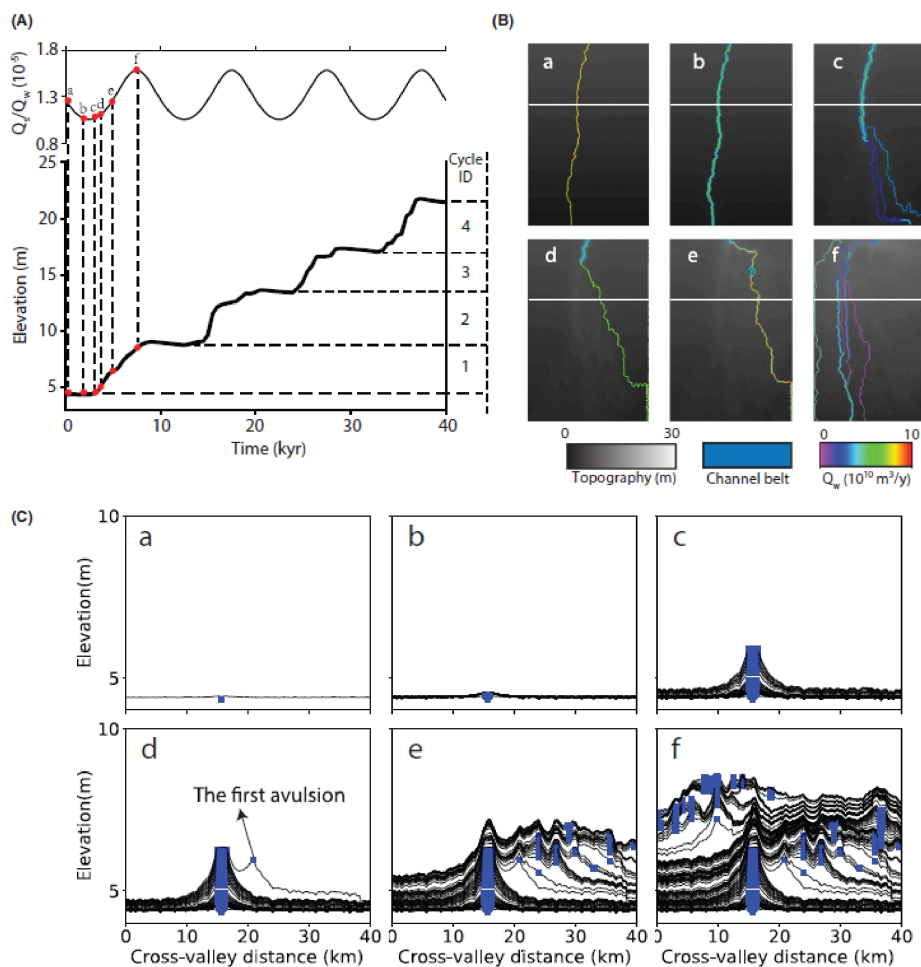
Figure 2.5: Alluvial stratigraphic patterns of one cycle in Scenario A20. (A) Six time points are selected for observation: points a-c in the non-deposition phase, and points d-f in the aggradation phase. (B) Topographical maps corresponding to six observational points in panel A. White lines indicate the position of Line BB' in Figure 2.1. (C) Topography at six observation points, where blue squares represent channel belt locations.
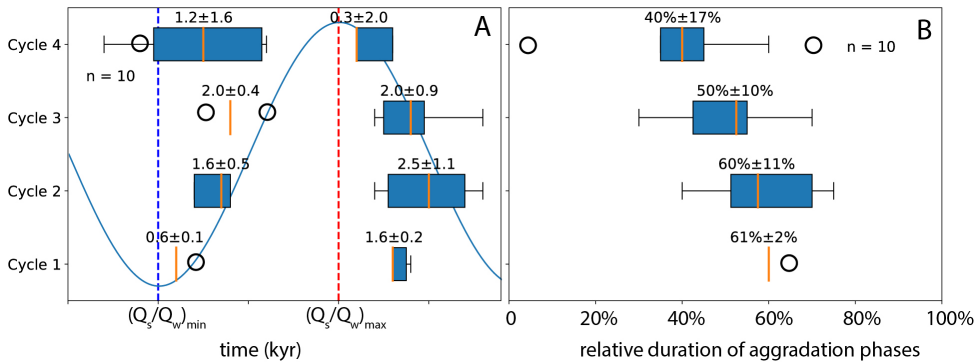
Figure 2.6: Timing and relative duration of aggradation phases in 10 realizations of Scenarios C20. (A) Initiation timing of aggradation phases. Blue and red dashed lines indicate $(Qs/Qw)_{min}$ and $(Qs/Qw)_{max}$, respectively. Box and whiskers plots show the range of data (whiskers), the lower and upper quartiles (box boundaries), and median (orange line within the box). Isolated dots represent extreme outliers, defined as greater than two times the interquartile range below or above the first or third quartiles, respectively. Numbers in formats of a ± b represent "mean ± standard deviation" of the time lag of an aggradation phase initiation or termination with respect to $(Qs/Qw)_{min}$ or $(Qs/Qw)_{max}$. (B) Relative duration of aggradation phases. Numbers in formats of a ± b represent "mean ± standard deviation" of the relative aggradation phase duration in one cycle.
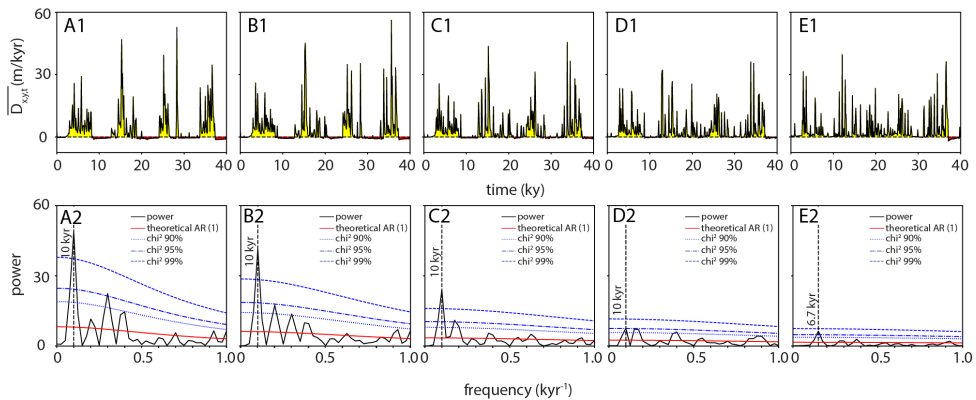
Figure 2.7: Signal weakening in the downstream direction in Scenario C20. From left to right, they are average depositional rates and REDFIT power spectra along lines AA', BB', CC', DD' and EE', respectively (positions shown in Figure 2.1).

2
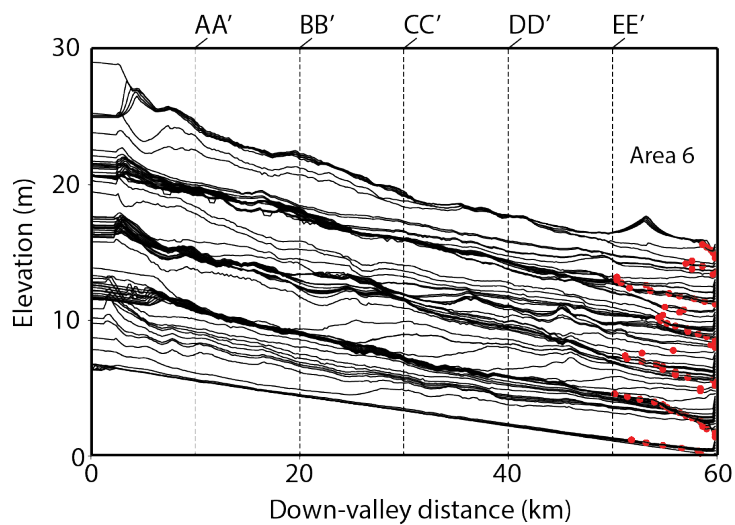
Figure 2.8: Fluvial profiles along the basin axis for Scenario C20. Red dots indicate where the base level reaches the land surface. Time interval between two successive profiles is 500 years.
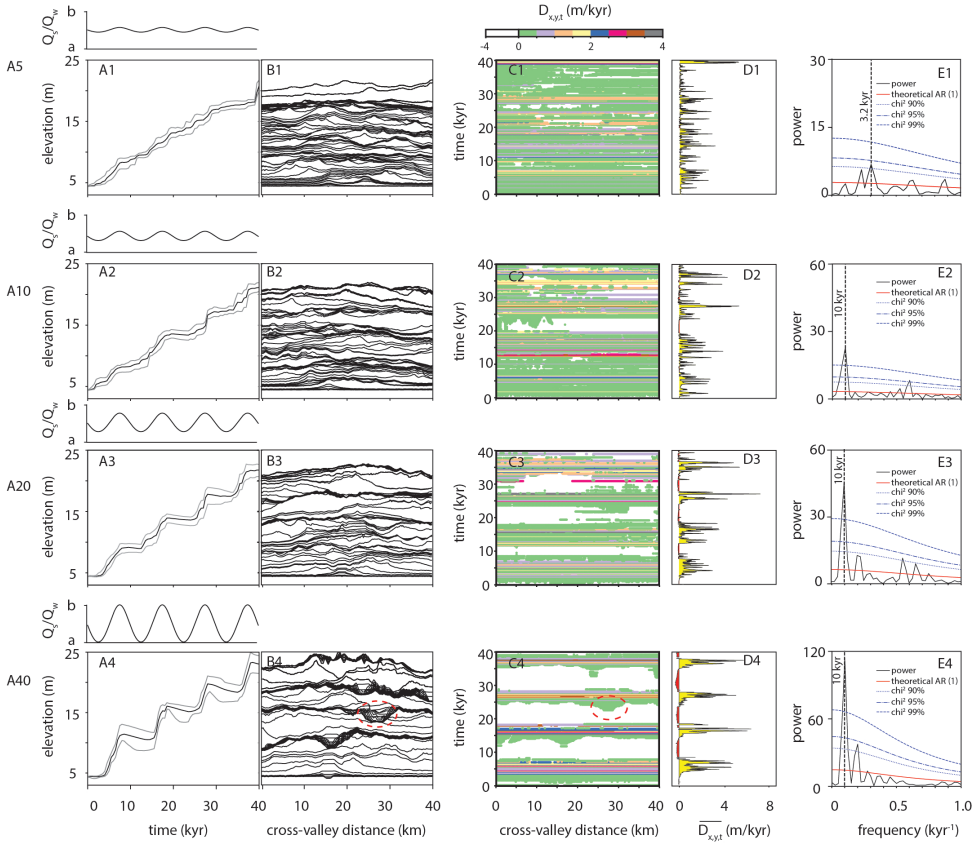
Figure 2.9: Alluvial stratigraphic patterns of scenarios with different Q_s/Q_w amplitudes (Scenarios A5, A10, A20, and A40). Curves of Q_s/Q_w ratios are displayed above panel A of each scenario, and a in the y axis equals 0.8×10^{-5} and b equals 1.8×10^{-5}. Red ellipse in panel B4 shows an example of largely confined channel belts, while red ellipse in panel C4 shows an example of rapid aggradation in the channel belt before superelevation is reached and avulsion occurs.

2
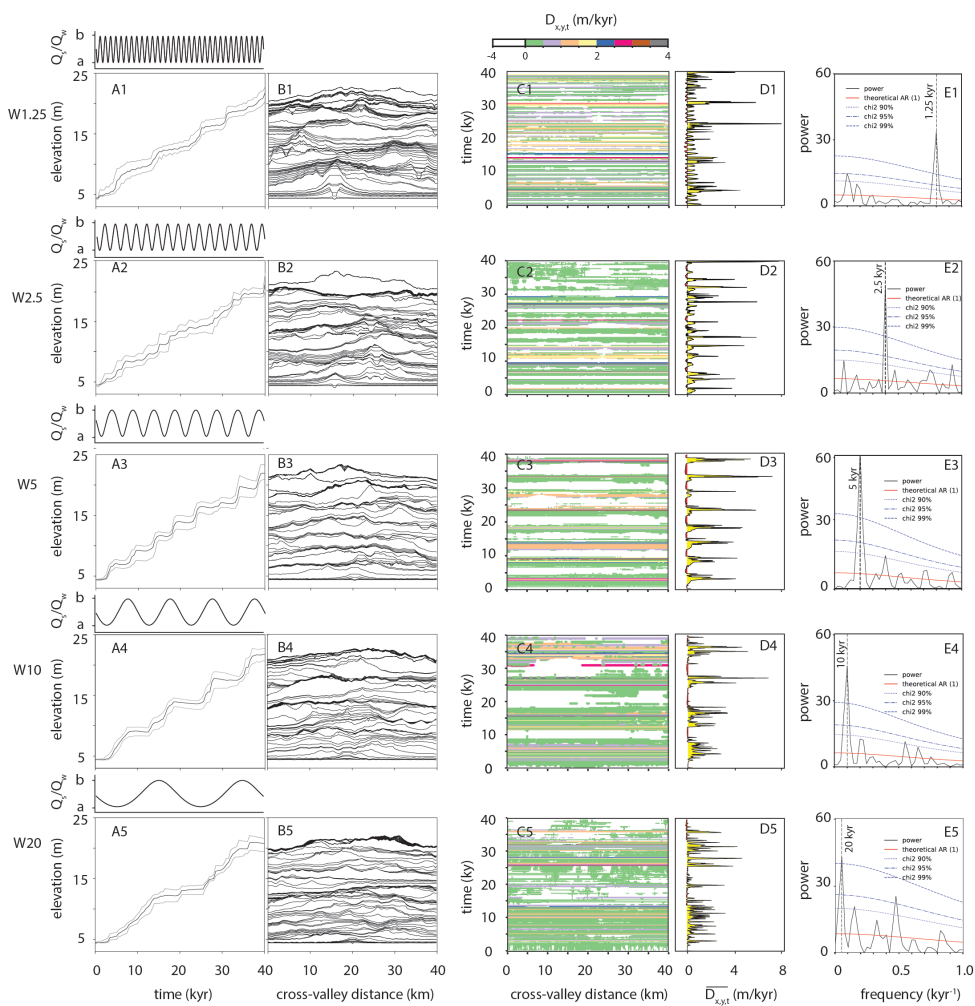
Figure 2.10: Alluvial stratigraphic patterns of scenarios with different Q_s/Q_w wavelengths (Scenarios W1.25, W2.5, W5, W10, and W20). Curves of Q_s/Q_w ratios are displayed above panel A of each scenario, and a in the y axis equals 1.0×10^{-5} and b equals 1.5×10^{-5}.

2.4 Discussion

2.4.1 KB08 model for alluvial stratigraphy simulation

Numerical modelling of alluvial stratigraphy has its clear limits when it comes to representation of true stratigraphic records (Hajek and Wolinsky, 2012). However, it is very useful to test a system's responses to changing boundary conditions, where outcrop analogue studies in many cases lack data and resolution. Specifically, from one field case to another, multiple boundary conditions change, and it is in many cases difficult for outcrop analogue studies to identify the dominant processes that have controlled the observed changes in the alluvial stratigraphy. In contrast, we can separate changes in boundary conditions to observe responses of the system to these changes through numerical modelling. Nevertheless, it is crucial to evaluate to what extent the numerical modelling results represent true alluvial processes and stratigraphic responses.

It is challenging for a single modelling tool to incorporate full temporal and spatial scales that autogenic and allogenic forcings operate over. The KB08 model employs a diffusion scheme to illustrate the stratigraphic patterns at a basin-filling time scale, which is much longer than a morphodynamic time scale (Paola et al., 2009). Therefore, the KB08 model likely underrepresents the stochasticity of the transport system, and the model tends to smoothen topography with the aim of algorithmic simplicity and computational economy. Yet, most morphodynamics occur at a channel scale, where the channels define the channel belt. In this study, we only focus on the channel-belt scale, assuming that intra-channel-belt morphodynamics will not significantly change the channel-belt morphodynamics. Modelling tools with layer-averaged Naiver-Strokes equations coupled to non-linear sediment transport algorithms, such as Delft3D, are superior in simulating shorter-time-scale morphodynamics, but they are not yet computationally feasible for simulation over basin-filling time scales that we aim to study.

In terms of our scenario setup about Q_w and Q_s forms, we always adopt a sinusoidal form of Q_w, based on the previous research that has shown that cyclic orbital forcing can result in cyclic precipitation variability, which further induces a similar time evolution of runoff that transmits the climate signal to the geomorphic system (Godard et al., 2013). For Q_s forms, Q_s signal is dependent on Q_w in Scenarios C10 and C20, following a non-linear rule, and this is consistent with the diffusive transport model (Whipple and Tucker, 2002), which assumes sediment flux to be a function of water discharge and river slope (Armitage et al., 2018; Forzoni et al., 2014; Nittrouer et al., 2012; Syvitski et al., 2000; Whipple, 2001). In amplitude- and wavelength-themed scenarios, Q_s signal is independent on Q_w, and this is partially in line with the advective stream power model (Willett et al., 2014), in which sediment is assumed to be supply- or detachment-limited. Specifically, the relationship between available sediment supply and the river transport capacity greatly influences the Q_s signal. When the available sediment amount is always smaller than the lowest river transport capacity, Q_s should match the erosion rate estimates that balance estimates of the long-term rock uplift rate (Armitage et al., 2018; Godard et al., 2013; Whipple, 2001; Zhang et al., 2018). However, no essential difference is observed among these scenarios with and without Q_s dependence on Q_w in our modelling results, in terms of regular alternation of aggradation and non-deposition phases, when they have similar Q_s/Q_w amplitudes and wavelengths (Figure 2.3 and Figure 2.9). Therefore, all our interpretations and following discussions are targeting the role of the Q_s/Q_w ratio.

In the KB08 model, different realizations of one scenario with identical boundary conditions show different outcomes. These variabilities are ascribed to the presence of stochastic components embedded in the model, which produce unpredictable model behaviors mimicking effects of autogenic forcing. Similarity between allogenic realizations with the same inputs is, however, robust at the allogenic forcing wavelength scale, in terms of regular alternation of aggradation and non-deposition phases. Therefore, we think the KB08 model helps elucidate the interaction between allogenic and autogenic forcing and thus serves well for the scope of our study.

2.4.2 Q_s/Q_w signal and modelled alluvial stratigraphy
Impact of cyclic versus non-cyclic Q_s/Q_w signal
Cyclic Q_s/Q_w forcing can drive the alluvial deposition through interaction with autogenic processes. An increases in Q_s/Q_w ratio results in immediate aggradation in the channel belt, and, depending on preceding floodplain topography, channel belt avulsions and aggradation over the width of the modelling basin will occur when the superelevation is reached. These aggradation and non-deposition phases are in pace with the imposed Q_s/Q_w ratio changes with sufficiently large amplitude and long wavelengths. In scenarios with short Q_s/Q_w wavelengths, we observe longer-time-scale basin-wide aggradation in addition to the shorter-time-scale aggradation as responses to Q_s/Q_w changes (panels A1, B1 and D1, Figure 2.10). In other words, there seem to be four longer-wavelength cycles in addition to the 32 short-wavelength (1.25 kyr) cycles that are expected based on the imposed Q_s/Q_w forcing. However, this longer-time-scale basin-wide aggradation does not occur in the fully autogenic scenario, which means this behavior is not intrinsic to the model creating superelevation of the channel belts over the alluvial plain at quasi-fixed time scales. It instead means that these long-term phases are a response to the imposed allogenic forcing. Our model runs are not long enough to statistically determine any stable frequency in these long-term basin-wide aggradation phases. It is beyond the scope of the current work to analyze this model character any further, which would need very long model runs with a range of high frequency forcing. For scenarios with long wavelengths, a similar model behavior is observed. Basin-wide avulsion and aggradation occurs not only in pace with the forcing, but also intermittently. Specifically, superelevation can be reached over a sufficiently long time period in the non-deposition phase of a long allogenic cycle, given the fact that the depositional rate in this phase is very low. Similarly, it takes shorter time periods for autogenically-controlled aggradation in the non-deposition phases to occur in small-amplitude scenarios (e.g. panels C1 and C2, Figure 2.9), due to the fact that channel belts are easier to be filled and super-elevated by within-channel aggradation in these scenarios. Therefore, we can conclude that, the model prefers basin-wide aggradation to occur under autogenic controls at a certain time scale that is long enough for channel belt aggradation to reach the superelevation. The exact time scale at which this autogenic behavior happens depends obviously on the allogenic forcing but also inherent model properties (e.g. basin subsidence rate, basin size, and basin slope).

Preservation and shredding of allogenic Q_s/Q_w signals
Preservation of allogenic signals in fluvial records requires either the allogenic signal to be relatively strong or the autogenic forcing to be relatively weak. The autogenic forcing

presents a compensational time scale of 2 kyr (Figure 2.4), which act as a low bandpass filter to prevent the allogenic signal from being preserved, known as the signal shredding effect (Hajek and Straub, 2017; Jensen and Pedersen, 2010; Straub and Foreman, 2018; Toby et al., 2019). As demonstrated in our KB08 model results, Q_s/Q_w ratios with larger amplitudes can better withstand signal shredding from autogenic dynamics. Based on Scenarios W1.25 and W2.5 (Figure 2.10), Q_s/Q_w ratios need to have sufficiently long wavelengths to prevent a cycle from being overprinted by the subsequent cycle. This is consistent with the argument about the maximum surface roughness proposed by Wang *et al.* (Wang et al., 2011), which highlights that the stratigraphic package should be thicker than the maximum channel depth in order to be preserved. Meanwhile, the Q_s/Q_w wavelength should not be too long, which will render the non-deposition phase subjected to autogenically-controlled aggradation (panels A5 and C5, Figure 2.10). In other words, although the depositional rate in the channel belt during a non-deposition phase is very low, super-elevation can be reached if the time is sufficiently long. The exact amplitude and wavelength thresholds between signal preservation and shredding again depend on the specific model setup, including basin size (Powell et al., 2012), basin subsidence rate, bank cohesiveness, and also measurement locality. As determined by the long-term accommodation, the long-term aggradation rates to a large extent also determine whether signals will be preserved or shredded (Foreman and Straub, 2017). With the current modelling results, we plot a tentative diagram to depict amplitude and wavelength thresholds between signal preservation and shredding for our model and scenario setup (Figure 2.11). In general, allogenic signals with large amplitudes and long, but not very long, wavelengths have large chances to be preserved in the alluvial stratigraphy.

However, it is worthwhile mentioning that these threshold values in Figure 2.11 are relative and they are not universally applicable to another modelled/real basin that has different properties. Moreover, there are many ideal situations in this study that potentially contribute to higher chances of signal preservation in this numerical exercise than those in reality. For instance, there is a perfect balance between average Q_s/Q_w ratio and basin slope and that between sediment supply rate (1.0×10⁶ m³/year), basin size (60 km by 40 km), and base-level rise rate (0.4 m/kyr). Moreover, the constantly rising base level provides continuously growing accommodation that would favor long-term aggradation, which also enhances the chances of signal preservation. Moreover, we have to mention that it is relatively more feasible to detect signals out of the modelled stratigraphy than the case in reality, because we have great control of time in the modelled basin and thus spectral analysis has an extremely high accuracy. The absent mass balance for floodplain aggradation plays a certain role in helping signal preservation, but its effect should be minor. Overall, it should be harder for field geologists to detect allogenic signals in the real basins due to complex natural conditions that might not synergy with each other in preserving allogenic signals.

Compensational time scales and autogenic forcing

The compensational time scale represents the time scale at which the floodplain roughness is levelled out over a certain segment of a sedimentary basin (Straub et al., 2009). There are many factors that can influence the compensational time scale, such as basin size, basin slope, magnitudes of sediment load (Q_{w0} in our study) and water discharge (Q_{w0} in our study) (Jerolmack and Paola, 2010; Powell et al., 2012; Straub and Esposito, 2013). As stated

2
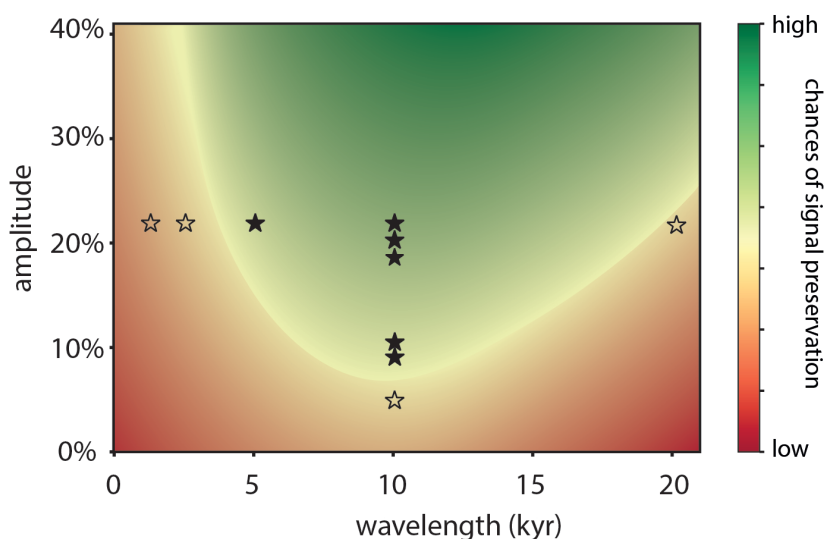
Figure 2.11: Amplitude and wavelength thresholds for Qs/Qw signal preservation. Hollow stars indicate shredded signals, while solid ones suggest preserved signals. Note that these threshold values are dependent on measurement localities and inherent properties of the modelled basin, and they can not be universally applied to all localities in all basins

above, the compensational time scale in a fully autogenic run can be very different from that in an allogenic run, due to interference of allogenic forcing on the autogenic behavior of river networks. For instance, during a non-deposition phase in an allogenic scenario that lasts longer than the compensational time scale in a fully autogenic scenario, channels are strictly confined within channel belts, which suppresses the inherent tendency of a transport system to level up topographic differences throughout the basin. This is consistent with the argument by Abels et al. (2013) that super–elevation during the overbank phase with low depositional rates will only be reached at sufficiently long timescales such that cyclic climate forcing may pace the changes between overbank phases and avulsion phases.

In general, a large forcing amplitude will suppress the tendency of a transport system to move laterally during the non-deposition phase, as the higher stream power with respect to sediment load causes confined, incisive channel belts (e.g. panel B4, Figure 2.10). How exactly the allogenic forcing with varied amplitudes and wavelengths interferes with autogenic forcing in producing different compensational time scales is beyond the scope of the current work, and it will be carefully evaluated in the future research.

2.4.3 Model-field comparison

In the KB08 model, Q_w and Q_s are set to represent the annual mean discharge and annual sediment load, respectively, and their ratio controls the fluvial graded profile. Increasing Q_s/Q_w ratio, either resulting from relatively decreasing water discharge to sediment load or relatively increasing sediment load to water discharge, contributes to overall regional-scale sedimentation in the model. In contrast, decreasing Q_s/Q_w ratio results in highly

organized channel belts eroding into the alluvial plain and bypassing sediments, as can be clearly seen in Scenario A40 (panel B4, Figure 2.9). This is in line with phenomena as reported by previous studies (Blum and Aslan, 2006; Demko et al., 2004). Deposition occurs in the model after the Q_s/Q_w ratio begins to increase, first filling the topographically low areas and then creating super-elevation (e.g. Figure 2.5C). With a time lag with respect to $(Q_s/Q_w)_{min}$, the aggradation phase takes place when lateral topographic gradients increase and super-elevation is sufficiently high. This is also in line with previous field studies (Mohrig et al., 2000; Slingerland and Smith, 2004).

In the KB08 model, during the time interval with decreasing Q_s/Q_w ratio, non-deposition phases occur on the floodplains with stable channel belts that only locally avulse or splay. Moreover, longer non-deposition phase, in the field context, contributes to generally more developed soil profiles. The modelled non-deposition phase seems to share similarities with the so-called overbank phase in the qualitative precession-forcing model of Abels et al. (2013) for the lower Eocene series of the Bighorn Basin, Wyoming, USA. The modelled non-deposition phase is characterized by relatively stable channel-belt locations and insignificant aggradation on the floodplain, and local avulsion may still occur. In the precession-forcing model, the overbank phase shows strongly-developed paleosols on floodplain fines that indicate long periods of non-deposition or low deposition (Abels et al., 2013). Field data concerning these floodplain cycles have so far only been gathered in floodplain strata. Therefore, it is not known yet whether these overbank phases coincide with the large-scale incision of the channel belt. Most overbank phases on the floodplains of the Bighorn Basin are however characterized by multiple soils that may be cumulative in nature (Kraus, 2002; Kraus and Gwinn, 1997). This means that small amounts of sediment arrive at these distal floodplain positions, also when channel belts have stable positions and possibly only splay and avulse locally.

In the KB08 model, during the time interval with increasing Q_s/Q_w ratio, sediment filling first takes place in the modelled channel belts, gradually leading to super-elevation and consequent frequent avulsion due to high depositional rates. The modelled aggradation phase resembles the so-called avulsion phase in the precession-forcing model of Abels et al. (2013). In the precession-forcing model, quickly avulsing channel belts at regional scale produce extensive sheet-like heterolithic avulsion–belt deposits (Abels et al., 2013), filling topographic differences between super-elevated channel belts and distal floodplains. In the KB08 model, the floodplain build-up continues as long as the Q_s/Q_w ratio keeps increasing; stratigraphic build-up with avulsion-belt deposition continues also when super-elevation is levelled out already. The duration of avulsion-belt formation has been a topic of investigation, as paleo-climatic data are needed to be set in sub-precession age models (Bowen et al., 2015; Wang et al., 2017). However, there are no ways to produce age models at a precision within a precession cycle for the Eocene or anywhere in the pre-Quaternary. Constraints on the relative duration of overbank and avulsion phases within the 21–kyr precession cycle remain dependent on present-day estimates of avulsion-belt deposition rates (Bowen et al., 2015). Wang et al. (2017) argued that the avulsion-belt deposition at one single location represents only 5%–10% of the precession cycle. According to Bowen et al. (2015), to produce the approximate 7-m-thick avulsion belt deposits, the duration of avulsion-belt formation should last between 3.5–14 kyr, that means, the avulsion duration accounts for 18%–70% of a precession cycle. In our model, the duration of an aggradation

phase is negatively correlated with Q_s/Q_w forcing amplitude, which varies between 40%-61% of a cycle wavelength for Scenario C20 (Figure 2.6B). Whether our results provide useful ways to constrain age models for ancient floodplain stratigraphy that are also used as paleoclimatic records (Abels et al., 2012; Bowen et al., 2015) remains to be resolved by more detailed 3D characterization of field data.

2.5 Conclusions

In this study, we evaluate the effect of cyclic and non-cyclic upstream forcing on alluvial stratigraphy using a process-based alluvial architecture model (Karssenberg and Bridge, 2008). We find cyclicity is preserved in the sedimentary records when the sediment load over water discharge (Q_s/Q_w) ratio has sufficiently large amplitudes and long, but not very long, wavelengths, the absolute values of which depend on inherent properties of the modelled basin. Within one allogenic cycle, there are a non-deposition phase and an aggradation phase. After the Q_s/Q_w ratio starts to decrease, the non-deposition phase occurs, during which channel belts are confined and stable at certain locations, and the vast floodplain undergoes very low sedimentation. The aggradation phase occurs after the Q_s/Q_w ratio starts to increase for a while, accompanied by sedimentary filling in the channel belt and creation of channel belt superelevation over the adjacent floodplains. Frequently shifting channel belts cause rapid sedimentation over the entire basin. The non-deposition and aggradation phases are comparable to the overbank- and avulsion-phases as identified in field successions in the Bighorn Basin, Wyoming, USA, which are attributed to precession-paced climate changes. In the KB08 model, larger forcing amplitudes result in longer non-deposition phases due to the fact that longer time is needed to fill the deeper-incised channel belts before superelevation can be reached. The upstream Q_s/Q_w signal is shredded in the downstream transmission process, and large amplitudes are more favorable for Q_s/Q_w signal preservation. We identify compensational time scales in the fully autogenic model runs by applying the method of Straub et al. (2009), and we find that the presence of an allogenic forcing will strongly influence the compensational time scale of a transport system. Findings of this study provide insights into the transmission and preservation processes of upstream cyclic Q_s/Q_w signals, during which allogenic and autogenic forcings interact with each other to produce alluvial stratigraphy.

2.6 Acknowledgement

2.7 Data availability

The data that support the findings of this study are archived and openly available at 4TU.Center for Research Data.

2

3

Floodplain aggradational cycles of the lower Eocene Willwood Formation

Here, 44 floodplain aggradation cycles were mapped and measured in 3-D using an unmanned aerial vehicle (UAV) to develop a photogrammetric model covering a geographic area of 10 km² and spanning a stratigraphic succession of 300 m. The 44 cycles have an average thickness of 6.8 m with a standard deviation of 2.0 m, which is in line with previous studies. Most cycles are consistently traceable over the entire model, indicating spatial consistency and in line with allogenic climate forcing by the astronomical precession cycle. Individual floodplain aggradation cycles may change in thickness rapidly when traced laterally, with rates up to 1 m over a lateral distance of 100 m and a maximum of 4 m. Detailed mapping of seven successive cycles reveals differences in their regionally-averaged thicknesses of 3.7 m to 9.7 m, with their coefficients of variation ranging between 17% and 28%. Variogram analysis demonstrates that the thickness of a cycle at one locality is statistically related to that at another locality over an average distance of 1.3 km in the paleoflow direction and 0.6 km perpendicular to the paleoflow direction. These different directional trends are interpreted to result from morphological elements oriented in paleoflow directions in the fluvial landscapes shaping more consistency of the sedimentary elements in paleoflow direction. Two different metrics suggest that full-compensational stacking occurs after deposition of 6 to 7 cycles, or timescales of ca. 120 to 140 kyr, although strong thickness compensation is shown to start at the subsequent one and two floodplain aggradation cycles, so at 40-60 kyr time scales.

3.1 Introduction

Alluvial stratigraphy is fundamentally controlled by channel avulsion frequency and long-term sediment accumulation rates (Allen, 1978; Ashworth et al., 2004) that are recorded by the distribution and configuration of channel sandstone bodies and coeval fine-grained sediment (Allen, 1978; Bridge and Leeder, 1979). Channel avulsion is an important process in channelized depositional systems. Channels aggrade or prograde faster than surrounding non-channelized regions (Hajek et al., 2012), causing avulsion to occur when a topographic threshold is exceeded. A difference is made between local and regional avulsion (Slingerland and Smith, 2004). A local avulsion may be triggered by simple channel blockage and has a local impact with the channel moving back into the original channel further downstream if that trajectory remains energetically most advantageous. A regional avulsion occurs when channels avulse at regional scales to a completely new trajectory on the floodplains. The threshold to drive an avulsion is defined as the critical slope ratio (Karssenberg and Bridge, 2008) or the superelevation of the channel belt over the floodplain (Jerolmack and Paola, 2007; Mohrig et al., 2000; Sun et al., 1996).

The rates at which superelevation is reached depend on channel belt and floodplain aggradation rates as well as non-deposition or degradation rates that may be different between channel belts and floodplains. Rates of aggradation or degradation depend on accommodation and sediment supply. Superelevation may be reached with all settings stable due to continuous higher aggradation rates in the channel belts than in the floodplains. River avulsions in these cases are fully autogenically controlled. Climate, tectonics, and base level may also impact these factors and speed up or slow down the rates at which superelevation is reached. Fluvial aggradational cycles have been reported in the Cretaceous-Paleogene of West Texas (Atchley et al., 2004), the Triassic of New Mexico (Cleveland et al., 2007), and the Eocene of northern Wyoming (Abels et al., 2013). These cycles are meter-scale, with typically fining-upward successions. They generally consist of two phases: (1) an overbank phase with relative channel stability and strong paleosol development on fine clastic sediments; and (2) an avulsion phase characterized by channel instability and weak to no pedogenesis on heterolithic sandy avulsion-belt deposits (Abels et al., 2013).

Most abovementioned fluvial aggradational cycles are reported to be driven by base-level variations, while those in the Eocene Willwood Formation of the Bighorn Basin in northern Wyoming are interpreted to be driven by precession-scale climate changes in multiple studies by indicating their duration to be around 20 kyr (Abdul Aziz et al., 2008; Abels et al., 2013; van der Meulen et al., 2020).

Previous Bighorn Basin Eocene studies have characterized and dated the climatically-driven cycles in various 1-D stratigraphic sections, including cycles in parallel sections separated by several kilometers (Abdul Aziz et al., 2008; Abels et al., 2013; van der Meulen et al., 2020; Westerhold et al., 2018). However, their 3-D characteristics, including their spatial consistency and variability, have not been studied. Lateral consistency of allogenically-driven cycles is expected, as external climate change would influence the whole basin at the same time. Local processes such as channel migration, local splaying, and avulsions are, however, expected to be an integral part of the dynamic fluvial environments and thus cause lateral and vertical variability on top of the regionally-consistent stratigraphy driven by external climate forcing. The spatial and temporal scales at which these local,

autogenic processes act and interact with regional, allogenic processes remain unknown, but crucial when these fluvial records are used for paleoenvironmental and paleoclimatic reconstructions (Straub and Foreman, 2018).

Here, we, therefore, analyze the precession-driven cycles in continuous outcrops of the lower Eocene Willwood Formation in the McCullough Peaks area of the Bighorn Basin, Wyoming, to reveal their spatial consistency and variability and to elucidate the spatial and temporal scales at which autogenic and allogenic controls interact and dominate. The objectives of this study are fourfold: (1) to investigate the traceability of cycles over a larger lateral distance; (3) to reveal the regionally-average vertical thicknesses and variability among individual cycles through the stratigraphy; (2) to characterize the lateral variability within each floodplain aggradational cycle; and (4) to evaluate compensational stacking through temporally-successive cycles. Finally, we aim to kinematically understand the fluvial morphodynamics that drive the dominant alluvial stratigraphy in the basin.

3.2 Geological Setting

The Bighorn Basin in Wyoming, USA, is a Laramide intermontane basin with a drainage outlet opening to the north (Figure 3.1). It hosts one of the best-studied terrestrial successions for fluvial cyclicity, with much research carried out on paleosols and river avulsion deposits (Abels et al., 2013; Bown and Kraus, 1981; Foreman et al., 2012; Kraus, 2002; Kraus and Aslan, 1993; Neasham and Vondra, 1972; Owen et al., 2017). Lower Eocene sediments of the Bighorn Basin exhibit regular alternations that have been related to the autogenic behavior that is intrinsic in a fluvial depositional system (Clyde and Christensen, 2003) and to allogenic forcing that is extrinsic (Abdul Aziz et al., 2008; Abels et al., 2013; Kraus and Aslan, 1993). Red/purple/grey paleosols are strikingly consistent over a large lateral extent (Kraus, 2002), and they are interpreted as products of the overbank phase (Abels et al., 2013). The paleoenvironments and paleoclimates in the basin have been extensively studied from floral and faunal fossils (Gingerich and Palasiatica, 2010) and using chemostratigraphic markers indicating the presence of the Paleocene-Eocene Thermal Maximum (Koch et al., 1992) and a series of early Eocene smaller hyperthermals (Abels et al., 2012, 2016). The mammal stratigraphy and data collections provide an accurate stratigraphy within the frame of the other stratigraphic controls as magnetostratigraphy, chemostratigraphy, and tephrastratigraphy (Clyde et al., 1994; Gingerich and Palasiatica, 2010).

The McCullough Peaks study area is in the northwestern part of the Bighorn Basin (Figure 3.1). The study interval here represents about 0.9 Myr of geological time straddling the interval in which the Eocene Thermal Maximum 2 and subsequent H2 events occur (Abels et al., 2016). The lower boundary is approximately 55 Ma, so about 1 Myr younger than the Paleocene-Eocene boundary marked by the Paleocene-Eocene Thermal Maximum (PETM). Fluvial strata in the study area have a dominant paleoflow direction of NNW to NNE (Neasham and Vondra, 1972).
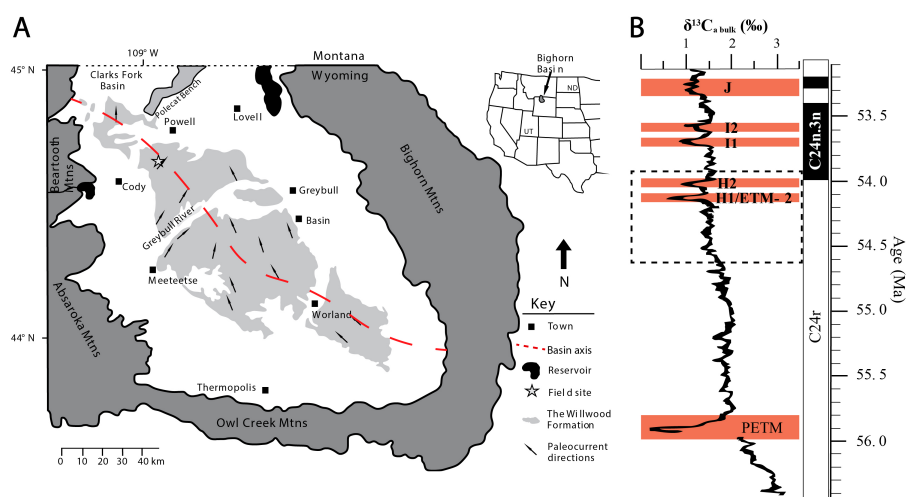
Figure 3.1: (A) The location of the study area, the McCullough Peaks, in the northern Bighorn Basin, Wyoming, USA (after Wang et al. (2017)). Paleoflow data indicated by the arrows are from Neasham and Vondra (1972). Note that the Washakie Range present during the Eocene is now covered by the Absaroka Mountains (Yonkee and Weil, 2015), and the Pryor Mountains present during the Eocene are now not distinguishable from the Bighorn Mountains (Blackstone, 1940). (B) Adjusted $\delta^{13}C_{a\ bulk}$ data from Zachos et al. (2010) by Birgenheier et al. (2019), with orange rectangles indicating hyperthermal events and the dashed rectangle indicating the study interval.

3.3 Methodology

3.3.1 Field survey

Stratigraphic sections were measured by digging 0.5-1 m wide and 0.5-1 m deep trenches down to fresh rock. Field units were designated based on field estimation of grain size; matrix color; abundance, size, and color of mottling; presence, abundance, and size of carbonate nodules; and abundance and size of slickensides. Hand sampling and field descriptions followed methods detailed in the Soil Survey Manual blue. Five long trenches were logged, with three reported in previous studies (Abels et al., 2012, 2013, 2016) and two reported here (see Figure 3.2 for trench locations). Palaeocurrent directions were measured from dune-scale cross-stratification (mainly planar and trough cross-stratification) in channelized sandstone bodies.

3.3.2 UAV-based photogrammetry

Photographs were taken automatically every three seconds by a 20-megapixel camera mounted on a multirotor unmanned aerial vehicle (UAV; DJI Phantom 4 Pro). The UAV was flown parallel to the outcrop surface manually at a speed of 5-10 m/s to provide a 60% horizontal overlap between successive photos. Each outcrop area was photographed from at least three different heights with different camera angles to provide complete coverage and to aid alignment during processing.

The final model includes 21144 photos taken on 34 flights (Figure 3.2), and it covers a total area of 10 km², with approximate north-south and east-west lengths of 2.5 km and 4 km, respectively. The studied stratigraphic succession is 300 m thick and dips at 2° towards
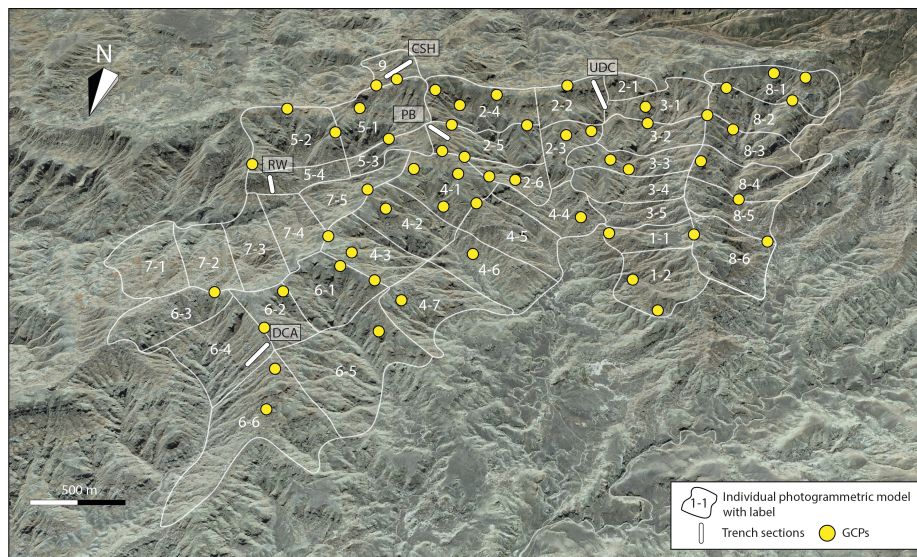
Figure 3.2: A bird's eye view from Google Earth showing the coverage of 42 individual photogrammetric 3-D models. Abbreviations: DCA–Deer Creek Amphitheater section(Abels et al., 2013), PB–Purple Butte section, UDC–Upper Deer Creek section(Abels et al., 2012), CSH–Creek Star Hill section (Abels et al., 2016), and RW–Roan Wash section.

the south. Fifty-seven ground control points (GCPs) were placed (see their localities in Figure 3.2) and surveyed using an Emlid Reach GNSS receiver, hereinafter referred to as the rover. Accuracy of GCPs was improved by using Post-Processed Kinematic (PPK) positioning technique which compares the rover-recorded GCP position to a second Emlid Reach GNSS receiver that acted as a stationary local base station. Both the rover and base station recorded raw GNSS measurements, which were then processed using the open-source GNSS post-processing package RTKLIB. The position of the base station was calibrated by collecting several hours of data and running the PPK solution against the nearest public Continuous Operating Reference Station (CORS) based in Fishtail, Montana (P722), which is run by the University NAVSTAR Consortium (UNAVCO). The GCP positions were then determined with centimeter accuracy relative to the local base station.

Agisoft PhotoScan (Version 1.4.3, July 2018; current Metashape) was used to build the 3-D digital models (virtual outcrops) from the acquired georeferenced photos. PhotoScan uses the structure from motion multi-view stereo (SfM-MVS) photogrammetric method for the reconstruction of an outcrop from multiple overlapping photographs (Eltner et al., 2016). Three-dimensional point clouds were generated in the Universal Transverse Mercator (UTM) coordinate system. Finally, a triangulated digital surface mesh was created, and the photos were draped onto the surface as the texture. Due to the large size of the area mapped, the complete photogrammetric image set was split into 42 model sections. For each section, a tiled model was generated based on a previous algorithm (Buckley et al., 2008), allowing the entire 3-D outcrop model to be imported into LIME (version 2.2.2) for visualization and interpretation (Buckley et al., 2019).
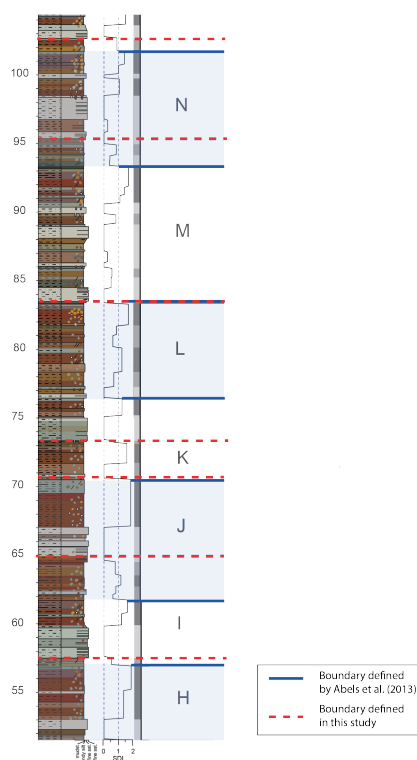
Figure 3.3: Comparison between cycle boundary in this study (red dash line) and that in Abels *et al.* (2013) (blue solid line), taking cycles H-N as examples.

3.3.3 Cycle boundary identification

Cycle boundary tops are placed at the sharpest facies transition from red/purple paleosols to whitish heterolithic deposits (Figure 3.3). This is slightly different from the procedure of Abels et al. (2013) who put cycle boundaries at the sharpest transition in the soil development index (SDI) curve, which in many cases corresponds to the top of the reddest soil. The cycle boundary of this study is in most cases slightly higher (0.6 m on average and up to 3.5 m for the seven cycles shown in Figure 3.3) than that of Abels et al. (2013). The reason for the chosen strategy is the impossibility to calculate SDI without non-weathered rock surface descriptions from trenched sections. Interpretation in the photogrammetric model is started from trenched sections (see their localities in Figure 3.2), where fresh rock descriptions are available such that the weathered exposures can be compared to the fresher surface descriptions. During this process, UAV- and hand-held camera-captured photos are used to aid interpretation where the model resolution is not sufficiently high.

3.3.4 Variogram analysis

As has been widely used to quantify variables in space, the variogram is a function of variance over lag distance h, with larger variogram values corresponding to longer lag
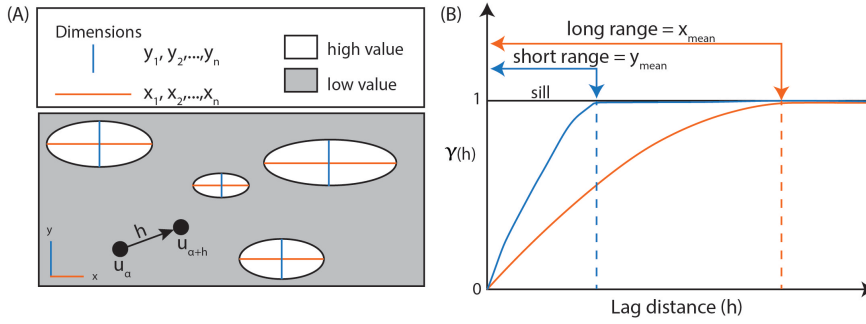
Figure 3.4: Schematic illustration of variogram components (modified from Pyrcz & Deutsch, 2003). (A) There are lenses with high values in the low-value background, with various long axes ($x_1, x_2,...,x_n$, averaging x_{mean}) and short axes ($y_1, y_2,...,y_n$, averaging y_{mean}); (B) The long and short ranges corresponding to x_{mean} and y_{mean} of high-value lens in Figure 4A, and observations appear independent (i.e. variance no longer increases) when the lag distance is beyond the range.

distances (Figure 3.4). A variogram can be calculated as follows (Pyrcz and Deutsch, 2003):

$$\gamma(h) = \frac{1}{2N(h)} \sum_{\alpha}^{N(h)} (z(u_\alpha) - z(u_{\alpha+h}))^2 \qquad (3.1)$$

where $\gamma(h)$ is a measure of dissimilarity over distance, which is a spatial variance between two data points separated by lag distance h representing the separation between two data points; $N(h)$ is the number of data point pairs separated by distance h; u_α is a data point at location α in 2-D space; $u_{\alpha+h}$ is a data point separated from u_α by the distance h; $z(u_\alpha)$ is the numerical value at data point u_α; and $z(u_{\alpha+h})$ is the numerical value at data point $u_{\alpha+h}$.

Cycle thicknesses are measured on outcrop surfaces in the model every 20 meters, which could be impossible at some locations due to vegetation, low model resolution, and recent debris. These thickness measurements are then analyzed as a 2-D directional variogram using Python codes by Pyrcz (2020). Variograms are calculated in six directions that separate 180° into six equal azimuth zones (e.g. 0°, 30°, 60°, 90°, 120°, and 150°) after observation of any statistical anisotropy in the variogram map. The lag distance is set as 100 m, with a lag tolerance of 50 m. The search strategy utilizes a wide azimuth tolerance (30°) and a large bandwidth (2 km) to reduce the nugget effect near the origin (Zhang et al., 2005). In a directional variogram, a range is identified when the sill ($\gamma(h) = 1$) is reached (Figure 3.4). Within the range, the cycle thickness at one locality is related to that at another locality, which is referred to as the spatial continuity of the cycle thickness. Such continuity is expected to be the largest in the paleoflow direction (Pyrcz and Deutsch, 2014).

3.3.5 Compensational stacking analysis

Coefficient of variation (CV)
The coefficient of variation (CV) is defined as the ratio of the standard deviation over the mean. If the thickness of a stratigraphic unit like an cycle has a small CV, then the thickness of the unit has an even distribution throughout the area. To investigate compensational stacking, successive cycles are combined as a stratigraphic unit to calculate CV. Seven successive cycles with high lateral coverage in the model, labelled as cycles H to N, are selected for this analysis. In practice, a CV is first calculated for the thickness of one cycle (e.g., cycle H), followed by calculation of a CV for the thickness of two successive cycles combined (e.g., cycles H and I), then three successive cycles (e.g., cycles H, I, and J), ..., and finally a CV for all of the available cycles combined.

Compensational stacking index (σ_{ss})
Compensational stacking index (σ_{ss}) has been introduced in Chapter 2, and it is defined as the standard deviation of sedimentation/subsidence to characterize the compensational timescale (Wang et al., 2011):

$$\sigma_{ss}(T) = \{\int_a^b [\frac{r(T;x)}{\hat{r}(x)} - 1]^2 \, dL\}^{1/2} \tag{3.2}$$

where $r(T;x)$ is the average deposition rate at a horizontal coordinate of x along a certain cross-basin line during a time interval of T, L is the cross-basin length, and $\hat{r}(x)$ is the local long-term sedimentation (or subsidence) rate.

Empirically, σ_{ss} is expected to decrease as T increases, following a power-law trend (Straub et al., 2009; Wang et al., 2011):

$$\sigma_{ss} = a' T^{-\kappa} \tag{3.3}$$

where a' is a coefficient, and the exponent, κ, is termed the compensation index. At a certain time scale when κ exceeds 1.0, the stratigraphic stacking is purely compensational (Straub et al., 2009). However, we have to note that it is impossible to make many long 1-D sections that span the whole stratigraphy due to the limitation of outcrop exposure and the presence of channel sandstone bodies and vegetation. With this metric, the compensational stacking is explored using only one 1-D composite section.

3.4 Results

3.4.1 Cycle traceability and composite stratigraphy
A total of 44 cycles are identified throughout the studied 300-m stratigraphy in the model, and their boundaries are well recognizable stratigraphically and traceable laterally. Local factors might hinder lateral tracing, such as occurrences of channel sandstone bodies, splitting or merging of soil horizons at the stratigraphic interval of the recognized boundary, recent debris and vegetation over the outcrops, and the low resolution of the photogrammetric model in some places. Cycle boundaries are traced in the photogrammetric model (see Figure 3.5). The full model will become available through V3Geo.com as early as Spring 2022 due to confidentiality reasons.

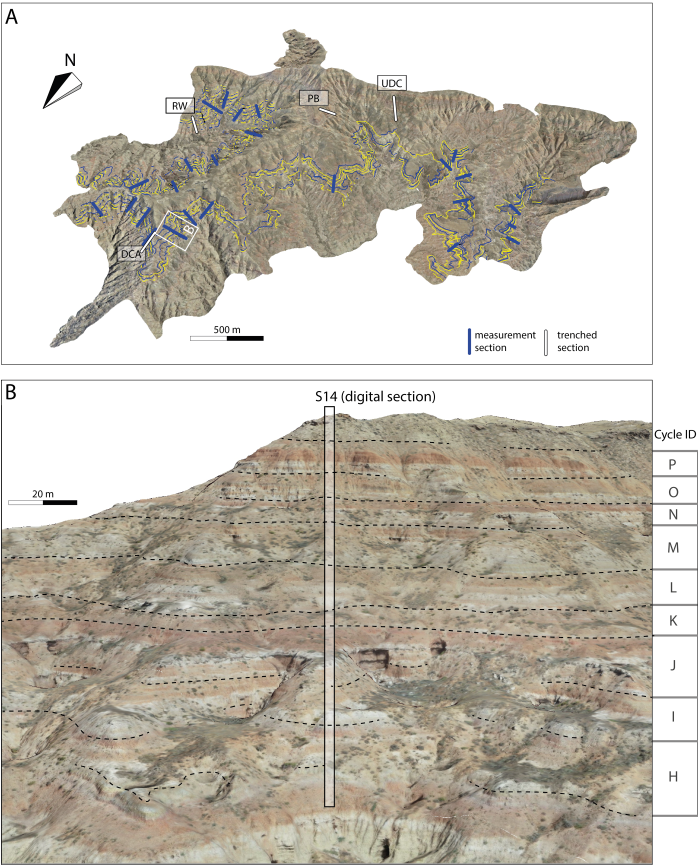Figure 3.5: Tracing of cycles in the photogrammetric model with the aid of individual drone and camera photos. (A) An overview of the interpreted 3-D photogrammetric model in the McCullough Peaks area, showing traced boundaries (blue and yellow lines) for seven successive cycles. (B) A zoomed-in outcrop section in the 3-D model, showing how cycle boundaries are traced and how a digital section (S14) is constructed.
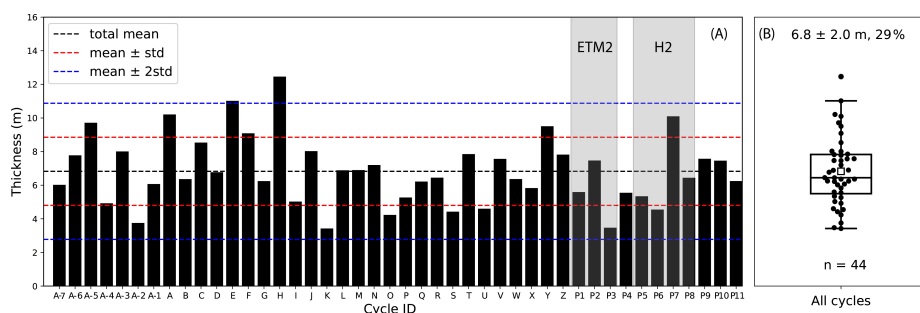
Figure 3.6: Thicknesses of 44 cycles in the composite stratigraphy. (A) Bar diagram showing the new labeling system and the variability of the cycle thickness in a 1D composite stratigraphy. (B) Boxplot showing the thickness variability of these 44 cycles. Box boundaries indicate lower and upper quartiles, lines extending from boxes represent the 1st to 2nd and 3rd to 4th quartile ranges, lines and squares within boxes indicate the median and mean values, and points outside the boxes stand for outliers. The number combination of "a ± b (c)" above the boxplot means "average ± standard deviation (CV)".

The stratigraphy in which the 44 cycles are recognized starts 7 cycles below the base of the Deer Creek Amphitheater section of Abels et al. (2013) and ends at/above the top of the Upper Deer Creek section of Abels et al. (2012) and Creek Star Hill section of Abels et al. (2016). The lower 10 cycles and upper 11 cycles have limited lateral extents within the photogrammetric model. Most of the other cycles can be traced over a maximum distance of 4 km in the NE-SW direction and 2.5 km in the SE-NW direction. A composite section that includes all of the 44 cycles is constructed by combining available trenched sections (DCA and UDC sections). We have extended the cycle labeling system of Abels et al. (2012, 2013) rather than starting a new one (see Figure 3.6A). cycles P1 to P3 correspond to the hyperthermal ETM2 and cycles P5 to P8 correspond to the hyperthermal H2 (Figure 3.1).

The composite stratigraphy with 44 cycles has a cumulative thickness of 300 m (Figure 3.6A), which is based on 1-D data and thus no regional averages of cycle thicknesses are included. The thickness of an individual cycle ranges between 3.4 m and 12.5 m. Their average, which we are referring to the arithmetic mean here and hereinafter, is 6.8 m, with a standard deviation of 2.0 m (Figure 3.6B).

3.4.2 Lateral thickness variability of individual cycles

Detailed mapping of cycles H to N shows that individual thickness measurements range between 2 m and 18 m with CV ranging between 17% and 28% (Figure 3.7), and regional average thicknesses of cycles H to N vary between 3.7 m (cycle K) and 9.7 m (cycle L). The average of all cycle thickness measurements is 7.3 m with a standard deviation of 2.6 m (Figure 3.7). These numbers are comparable to those calculated for all 44 cycles in the 1-D composite section (6.8 ± 2.0 m, Figure 3.6B) and previously reported values.

We make a total of 22 digital sections in the photogrammetric model, such as section 14 (S14) in Figure 3.5B. The top cycles are flattened in Figure 3.8, in which cycle thicknesses vary rapidly in the lateral direction, with a maximum of 4 m over a distance of 400 m.
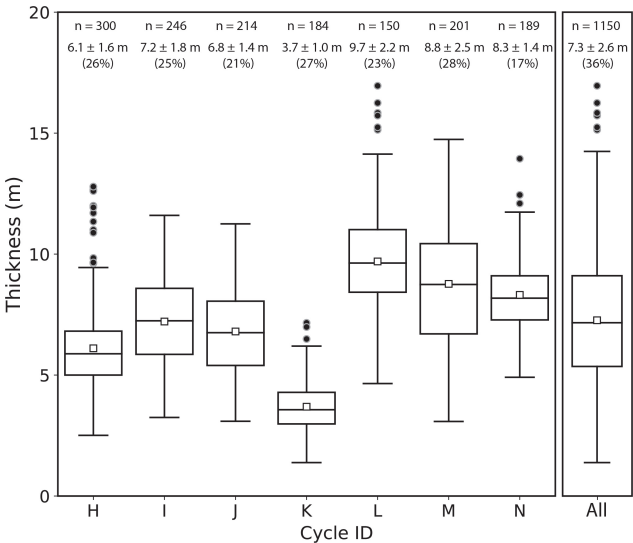
Figure 3.7: Box plots illustrating the variability of the thicknesses of cycles H-N. The very right boxplot is based on 1150 measurements that are equally contributed by the seven cycles by randomly selecting 150 measurements from each floodplain aggradational cycle. See explanations of boxplot components in Figure 3.6.
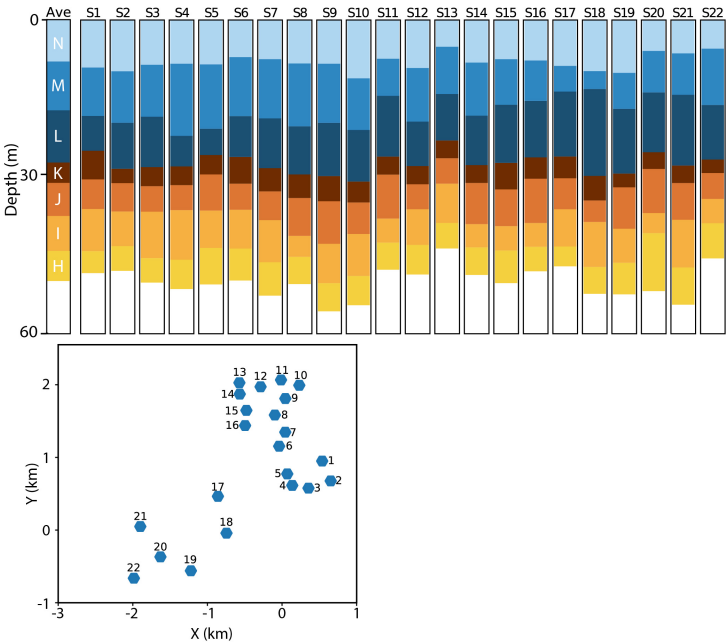
Figure 3.8: Variation of cycle thickness in the lateral extent. The lower panel shows locations of 22 digital sections, while the upper panel shows the thickness variations of seven successive cycles, with the top cycle flattened. Note that the coordinates in the lower panel are converted from global UTM coordinates to local ones, with applied offset of X_{offset} = 673000 m and Y_{offset} = 49242600 m.

3
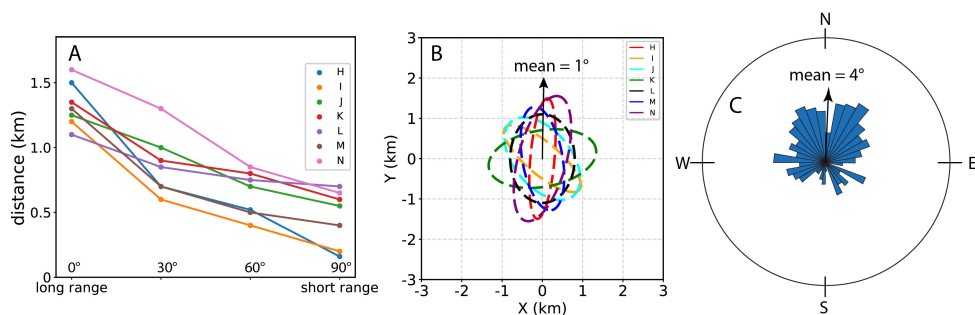
Figure 3.9: (A) Variation of ranges with azimuth, assuming the long-range azimuth to be 0° and thus the short-range azimuth to be 90°. (B) Oriented variogram ellipses with long and short ranges as long and short axes. (C) Field-measured paleoflow directions in the dune-scale cross-stratifications.
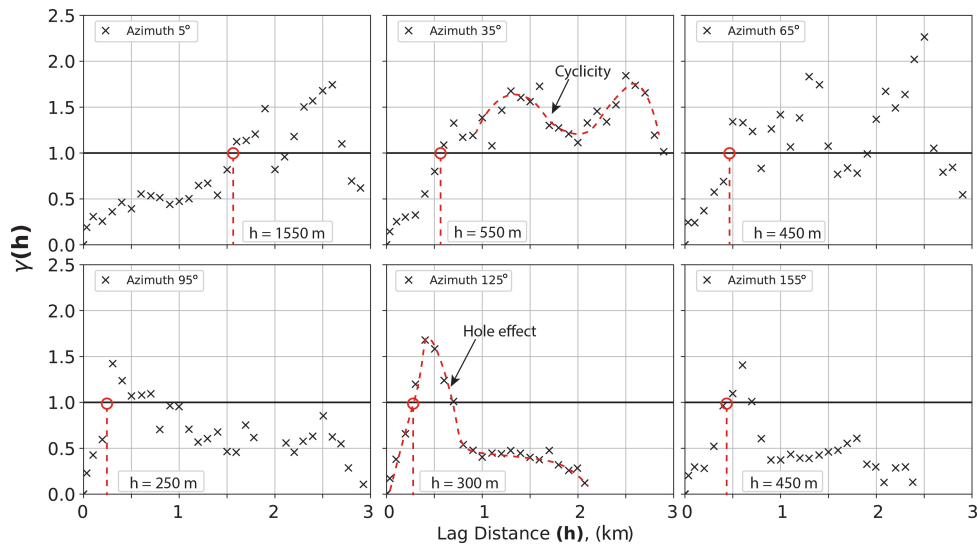
Figure 3.10: One-dimensional directional variograms for cycle H with different azimuths. Red circles and lines indicate the ranges along different azimuths. Information on how to read variograms has been detailed in Section 3.4.

Variograms are calculated for the seven cycles to indicate the correlativity of the cycle thickness at one specific location to that at another over a certain distance. The correlatable distance is on average 1.3 km in the long-range direction (see its definition in Section 3.4) and 0.6 km in the short-range direction (Figure 3.9A). The aspect ratio of the variogram ellipse varies between 1.4 to 5.3, with an average of 2.2. The long-range azimuth ranges between 310° and 80°, averaging 1° (Figure 3.9B), which coincides with the average paleoflow direction measured in the dune-scale cross-beddings in the field (4° ± 24°; Figure 3.9C). Individual 1-D variograms show repetitive, non-monotonic features (e.g. Figure 3.10B), which are referred to as cyclicity by Pyrcz and Deutsch (2003). Meanwhile, there are also non-monotonic variograms that don't present repetitive patterns (e.g. Figure 3.10E), which, together with the above-mentioned cyclicity, are referred to as the hole effect (Pyrcz and Deutsch, 2003).

3.4.3 Vertical cycle stacking

A locally thicker cycle seemingly tends to stack on a locally thinner cycle and vice versa. Examples are the thicker-than-average cycle L and the thinner-than-average cycle M in Section S18 of Figure 3.8. To quantify this compensational stacking behaviour, two metrics are used. For the first metric, we compile the thicknesses of individual cycles and divide the thickness by their average. Now, the standard deviation of each cycle thickness is equivalent to its CV since the average is 1. Subsequently, the CV of two successive cycles at individual locations as a stratigraphic unit is calculated (Figure 3.11). This shows a significantly reduced CV from 23% to 14%, a reduction of 53% of the total CV reduction (numerically calculated as (23% - 14%)/(23% - 6%)). Stacking three cycles at individual locations reduces the CV by 76% to 10%. The CV does not decrease further than 6% when 6 successive cycles are stacked.

For the second metric, we calculate σ_{ss} using the composite section shown in Figure 3.6 based on the method described in Section 3.3.5. The predicted compensational timescale is identified by drawing two green dashed trend lines representing best-fit linear regression of the dots before and after the knick point. Thus, the predicted compensational timescale corresponds to 7 cycles, although the slopes on both sides of the knick point are quite similar. According to the method, this indicates stratigraphic stacking becomes fully compensational after deposition of 7 cycles (Figure 3.11).

3
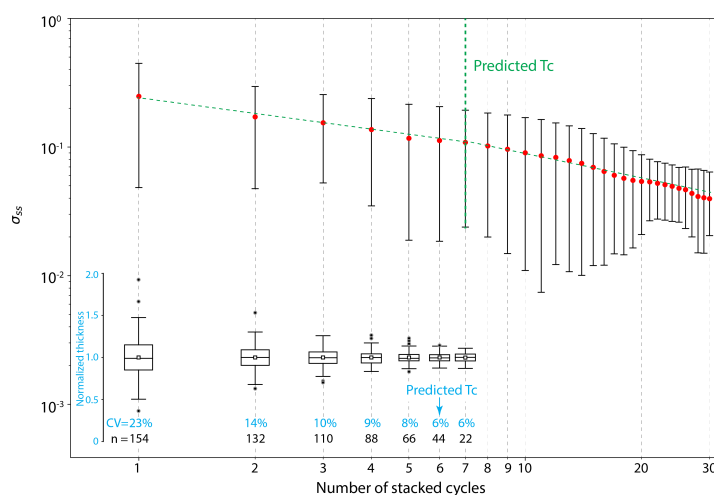
Figure 3.11: Two metrics for indicating the compensational timescale (Tc). (1) The lower part shows the decay of CV of the thicknesses of seven cycles with an increasing number of cycles. The predicted Tc corresponds to about 6 cycles since CV doesn't reduce anymore after the number of stacked cycles reaches 6. (2) The upper part shows the decay of σ_{ss} with an increasing number of cycles in the composite section (Figure 3.8). Error bars represent the geometric standard deviation, red dots indicate the average σss at the corresponding number of cycles, green dashed trend lines represent best-fit linear, and the vertical green dashed line indicates the predicted Tc (see Section 3.3.5 for more detailed explanation of the principle) that corresponds to 7 cycles, over which the stratigraphic stacking transits from anti-compensational to compensational form.

3.5 Discussion

3.5.1 Floodplain aggradational cycles – lateral Consistency

Floodplain aggradational cycles are dominant features of alluvial stratigraphy in many alluvial records (Abels et al., 2013; Kraus and Gwinn, 1997). They are related to phases of river stability and deposition of true overbank fines on which strong paleosols may develop and phases of regional-scale river avulsion causing deposition of the heterolithic avulsion belt on which weak or no soils develop (Abels et al., 2013; Kraus and Aslan, 1993). In the Bighorn Basin, the cycles have been linked to precession-scale climate change (Abdul Aziz et al., 2008; Abels et al., 2013, 2016; van der Meulen et al., 2020) although the climatic model (e.g. precipitation, temperature, vegetation) remains enigmatic.

At least six different stratigraphic sections of three different intervals of time in the Bighorn Basin have now revealed similarly-thick cycles (Abdul Aziz et al., 2008; Abels et al., 2013, 2016; van der Meulen et al., 2020; Westerhold et al., 2018). Previously, lateral consistency was only demonstrated in two 1-D parallel sections spaced 7.5 km with correlations confirmed by carbon isotopes (van der Meulen et al., 2020). Consistency over 15 km was suggested by Westerhold et al. (2018), which, however, could not be independently confirmed by stratigraphic constraints. Here, we demonstrate lateral consistency of individual cycles over a 10 km² area and a maximum length of 5 km approximately in the paleoflow direction. We also demonstrate cycle to be a consistent component of alluvial stratigraphic build-up over nearly 1 Myr in the lower Eocene Willwood Formation with

44 cycles stacking to make ~300 m stratigraphy. The lateral consistency of cycles found in this study, the continuity in stratigraphy in line with all available dating pointing at cycle occurring at precession-time scales, and all previous documentation of the cyclicity and dating, strongly confirm their allogenic nature. We think there can be placed little doubt at that cycles in the lower Eocene infill of the Bighorn Basin are driven by precession-forced climatic changes.

Longer-term aggradation rates depend on the accommodation creation, which, in the case of the Bighorn Basin where sea/lake-level variation is absent, is related to tectonic subsidence. Abels et al. (2013) argued that reaching superelevation was likely at pace with the accommodation space creation by tectonic subsidence and precession-driven climate changes. This means that the long-term average cycle thickness would approach the long-term basin subsidence. If all these 44 cycles with an average thickness of 6.8 m are driven by precession cycles with a duration of ca. 20 kyr, the estimated basin subsidence rate equivalent to the long-term sedimentation rate would be 0.34 m/ky. This is in line with previous estimates of 0.29-0.39 m/kyr (Abels et al., 2012, 2013; Clyde et al., 1994; Gingerich and Palasiatica, 2010; Stap et al., 2009; Westerhold et al., 2007). Also, subsidence rates and aggradation rates were relatively constant over long periods of time, as suggested by previous research based on stable carbon isotope dating (Abels et al., 2016). At the Paleocene-Eocene transitional interval, cycles are reported to be slightly thicker, reaching an average of 8 m per cycle (Abdul Aziz et al., 2008; van der Meulen et al., 2020). In other words, the thinner Willwood Formation cycles may indicate slowed tectonic subsidence during the early Eocene (Abels et al., 2016; van der Meulen et al., 2020).

In numerical forward model runs, Wang et al. (2021c) found that very short forcing cycle wavelengths may render channel belts unable to reach superelevation in time, and thus not all individual forcing cycles can cause regional avulsion phases, but instead, avulsion phases occur every second, third, or fourth cycle. These authors also found that very-long forcing cycle wavelengths may cause the superelevation to be reached in the overbank phase and thus accelerate the entrance of the system into the avulsion phase. There may however be a range of intermediate wavelengths, where the system maintains its behavior for some time until the trigger occurs. The balance between subsidence, sedimentation, and climate change time scales, may in that sense be less critically exactly coinciding. Instead, the fluvial systems may maintain themselves at a certain state for some time, slowly building up stratigraphy; fluvial changes may occur if a strong climate trigger occurs during that time.

It remains enigmatic what climate triggers produce the cycles in the Willwood Formation. Likely, this had to do with sediment supply, both amount and type, and discharge hydrograph. Wang et al. (2021c) produce regional avulsion and overbank phases in a diffusion-based numerical forward stratigraphic model. In their model, increasing sediment supply relative to water discharge causes sediment accumulation in the channel belt and speeds up the time to superelevation, after which regional-scale avulsion occurs. In comparison, during the interval of decreasing sediment supply relative to water discharge, the channel belts are incisive and overbank deposition occurs (Wang et al., 2021c). Within the Bighorn Basin, climate changes may have also strongly impacted groundwater levels and vegetation types and intensity, which may also play important roles.

The average thickness of 44 stacked cycles in the 1-D section (6.8 m) and that of 7 suc-

cessive cycles that are mapped in the whole 3-D space (7.3 m) are quite similar. However, the individual cycle of the seven cycles analyzed show different thicknesses also when averaged over the entire width of the study area. We think this can be because of two different reasons. The first is that not all precession cycles are of the same wavelength. Typically, insolation curves show intervals of more pronounced cyclicity in the vicinity of eccentricity maxima and intervals of less pronounced cyclicity in the vicinity of eccentricity minima. In the latter parts, obliquity in many cases plays a more important role. Also, precession frequencies are more than a simple 20-kyr sine wave (Berger et al., 1992), which causes a relative variability in the forcing and thus may drive thicker and thinner cycle in terms of the regional average thicknesses (Figure 3.7) in response to shorter or longer insolation cycles. But, second, we cannot know yet whether the spatial consistency and variability of cycles recorded in our study area (~10 km²) is indeed a regional-scale representation. Thinner cycles may display thickening features outside the study area. We think the current size of the study area is large enough to deduce conclusions about lateral consistency and variability of the floodplain aggradational cycle, but we cannot exclude that (slightly) different numbers pop up when larger areas are analyzed.

3.5.2 Floodplain aggradational cycles – lateral variability

Thicknesses of individual cycles may change rapidly in the lateral direction with rates up to 4 m over a lateral distance of 400 m (Figure 3.8). It should be noted that all of the geometries discussed here are derived from compacted stratigraphy. Part of the variability that is measured likely relates to differential compaction between different lithologies. We did attempt to decompact cycles and reconstruct these differential thicknesses but we were so far unsuccessful, as we found out this requires detailed information on early-stage consolidation and later-stage compaction and the exact rates of these. Differential early-stage consolidation may cause higher or lower sedimentation in different areas and thus influence the subsequent thicknesses of stratigraphy, while late-stage compaction does not impact sedimentation. We envision that a backstripping exercise with active sedimentation and thus knowledge about rates of sedimentation depending on topography is needed to decompact the succession and reconstruct the paleotopography. That is clearly beyond the scope of the current work. Therefore, all the results we present and discuss are of compacted stratigraphy.

The thickness variability at local scales are obvious for all the seven cycles detailed mapped within the 10 km² study area, and this is related here to morphologic variability within the fluvial system in combination with differential compaction as discussed above. Morphologic elements in the fluvial landscape are major and minor channel belts, crevasse splays, levees, and floodplains. These caused different rates and types of sedimentation in different areas, which thereby results in topographic gradients between them. Major channels elevate above the landscape just before avulsion and the sands receive little consolidation afterward compared to the clays of the surrounding floodplains. With that, major and to some extent likely minor sandbodies will result in topographic highs in the subsequent cycle causing less sediment to arrive at those locations. Thicker-than-average cycles at some localities are mostly dominated by crevasse splay sediments, and overlying sediments are finer and mostly dominated by distal floodplain soils. How this results in compensational stacking will be discussed in Section 3.5.3. Typically, such lateral mor-

phological changes and related consolidation differences explain the thickness variations between allogenically-driven cycle boundaries.

The spatial continuity of the cycle thicknesses is stronger in the direction of paleoflow than that perpendicular to paleoflow (Figure 3.9). This could be indicative of how flood-plain deposits are morphologically segmented by single or stacked channels oriented into the downstream direction. Moreover, the morphological effect of channel segmentation could depend on the fluvial styles, as the number of river threads and the frequency of flooding and splaying will impact floodplain variability. The cyclicity and the hole effect found in the variogram analysis (Figure 3.10) could be related to channel-segmented blocks that are expressed as depressions or topographic highs (Pyrcz and Deutsch, 2003).

We analyze, using similar methods, the numerically-modelled stratigraphy in the KB08 model of Wang et al. (2021c). In Scenario A40 of Wang et al. (2021c), water discharge and sediment input are fed cyclically with a wavelength of 10 kyr and an amplitude of 40%, which produces four sedimentary cycles that mimic those in the Bighorn Basin. Vari-ogram analysis is implemented using the thickness map of the third cycle in the center of the basin to avoid the too strong impact of either upstream or downstream factors (Fig-ure 3.12). Interestingly, we find a long range of 22 km in the direction of paleoflow and a short range of 6 km perpendicular to paleoflow in the cross-basin direction (Figure 3.12D). The hole effect is also present in the variogram of the modelled stratigraphy (e.g., azimuths 30° and 120° in Figure 3.12D), which have similar characters to those based on the field data (Figure 3.10). It should be noted that the modelled strata are free of compaction while the field counterparts are not. The hole effect seems to be related to the presence of various depressions such as the blue low-thickness areas in Figure 3.12C or topographic highs such as the red/yellow high-thickness areas in Figure 3.12C. The lows and highs in mod-elled stratigraphy result from the segmentation of floodplain fines by channel belts that represent the finest resolution of the numerical model and could represent channels in the field. The similarity between the numerical model and the field data in terms of variogram features might indicate similar spatial features of cycles as shaped by the (modelled/real) fluvial processes.

3.5.3 Compensational stacking of floodplain sedimentation

Compensational stacking refers to the tendency of a depositional system to fill the lows and remove the highs in topography (Straub and Pyles, 2012; Straub et al., 2009). In other words, relatively high or low topography in the local areas will lead to local higher deposi-tion or erosion rates during the formation of subsequent and overlying cycles. Therefore, compensational stacking is expected to significantly reduce the topographic differences if the depositional time is sufficiently long, which means the smoothing effect of the later deposited cycles is much larger than the newly introduced morphological variability. Sev-eral other factors are also influential, in particular the early consolidation effect that may result in variable topography that was originally flat but had different soil characters. For example, sandstone bodies remain highs in the landscape as these consolidate less, while floodplain clay or even peat eventually produce lows in the landscape as these relatively consolidate more. Therefore, we attribute the compensational stacking found in this study to be the result of both fluvial morphology and compaction. In section 3.5.2, we have dis-cussed why decompaction at these scales has been unfeasible within the current study.
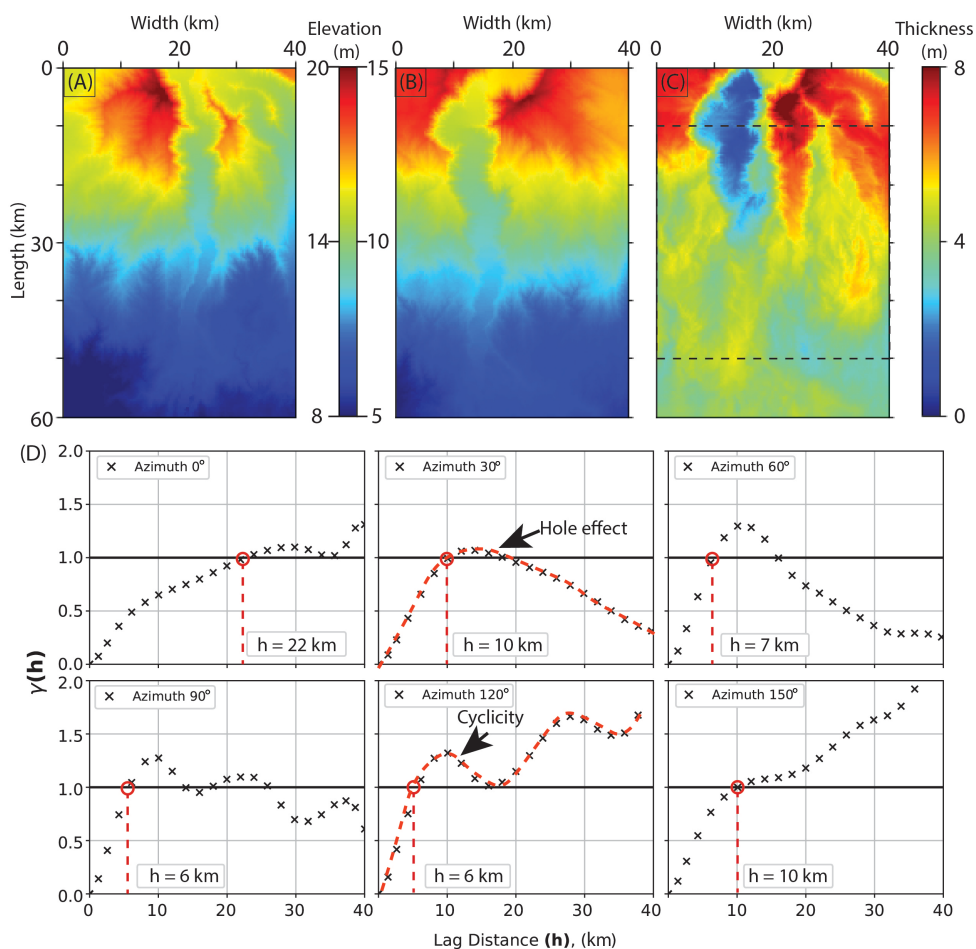
3

Figure 3.12:   Geostatistical analysis using the Scenario A40 data produced by Wang et al. (2021c). (A) The elevation map of the base of cycle 3. (B) The elevation map of the top of cycle 3. (C) The thickness map of cycle 3. (D) Directional variograms using the data constrained in the red rectangular of Figure 13C.

Two metrics (i.e., CV and σ_{ss}) point to full compensational timescales corresponding to 6 and 7 cycles (i.e., ~120-140 kyr), respectively. However, 54% compensational stacking is already reached in the subsequent first cycle and 76% in the subsequent two cycles. The remaining 23% compensational stacking occurs when the stacked cycle number increases from 3 to 6 (CV drops from 9% to 6%). These numbers are similar, while they are based on different methods applied to different datasets. The CV metric is based on measurements of the lateral thickness data of seven cycles in 22 digital sections over the whole study area, whereas the compensational index method is based on a long 1-D composite section lacking lateral data. The CV metric is favored because of the underlying 3-D dataset, but it comprises a limited stratigraphic interval. The compensational index method is based on a very long sedimentary record (~300 m), but it is applied in a 1-D dataset instead of a 3-D one. Therefore, the timescales we obtain here await examination by both spatially wider and stratigraphically longer dataset.

The compensational timescales corresponding to 6 and 7 precession cycles are longer than those identified in previous research, such as the 2.0 kyr timescale (artificial time scale in the model, equivalent to 1/5 of the acted 10 kyr cyclic forcing) in the fully autogenic numerical scenario of Wang et al. (2021c) as well as the 67 kyr, 100 kyr, and 55 kyr timescales based on the estimation of the maximum channel belt sandstone body thickness and the long-term sedimentation rate in the Bighorn Basin, Piceance Creek Basin, and Trem-Graus Basin (Straub et al., 2020). This difference can be explained by the fact that the basic stratigraphic units used in our study are different from those in the aforementioned studies. Straub et al. (2020) use decennial to centennial-scale intervals as their basic stratigraphic units, which implies the availability of high-resolution data, while we use precession-driven cycles as the basic stratigraphic units, which implies low-resolution data. This finding is in line with the previous study (Straub and Pyles, 2012) that compensational stacking is prevalent at various hierarchical scales. Straub and Pyles (2012) pinpointed that units as small as individual channel beds are compensating the topographic differences created by older beds, whereas units of channel stories and higher hierarchy (i.e. channel element and channel complex) are also compensating during their stacking. Nonetheless, the compensational timescales identified in this study and other studies are not universally applicable for all basins that record precession-scale cyclicity, since it depends on several site-specific factors, such as sediment supply, basin size and slope, base-level fluctuation, and subsidence-caused accommodation changes. Moreover, we also find that considerable, though not full, compensational stacking already occurs as the subsequent cycle gets deposited, which is evidenced by the sharp reduction of CV from 23% to 14% (Figure 3.11). Furthermore, Wang et al. (2021c) showed that the compensational timescale in an allogenically-involved scenario (such as C10 and C20) is about 2.6 times of that in the fully autogenic scenario, which indicates the interference of allogenic forcing on autogenic processes.

3.5.4 Disentangling autogenic and allogenic forcing

One of the goals of this study has been to disentangle allogenic from autogenic sedimentation in the alluvial succession of the Bighorn Basin. With the laterally-consistent, precession-driven floodplain aggradation cycles, the successions display a strong impact of allogenic, cyclic forcing. Autogenic processes, as local splaying or avulsion and minor dis-

tributaries, interplay with this external forcing. With the study of the lateral consistency and variability, we think we have demonstrated that allogenic and autogenic forcing may eventually indeed be separated to some extent. Some of the spatial and temporal impacts of both allogenic and autogenic controls have also been quantified here. These are the lateral continuity of geometry in paleoflow and perpendicular to paleoflow and the rates of lateral thickness changes and maximum thickness changes of the cycles.

The separation and quantification of allogenic and autogenic variability in the fluvial stratigraphy of the Bighorn Basin display examples from a single case. The specific size of the morphological elements in that fluvial system will determine the spatial scale of autogenic variability in the rock record together with the activity of these elements. The dominance of this autogenic variability in the stratigraphic record will be determined by the aggradation rates. High aggradation rates will cause the imprints of autogenic variability to be spread through the record, while low aggradation rates will cause single levels to be dominated by autogenic variability. As such, cycles will be less visible in those settings. On the other hand, in high accumulation-rate settings, external drivers like cyclic climate forcing may be better displayed in the stratigraphic record. However, to what extent autogenic processes will start to act also at these longer timescales if allogenic triggers remain absent, remains unknown.

3.6 Conclusions

We here studied the interaction of allogenic climate forcing and autogenic processes on building alluvial stratigraphy of the lower Eocene Willwood Formation, Bighorn Basin, Wyoming. The local floodplain stratigraphy is dominated by floodplain aggradation cycles (cycles), recognized in many successions globally, and in this basin thought to be controlled by precession-scale climate change. Analysis of a fully-georeferenced 3-D photogrammetric model covering an area of ca. 10 km² and a succession thickness of ca. 300 m in the McCullough Peaks Area of the Bighorn Basin reveals a total of 44 stacked cycles. These cycles have an arithmetic mean thickness of 6.8 m and a standard deviation of 2.0 m. We find a strong lateral consistency of floodplain aggradational cycle, a solid continuity in stratigraphy in line with all available dating pointing at cyclicity occurring at precession scales, which, together with all previous documentation of the cyclicity and dating, strongly confirms their allogenic, precession-driven nature. At the same time, these cycles display a strong lateral thickness variability that is ascribed to autogenic processes in the fluvial system. Cycle thickness may change as rapidly as 4 m over 400 m when traced laterally. Variogram analysis shows that the thickness of an individual cycle at a specific locality is related to that at another locality over an average distance of 1.3 km in the paleoflow direction and 0.6 km perpendicular to the paleoflow direction. We attributed this to the more continuous morphodynamic features of a fluvial system in the paleoflow direction, thereby indicating the decisive role of fluvial dynamics in shaping geological bodies. The major part of the compensational stacking of stratigraphy occurs after the deposition of 3 cycles, while full compensation seems to be reached after 6 to 7 cycles. The regional traceability of and variability among individual cycles as well as spatial continuity and variability within individual cycles provide an example of the interaction between allogenic and autogenic controls on alluvial stratigraphy and the opportunity to disentangle the impact of these processes in the rock record.

3.7 Acknowledgement

3

4

Fluvial sedimentology of the lower Eocene Willwood Formation

The lower Eocene Willwood Formation of the intermontane Bighorn Basin, Wyoming, USA, is an alluvial red bed succession that has been studied intensively for paleontology, paleoclimate, and sedimentary reconstruction. However, alluvial sandstone bodies and their corresponding river styles remain little characterized and documented. Here, we study the characteristics and river styles of the sandstone bodies through ca. 300 m of alluvial stratigraphy in the McCullough Peaks outcrop area using field data and a georeferenced 3-D photogrammetric model. Four channel facies associations corresponding to different planform river styles are recognized: crevasse channel, massive trunk-shaped channel, braided channel, and sinuous channel, with the latter two styles being the more abundant. Braided and sinuous channel sandstone bodies differ significantly in average thickness (6.1 m vs 9.0 m) but insignificantly in average width (on average 231 m) and paleoflow directions (on average N003). Distinct alternations between braided and sinuous river styles are seen, which show no spatial dependency in the 10 km2 study area. Bighorn Basin margins varied in the early Eocene, with differing tectonic, geological, and topographic characteristics. The observed mix of river styles may be attributed to differential influences of axial and transverse river systems or climate change that controls water discharge and sediment load. An early Eocene geomorphologic reconstruction is implemented summarizing these new and earlier results.

4.1 Introduction

Alluvial architecture illustrates the size, shape, and spatial arrangement of fluvial channel bodies and their associated facies in three dimensions (Allen, 1978; Bridge and Leeder, 1979). The architecture is controlled by both autogenic processes, such as channel avulsion and self-organization (Hajek et al., 2010; Mackey and Bridge, 1995), and allogenic factors, such as eustasy, climate, and tectonics (Bijkerk et al., 2014; Hampson et al., 2013; Holbrook et al., 2006; Shanley and McCabe, 1994). Extensive studies have been conducted on alluvial deposits using various approaches and datasets, including high-resolution three-dimensional seismic data (Posamentier et al., 2007), numerical modeling (Jerolmack and Paola, 2007; Karssenberg and Bridge, 2008; Wang et al., 2021c), and outcrop analogs (Allen et al., 2013; Colombera et al., 2016, 2017; Ghinassi and Ielpi, 2018). Outcrop analogs provide data that span large hierarchical temporal and spatial scales, which can help interpret depositional environments, reconstruct palaeoclimates (Colombera et al., 2016; Howell et al., 2014; Paredes et al., 2016), and be used for subsurface predictive models (Bryant et al., 2000; Enge et al., 2007).

By utilizing alluvial strata in the Bighorn Basin, numerous studies have investigated a variety of aspects: e.g., paleontology (Gingerich and Palasiatica, 2010); palaeo-magnetism (Clyde et al., 1994); and, especially, palaeosols (Abels et al., 2013; Kraus, 2002; Kraus and Gwinn, 1997). In contrast, the alluvial sandstone body character and spatial distribution are less well documented and analyzed. The well-documented floodplain cyclicity in the Willwood Formation of the Bighorn Basin provides an opportunity to investigate the influence of orbital climate forcing on alluvial architecture (Abdul Aziz et al., 2008; Abels et al., 2013). Also, extreme climate warming has been observed to impact alluvial architecture in the basin (Foreman, 2014; van der Meulen et al., 2020). Generic relationships between channel and floodplain deposits were illustrated over basin scales, with thick sheet sandstones ascribed to meandering river processes (Kraus and Gwinn, 1997). Coarse-grained and conglomeritic braided channel deposits were described in the west of the basin (Neasham and Vondra, 1972). Detailed sedimentological description was conducted by Foreman (2014) on the PETM boundary sandstones. Owen et al. (2017, 2019) performed a basin-scale classification of fluvial architecture, with their work and others providing a basin-scale context for our studies.

Here, we characterize channel sandstone bodies in terms of geometry and internal characteristics, reconstruct their related river styles, and fit them in a basin-scale geomorphology. An integrated field analysis is performed on the alluvial sandstone bodies in the McCullough Peaks area of the Bighorn Basin (Figure 4.1), combining field documentation with observations in a georeferenced photogrammetric model developed using an unmanned aerial vehicle (UAV). The objectives of this study are fourfold: (1) to document lithofacies and lithofacies associations, (2) to attribute lithofacies associations to corresponding river styles, (3) to analyze the distributions of the river styles over space, and (4) to reconstruct the early Eocene geomorphology of the Bighorn Basin.
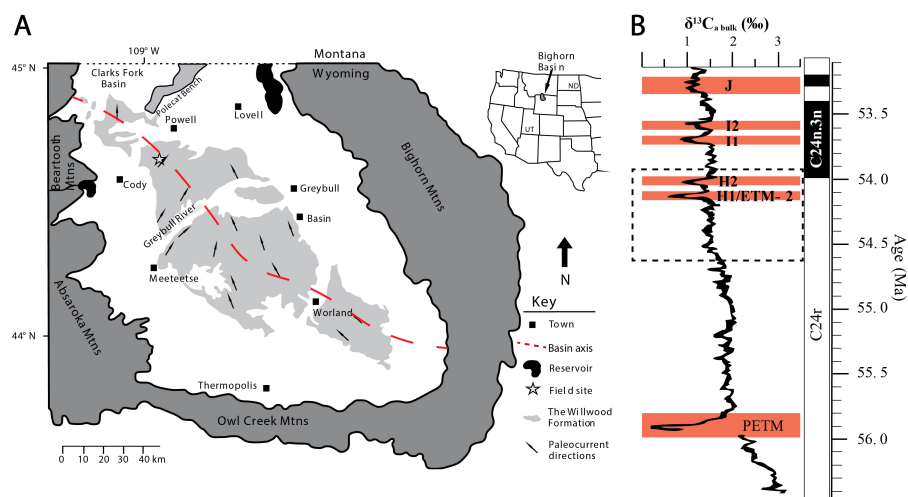
Figure 4.1: (A) The location of the study area, the McCullough Peaks, in the northern Bighorn Basin, Wyoming, USA (after Wang et al. (2017)). Paleoflow data indicated by the arrows are from Neasham and Vondra (1972). Note that the Washakie Range present during the Eocene is now covered by the Absaroka Mountains (Yonkee and Weil, 2015), and the Pryor Mountains present during the Eocene are now not distinguishable from the Bighorn Mountains (Blackstone, 1940). (B) Adjusted $\delta^{13}C_{a\ bulk}$ data from Zachos et al. (2010) by Birgenheier et al. (2019), with orange rectangles indicating hyperthermal events and the dashed rectangle indicating the study interval.

4.2 Geological background

4.2.1 Structural setting

The Bighorn Basin is a Laramide intermontane basin with a length of ca. 200 km and a width of ca. 80 km. It was bounded by the western Beartooth Mountains, southwestern Washakie Range, eastern Bighorn Mountains, and the northeastern Pryor Mountains during Paleocene to Early Eocene (Foose et al., 1961). Drainage of the basin was toward the north and northeast during deposition of the Willwood Formation. The Absaroka Range was formed by volcanic activity during the late early and middle Eocene (Smedes and Prostka, 1972), which makes it challenging to constrain the southwestern margin of the Bighorn Basin in the Eocene. The eastern margin of the basin has always been a relatively gentle slope (Yonkee and Weil, 2015).

4.2.2 Palaeoclimate

The global early Eocene is indicated to be in a hothouse state, with an globally average temperature ~12°C higher than the present global average (Scotese et al., 2021; Westerhold et al., 2020). The early Eocene Bighorn Basin is suggested to have been in a warm-temperate to a subtropical environment with seasonal precipitation. The basin landscape resembled modern-day savannahs, with broad open areas interspersed with forest-bordering streams. There are two hyperthermal events that are recorded in the upper part of our study interval, referred to as H1/ETM2 and H2 (Figure 4.1) (Abels et al., 2016).

4.2.3 Depositional setting

The Willwood Formation consists of a series of lower Eocene alluvial deposits that are currently exposed in the central part of the basin roughly along the NNW-SSE-extending basin axis (Figure 4.1). It is mainly composed of sandstones, siltstones, and claystones, parts of which have undergone intensive pedogenic modification (Kraus and Davies-Vollum, 2004). Extensive studies have been carried out, with main focus on palaeosols (Kraus, 1999, 2002), processes of river avulsion (Kraus and Davies-Vollum, 2004; Kraus and Gwinn, 1997; Neasham and Vondra, 1972), and fluvial cyclicity (Abdul Aziz et al., 2008; Abels et al., 2013). The dominant palaeoflow direction is interpreted to be NNW to NNE (Neasham and Vondra, 1972; Owen et al., 2017, 2019). Cyclic palaeosol maturation patterns associated with heterolithic avulsion deposits have been inferred as the result of allogenic forcing (Abdul Aziz et al., 2008; Abels et al., 2013; Kraus and Aslan, 1993; Wang et al., 2021b). The sediment accumulation rate has been estimated by various studies, showing a range of 288 to 391 m/Myr (Abels et al., 2012, 2013; Clyde et al., 1994; Gingerich and Palasiatica, 2010; Stap et al., 2009; Wang et al., 2021b; Westerhold et al., 2007).

4.2.4 Tectonics and possible provenances

Neasham and Vondra (1972) suggested most Willwood sandstone units to be subarkose, with a mainly western source. In contrast, Kraus and Middleton (1987) indicated that most sandstone bodies in their study area (the Clarks Fork Basin in front of the Beartooth Range) are litharenites, with the main source area in the Beartooth Mountains. Meanwhile, other work indicates the presence of multiple provenances, including all the mountainous areas expressed before or during the early Eocene (e.g. Owen et al. (2019)).

Beartooth Mountains to the northwest

The major uplift of the Beartooth Mountains took place during the mid-to-late Paleocene (Gingerich, 1983). The eastern flank of the Beartooth Mountains was very steep (Wise, 2000). According to the work by DeCelles et al. (1991), the Beartooth fluvial systems are composed of several ephemeral coarse-grained alluvial fans and braid-plain deposits. Lacustrine deposits are reported in the northwest of Powell, in the mountain front close to the Polecat Bench area (Figure 4.1)(Yuretich et al., 1984).

Absaroka Mountains to the west

The Absaroka Mountains forming the western margin of the present-day Bighorn Basin were not emplaced until near the end of Willwood Formation deposition, since volcanic activity started in the middle early to middle Eocene (Smedes and Prostka, 1972; Sundell, 1990). This makes it challenging to understand the original catchment of the Bighorn Basin fluvial system.

Washakie Range to the west

It is suggested that the Washakie Range, present during the Paleocene and Early Eocene, was located farther west of the current western basin boundary, with a steep front towards the east. Overthrusting associated with the formation of the mountain range is likely to have influenced the development of the Willwood sedimentary sequences (Yonkee and Weil, 2015), thus making it difficult to constrain the characteristics of the fluvial system fed by this source terrain. According to Owen et al. (2019), at the time the Willwood system was active, it was characterized as a distributive fluvial system (DFS), with conglomeratic input from the Washakie Range. Kraus (1984) reported early Eocene fanglomerates in the

alluvial fan system sourcing from this range.

Owl Creek Mountains to the south

The uplift around the southern margin of the basin formed the southern Bighorn and Owl Creek Mountains, which were subsequently thrust southward in the early-mid Eocene. In general, the northern slope of Owl Creek Mountains was gentle (not steeply faulted) during the earliest Eocene, and the southern part of the Bighorn Basin was relatively low, probably only forming a gentle rise separating the Bighorn Basin from the Powder River Basin in the south (Wing and Bown, 1985).

Bighorn Mountains to the southeast and east

The Bighorn Mountains have a long shallowly dipping slope on the Bighorn Basin side and a steep thrust scarp on the Powder River Basin side (Yonkee and Weil, 2015). Swampy and lacustrine deposits are indicated to be present in front of the Bighorn Mountains on the Bighorn Basin side (Davies-Vollum and Wing, 1998; Wing and Bown, 1985). There might be large fluvial systems along the western side of the Bighorn Mountains, but they may contribute less and finer sediment to the McCullough Peaks study area given the shallow gradient and consequently less energy there. Westerly palaeocurrents are rarely measured in the eastern and southeastern parts of the basin (Owen et al., 2019), suggesting that the eastern side of the basin might have contributed little to the basinal fluvial system.

Pryor Mountains to the northeast

The Pryor Mountains are interpreted to be asymmetric anticlines that experienced overthrusting in the later stages (Blackstone, 1940). Their contribution as a significant catchment is not supported by the palaeocurrent data. There was a "Pryor Gap" between the Pryor Mountains and the Bighorn Mountains (Blackstone, 1940), which could have served as a possible exit for the fluvial system during the deposition of the Willwood Formation.

4.3 Methodology and dataset

4.3.1 Onsite documentation

Sandstone bodies were systematically documented in the field (Figure 4.2) using a standard set of parameters including grain size, lithology, sedimentary structure, geometry, boundaries, palaeo-flow directions, and dimensions, based on which a lithofacies and lithofacies association classification scheme is established following methods outlined by Miall (1985) and Allen (1983). Data were captured in comprehensive spreadsheets as well as short sedimentary logs to characterize each sandstone body type. The grain size was measured by observing the grains on the grain size chart under a hand lens. Dimensions of sandstone bodies are measured using Jacob's staff, flexible tapes, and binoculars when not accessible.Palaeocurrent data and cross-set thickness were measured from dune-scale cross-stratification (mainly planar and trough cross-stratification).

4.3.2 UAV-based photogrammetry

The preparation of the UAV-based photogrammetric model has been detailed in Wang et al. (2021b). The model includes 21144 photos taken on 34 flights and it covers a total area of 10 km², with approximate north-south and east-west lengths of ca. 2.5 km and

4
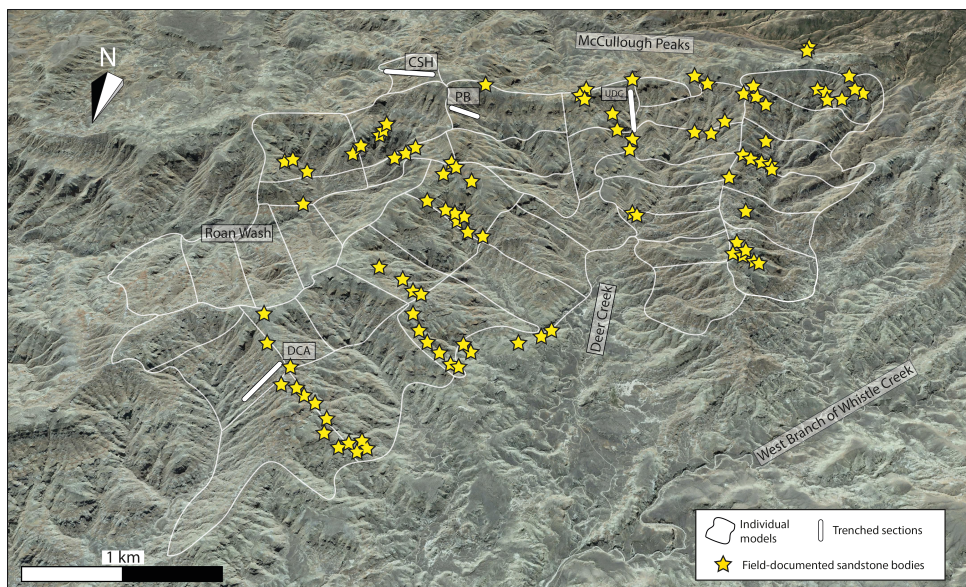
Figure 4.2: Bird's eye view from Google Earth showing UAV photogrammetry coverage and outcrop-documented sandstones. Abbreviations: DCA, Deer Creek Amphitheater section (Abels et al., 2013); PB, Purple Butte section (Wang et al., 2018); UDC, Upper Deer Creek section (Wang et al., 2018); CSH, Creek Star Hill section; and RW, Roan Wash section.

ca. 4 km, respectively. The studied stratigraphic succession is ca. 300 m thick and dips at ca. 2° towards the south. Fifty-seven ground control points (GCPs) were placed, contributing to centimeter accuracy relative to the local base station. Agisoft PhotoScan (Version 1.4.3, July 2018; current Metashape) was used to build the 3-D digital models, which were later imported into LIME (version 2.2.2) for visualization and interpretation (Buckley et al., 2019).

4.3.3 Petrological analysis

A total of 32 sandstone specimens were sampled from outcrops in the study area and made into thin sections in the laboratory. Composition of framework grains was obtained from 300 point counts per thin section. Classification of sandstones follows the scheme by Mcbride (1963) that groups framework grains into (1) quartz plus chert and quartzite, (2) feldspar, and (3) rock fragments and accessory minerals.

4.3.4 Formative bankfull depth estimation

Dune-scale cross-set thickness (S_m) has been empirically used to estimate the mean formative bedform height (h_m), as is shown in Equation 4.1 (Bridge and Tye, 2000; Leclair and Bridge, 2001). The application of this method requires to meet the precondition that the coefficient of variation (ratio of standard deviation to mean) of the preserved cross-set thickness should vary between 0.58 and 1.18 (Bridge and Tye, 2000).

$$h_m = 2.9 \ (\pm 0.7) \ sm \tag{4.1}$$

Then, the mean formative bankfull depth (d) can be estimated based on the empirical equation proposed by Bradley and Venditti (2017):

$$d = 6.7 \ h_m \ (\text{with 50\% prediction interval: } 4.4 \ h_m \text{ to } 10.1 \ h_m) \tag{4.2}$$

4.3.5 Statistical analysis

Two-sample t-tests are performed to assess whether the differences between parameters of different types of deposits are statistically significant. Paleocurrent data are analyzed as circular data using the *R* programming language, and the Rayleigh Test of Uniformity is implemented to check whether the distribution is significantly different from the uniform distribution. Watson's Two-Sample Test of Homogeneity is employed to compare whether the two distributions are significantly different from each other.

4.4 Results

4.4.1 Lithofacies analysis

Based on detailed observation and description of grain size, lithology, internal sedimentary structures, and positions in the sandstone bodies, a total of 12 lithofacies are recognized in the field (Figure 4.3 and Table 4.1). There is one conglomeratic lithofacies, named clast-supported conglomerate (G); there are nine sandy lithofacies, including massive sandstone (Sm), trough cross-stratified sandstone (St), planar/tabular cross-stratified sandstone (Sp), ripple cross-laminated sandstone (Sr), climbing-ripple cross-laminated sandstone (Scr), low-angle (<15°) cross-stratified sandstone (Sl), sandstone with erosional scour and fill (Se), bioturbated sandstone (Sb), and convoluted sandstone (Sc); there are two silty to muddy lithofacies: siltstones and claystones (Fs) and ripple-laminated siltstones (Fl). Details of their character and interpretation are given in Table 4.1.

4
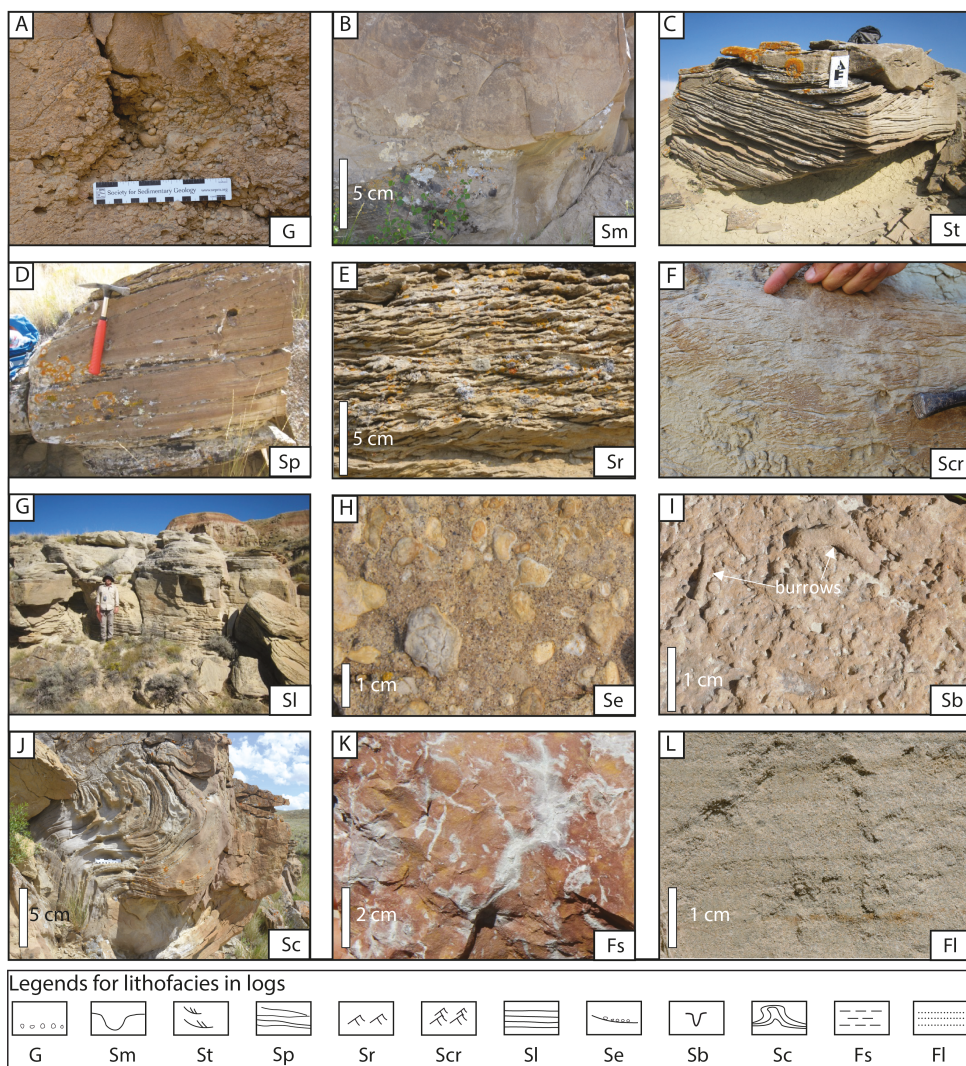
Figure 4.3: Lithofacies recognized in the study area. Lithofacies recognized in the study area. A. Clast-supported conglomerate (lithofacies G); scale bar length = 15 cm. B. Massive sandstone (lithofacies Sm). C. Trough cross-stratified sandstone (St); card length = 10 cm. D. Planar/Tabular cross-stratified sandstone (lithofacies Sp); hammer length = 25 cm. E. Ripple cross-laminated sandstone (lithofacies Sr). F. Climbing-ripple cross-laminated sandstone (lithofacies Scr). G. Low-angle (<15°) cross-bedded sandstone (lithofacies Sl); person height = 180 cm. H. Sandstone with erosional scour and fill (lithofacies Se), with floating carbonate nodules as the lag deposits. I. Bioturbated sandstone (lithofacies Sb). J. Convoluted sandstone (lithofacies Sc). K. Siltstones and claystones (lithofacies Fs). L. Ripple-laminated siltstones (lithofacies Fl). Legends for lithofacies are shown for logs in below figures.

Table 4.1: Description and interpretation of lithofacies.

Lithofacies code	Description	Interpretation
Clast-supported conglomerate (**G**)	Poorly sorted, granule to small pebble conglomerate, with medium-grained angular sandstones as matrix. Conglomerate fills erosional scours can also be organized in 20 to 60 cm thick beds at the base of sandstone bodies.	Intrabasinal clasts of floodplain mudstones or granules deposited by subcritical to supercritical traction flow.
Massive sandstone (**Sm**)	Fine to medium-grained sandstone, well-sorted, no apparent sedimentary structures, a few decimeters in thickness.	High rate of deposition, probably formed during high-discharge periods.
Trough cross-stratified sandstone (**St**)	Fine- to coarse-grained, well-rounded sandstone forming up to 50 cm thick cross-stratified beds. Preserved set thickness varying between 5 and 30 cm, decreasing upward in the bed in many cases. Sets in the basal part of a sandstone body are in many cases poorly sorted and may contain granules; sets in the top are better sorted. Claystone chips are common. Bed boundaries are slightly inclined (up to 2°).	Subcritical flow, normal deposition rates, bedload deposition, dune migration.
Planar/Tabular cross-stratified sandstone (**Sp**)	Fine- to medium-grained, well-rounded, and moderate- to well-sorted lithic sandstone forming up to 30 cm thick cross-stratified beds. Preserved set thickness varying between 5 and 20 cm, in many cases decreasing upward. Bed boundaries are slightly inclined.	Subcritical flow, normal deposition rates, bedload deposition, plane bed formation.
Ripple cross-laminated sandstone (**Sr**)	Very fine to fine-grained sandstone, well-sorted, ripple lamination with a set thickness of 2-5 cm.	Ripple migration under the low-flow regime.
Climbing-ripple cross-laminated sandstone (**Scr**)	Fine-grained sandstone, moderately to well sorted, asymmetrical cross lamination with climbing set boundaries, with a bed set thickness of 2-5 cm.	Subcritical flow, faster deposition than ripple migration due to abundant suspended sediments.
Low-angle (<15°) cross-bedded sandstone (**Sl**)	Fine to medium-grained sandstones, well-rounded, moderately to well-sorted, bed thickness of 0.1-1 m. Low-angle stratification with a long wavelength and low angle.	Deposition under upper-flow-regime conditions during high-stage flooding events in nearby channels.
Sandstone with erosional scour and fill (**Se**)	Fine to medium-grained poorly sorted sandstones, with sand-supported nodules (0.5-2 cm in diameter) filling the scours, thickness of 0.2-1 m.	Supercritical flow causing the scour, high deposition rates, with nodules as lag deposits
Bioturbated sandstone (**Sb**)	Fine- to medium-grained sandstone, moderately to poorly sorted, with vertical and horizontal burrows.	Trace fossils formed by insets, dwelling, resting, crawling
Convoluted sandstone (**Sc**)	Fine- to medium-grained, well-rounded, moderately to well-sorted lithic sandstone. Preserved set thickness varying between 5 and 20 cm, in many cases decreasing upward. Overturned-fold-shaped structures that modified or destroyed primary sedimentary structures, with a size of 20-60 cm.	Water escape structures formed in rapidly deposited, poorly sorted sands
Siltstones and claystones (**Fs**)	Clay to siltstone, with laminated or blocky structures, various matrix colours, frequently seen slickensides and nodules.	Soil formation with chemical precipitation developed on former overbank fines.
Ripple-laminated siltstones (**Fl**)	Well sorted siltstones with ripple laminations.	Settling from suspension and forming silty plug in the abandoned channel.

Table 4.2: Presence of facies in each facies association

Facies associations	Containing facies
FA1 (crevasse channel sandstone deposits)	St, Sp, Sr
FA2 (large-scale massive trunk-shaped channel sandstone deposits)	G, St, Sp, Sr, Sc
FA3 (braided channel sandstone deposits)	G, Se, St, Sp, Sr, Sc, Sl
FA4 (sinuous channel sandstone deposits)	G, Se, St, Sp, Sr, Sc, Fl
FA5 (crevasse splay deposits)	St, Sl, Sr, Sb
FA6 (overbank palaeosol deposits)	Fs

4.4.2 Facies association analysis

According to the organizations of lithofacies in the vertical succession and lateral distribution (Table 4.2), a total of 6 facies associations are classified, which fall into two major categories, namely channel facies associations and floodplain facies associations. They are described and interpreted in the following sections, though petrological and statistical analyses are not done in all facies associations.

4.4.3 Channel facies associations

Facies Association 1: crevasse channel deposits

Description:

Facies Association 1 (FA1) is mainly composed of fine- to medium-grained sandstone bodies, with a thickness range of 0.5-3 m. Its indurated part shows a lenticular external geometry with concave-up margins in the transverse view (Figure 4.4A) and ribbon-shaped geometry in the longitudinal view (Figure 4.4B). Various lithofacies are present, including trough cross-stratified sandstone (St), planar/tabular cross-stratified sandstone (Sp), and ripple cross-laminated sandstone (Sr). Within FA1, trough cross-stratified sandstone (St), if present, is usually in the lower part, planar/tabular cross-stratified sandstone (Sp) in the middle part, and ripple cross-laminated sandstone (Sr) in the upper part. This facies association is generally encased within floodplain deposits that present pedogenic features due to subaerial exposure. The contact between FA1 and floodplain fines is usually sharp with floodplain fines passively draping the top of the sandstone body.

Interpretation:

FA1 is interpreted to be the product of relatively straight crevasse channels (Clyde and Christensen, 2003; Gibling, 2006; Kraus and Gwinn, 1997), also known as feeder channels of the avulsion complex (Davies-Vollum and Kraus, 2001). The sharp contact with floodplain fines indicates an erosional base, and the presence of cross-bedding suggests downstream traction of stream power. Similarly, in a region in the vicinity of the study area, this type of sandstone bodies is reported to be generally thinner than 3 m (Clyde and Christensen, 2003; Kraus and Gwinn, 1997) and referred to as ribbon sandstone bodies (Kraus and Middleton, 1987).
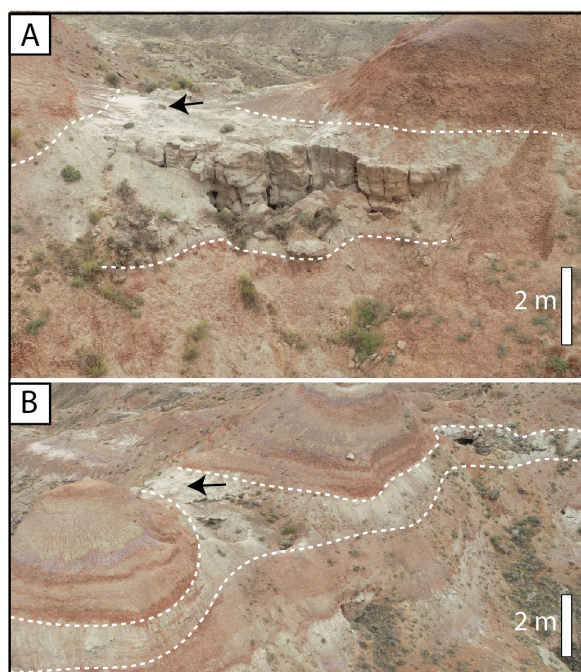
Figure 4.4: Facies Association 1: crevasse channel sandstone deposit. (A) UAV photo showing the channel body in transverse view. (B) UAV photo showing the ribbon shape of the same channel body in longitudinal view. The two black arrows in panels A and B point at the same gravel rock.

Facies Association 2: large-scale massive trunk-shaped channel deposits

Description:

Facies Association 2 (FA2) is mainly composed of fine- to medium-grained sandstones (Figure 4.5), with a thickness of commonly >8 m. FA2 deposits generally present channelized features with clear gradually-thinning channel wings (Figure 4.5A) or steep channel margins (Figure 4.5D). There is usually a channel lag at the base formed by clast-supported conglomerate (G) and trough cross-stratified sandstone (St), above which trough cross-stratified sandstone (St), planar/tabular cross-stratified sandstone (Sp), and ripple cross-laminated sandstone (Sr) dominate, with occasionally seen convoluted sandstone (Sc). FA2 generally appears to be massive, with a paucity of internal erosional surfaces and an abundance of sharp channel margins (Figure 4.5D). FA2 is relatively rare with 5 localities out of 108 documented sandstone bodies in the study area, and it in many cases (3 out of 5) occurs at the same stratigraphic level as the sinuous channel sandstone deposits (FA4), which will be introduced later.

Interpretation:

FA2 may represent the main channel in the axial fluvial system (DeCelles and Cavazza, 1999) to which other streams join. Great sandstone body thickness (>8 m) and steep channel margin (e.g. Figure 4.5D) may indicate deep and strong floodplain scouring by such

4
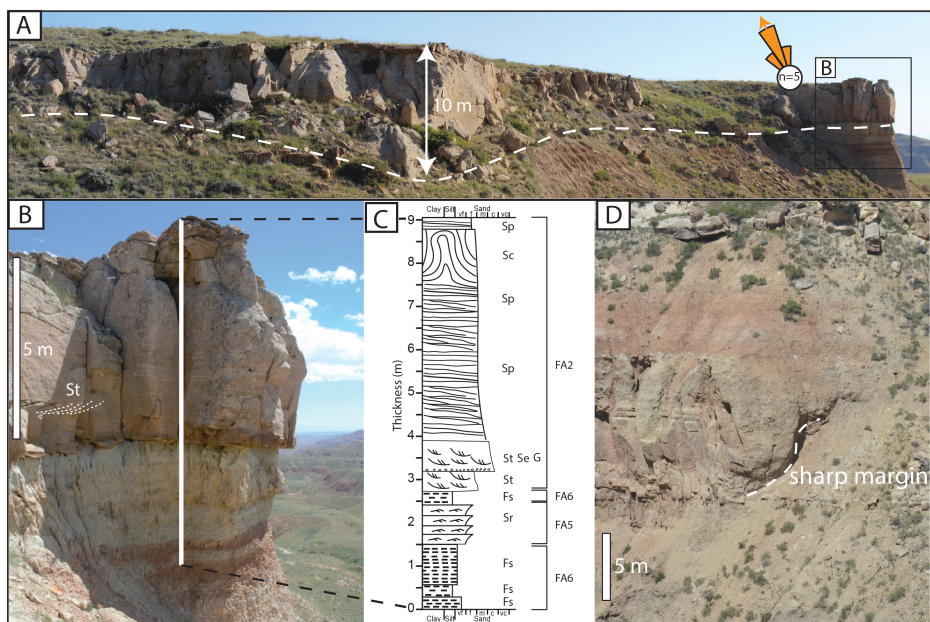
Figure 4.5: Facies Association 2: large-scale massive trunk-shaped channel sandstone deposit. (A) Overview of the massive trunk-shaped channel deposits with a maximum thickness of 10 m. (B–C) Zoomed-in view of the right side of panel A showing detailed sedimentary structures and underlying floodplain fines. The white line marks the corresponding sedimentological log. (D) Second example of FA2 deposits showing massive features that are not accessible due to the steep terrain. The contact between the sandstone body and floodplain is sharp here. For legend, see Figure 4.3.

axial fluvial system. The erosional base of the sandstone body as well as the presence of clast-supported conglomerate (G) as channel lag deposits are consistent with the strong scouring behavior of the fluvial system.

Facies Association 3: braided channel sandstone deposits
Description:
Facies Association 3 (FA3) is generally composed of medium-grained sandstones, with conglomerate occasionally seen at the base as lag deposits (Figure 4.6). It is usually multi-storied, with the thickness varying between 4 m and 8 m, and a single-story unit within it is generally 0.5-2 m thick. Sharp erosional bases are present between stories. Within a single story, there is usually sandstone with erosional scour and fill (Se) and trough cross-stratified sandstone (St) in the lower part, planar/tabular cross-stratified sandstone (Sp) in the middle part, as well as ripple cross-laminated sandstone (Sr) and low-angle (<15°) cross-stratified sandstone (Sl) in the upper part, with occasionally seen massive sandstone (Sm; Figure 4.6D and Figure 4.6E). The dip direction of the accretion surfaces is generally parallel to measured palaeocurrent directions in cross-bedded sets.
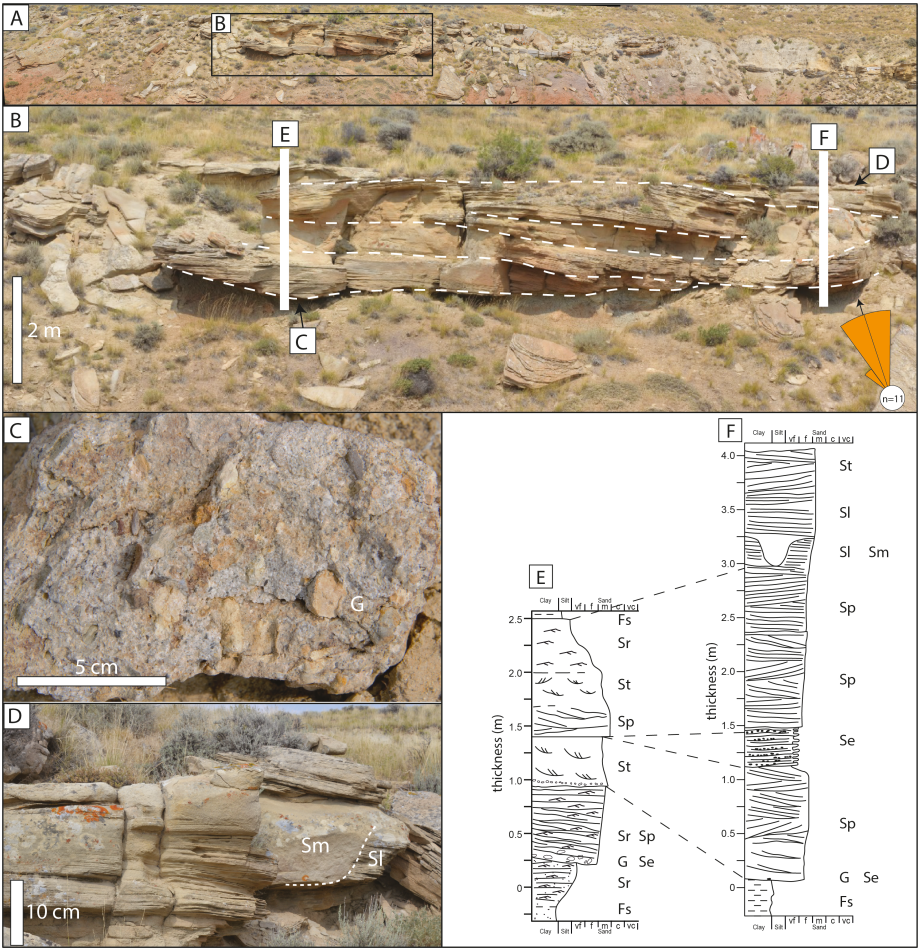
Figure 4.6: Facies Association 3: braided channel sandstone deposits. (A–B) Overview and close-up view of FA3 deposits, where there are five stories with the thickness of each varying between 0.5 and 1 m. (C) The bottom view of the channel base with floodplain nodules as lag deposits. (D) Massive bank-breaching deposits (Sm; cf. van den Berg et al. (2017)) eroding low-angle cross-bedded sandstone (Sl). (E–F) Sedimentary logs for locations in panel B, showing the vertical succession of lithofacies in FA3. For legend, see Figure 4.3.

4
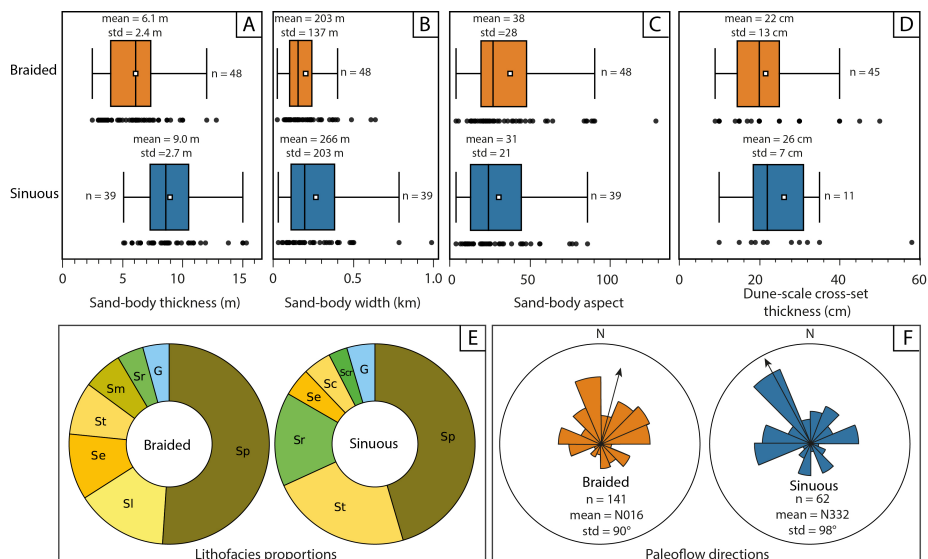
Figure 4.7: (A) Thicknesses, (B) widths, and (C) aspects of braided and sinuous channel sandstone bodies. (D) Thicknesses of dune-scale cross-sets. (E) Proportions of lithofacies types in the total thickness (T) of the field-documented braided and sinuous sandstone bodies (abbreviations are listed in Table 4.1). (F) Rose diagrams of palaeoflow directions. Note the significantly thinner and insignificantly narrower braided deposits than sinuous counterparts, the similarity and difference between lithofacies proportions, and the similarity and difference between paleoflow directions.
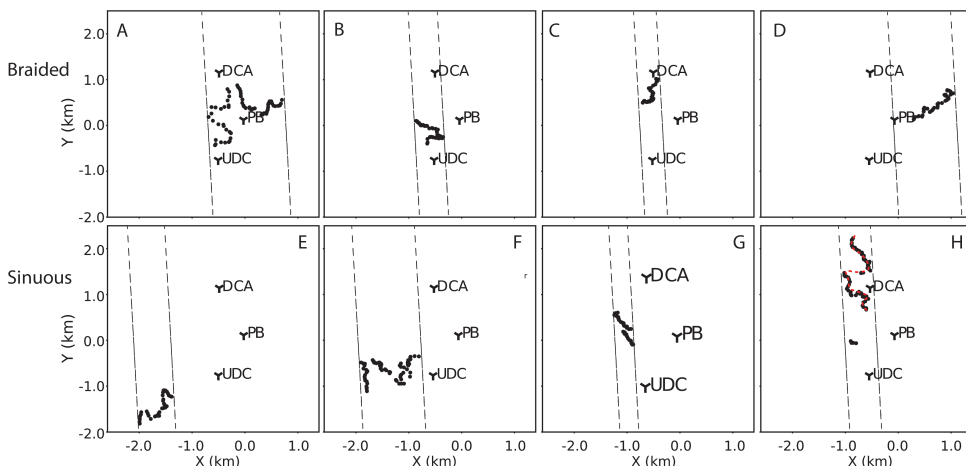
Figure 4.8: (A-D) Four examples showing how widths of braided channel sandstone bodies are measured. (E-H) Four examples showing how widths of sinuous channel sandstone bodies are measured. The black dots indicate the presence of the sandstone body at the outcrop surface, and two dashed boundary lines are along the average paleoflow direction (N004). A sinuosity index is calculated in subfigure H, indicated by the red dot line. Locations of DCA, PB, and UDC sections can be found in Figure 4.2 for comparison.

Forty-eight sandbodies with FA3 are documented in this study. The average thickness of these sandstone bodies is 6.1 m while the standard deviation is 2.4 m (Figure 4.7A). Their apparanant widths from field documentation were corrected using the average paleoflow direction (Figure 4.8); the corrected widths have an average of 203 m and a standard deviation of 137 m (Figure 4.7B). These braided channel sandstone bodies commonly have 3-4 stories, with an average story thickness of 1.7 m. Dune-scale cross-sets in FA3 (n =45) have an average thickness of 22 cm with a standard deviation of 13 cm and a coefficient of variation (CV) of 0.59 (Figure 4.7C). Using these dune-set data and employing existing empirical relationships (Bridge and Tye, 2000; Leclair and Bridge, 2001), the average bankfull depth is estimated to be 4.3 m (22 cm × 2.9 × 6.7). The high CV (0.59) ensures the reliability of our estimation of the formative flow depth using cross-set thickness. In terms of lithofacies proportion, planar/tabular cross-stratified sandstone (Sp) and low-angle (<15°) cross-stratified sandstone (Sl) are dominant lithofacies in FA3 when it comes to their proportions in thickness, accounting for 51% and 15%, respectively (Figure 4.7D). Palaeoflow rose diagram shows a mean flow direction of N016 and a standard deviation of 90° (Figure 4.7E). The distribution of the paleoflow data is significantly different from the uniform distribution according to the Rayleigh test of uniformity (0.286 with a p-value of 0).

Microscopic observation of 28 thin sections shows that monocrystalline quartzs in FA3 are generally subrounded to subangular and slightly spherical (Figure 4.9A and Figure 4.9B), and they are classified together with polycrystalline quartz (quartzite), and microcrystalline quartz (chert) as "quartz" in the scheme developed by Mcbride (1963). Feldspar content widely varies, with potash feldspar (e.g. orthoclase and microcline) more dominant than plagioclase (e.g. albite). Rock fragments include sedimentary, volcanic, and metamorphic components. Accessory (heavy) minerals are either of igneous or metamorphic origin, and include magnetite, zircon, tourmaline, and hornblende. Both calcite and silica cement are observed, with the former one contributing to the mosaic granular framework, while the latter caused euhedral to subhedral quartz/feldspar overgrowths.

Interpretation:

FA3 represents the sedimentary product of braided channels. This interpretation is supported by the predominance of medium to coarse-grained bedload material (Foreman, 2014), the scarcity of lateral accretion deposits, the abundance of downstream accretion deposits, and stacking of several single-story units within individual sandstone bodies (Gibling, 2006). The presence of some fine-grained deposits below erosional surfaces suggests channel abandonment and reoccupation. Single-story units in FA3 are generally narrow and thin, indicating their short life-spans and quick lateral coalescence of multiple channel stories (Gibling, 2006). In general, braided channels are believed to result from high sediment load, coarse sediment grain size, high gradient, and weak overbank materials (Church, 2006; Schumm, 1985).

Facies Association 4: sinuous channel sandstone deposits
Description:

Facies Association 4 (FA4) is generally composed of (1) poorly sorted, subangular, coarse-grained trough cross-stratified sandstones (St) with granules (G) and sandstones with erosional scour and fill (Se) at the base, (2) large-scale inclined strata with moderate to well-sorted medium-grained trough cross-stratified sandstones (St) and planar cross-stratified

4
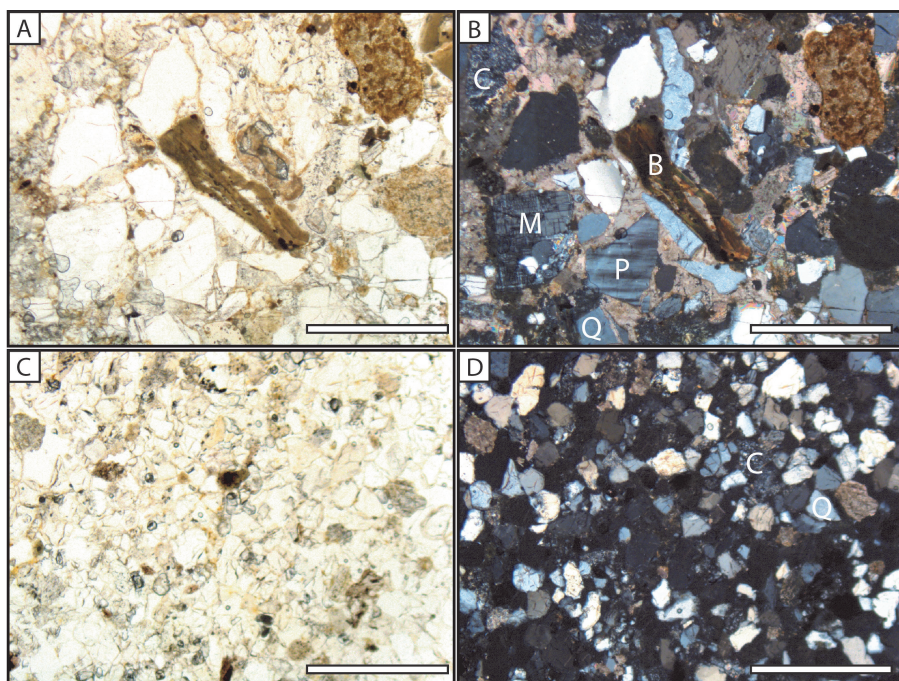
Figure 4.9: Petrographic characteristics of braided and sinuous deposits. (A, B) Thin sections of braided channel deposits under plane- and orthogonally-polarized light. (C, D) Thin sections of sinuous channel deposits under plane- and orthogonally-polarized light. B = biotite; C = chert; M = microline; P = plagioclase; Q = quartz. White bar for scale is 500 μm.

sandstones (Sp) in the middle, and (3) fine-grained ripple-laminated sandstones (Sr) at the top (Figure 4.10). The basal part is usually 0.5-1 m thick, while the middle and upper parts are generally thicker than 4 m. Both dune-scale cross-stratification (Figure 4.10D) and ripple-scale cross-lamination sedimentary structures are present. Accretion beds (Figure 4.10B) are inclined approximately perpendicular to or at a large angle with measured palaeocurrent directions. Water-escape structures (Sc) are occasionally seen within lateral accreted deposits (Figure 4.10C). The presence of one well-preserved extensive channel belt oriented in the downstream direction makes it possible to calculate its channel sinuosity index in the photogrammetric model (Figure 4.8H), which is 1.8 and thus falls in the meandering river category (Williams, 1986).

Thirty-nine sandstone bodies with FA3 are documented from our field investigation. The average thickness is 9.0 m while the standard deviation is 2.7 m (Figure 4.7A). Apparent field measurements of these sandbodies are corrected against the average paleoflow direction (Figure 4.8); corrected, near-true widths of these sandbodies have an average value of 266 m and a standard deviation of 203 m (Figure 4.7B). Dune-scale cross-sets in FA4 (n =11) have an average thickness of 26 cm with a standard deviation of 7 cm and thus a coefficient of variation (CV) of 0.29 (Figure 4.7C). From these data and application of existing empirical relationships (Bridge and Tye, 2000; Leclair and Bridge, 2001), the average

bankfull depth is calculated to be 5.1 m (26 cm × 2.9 × 6.7), which is consistent with the thickness of the inclined strata (commonly > 4 m). The low CV (0.29, required to range between 0.58-1.18) renders it uncertain to estimate the formative flow depth using cross-set thickness. Planar/tabular cross-stratified sandstone (Sp) and trough cross-stratified sandstone (St) are predominant lithofacies when it comes to their proportions in thickness, accounting for 45% and 23%, respectively (Figure 4.7D). The palaeoflow measurements (n = 63) present a mean flow direction of N332, with a standard deviation of 98° (Figure 4.7D). The distribution of the paleoflow data in FA4 is significantly different from the uniform distribution according to the Rayleigh test of uniformity (0.23 with a p-value of 0.04).

Compared with FA3 braided channel sandstone bodies, sinuous counterparts are significantly thicker (t = 5.3, p = 0.9×10^{-7}) but not significantly wider (t = 1.4, p = 0.16) according to the t-test. However, dune-scale cross-sets in FA4 sinuous channel deposits are not significantly different from those in FA3 braided channel deposits (t = 0.6, p = 0.5), although the average of the former is thicker than that of the latter. In terms of paleoflow measurements, there is no significant difference between braided and sinuous channel deposits at 0.05 level of significance according to Watson's Two-Sample Test of Homogeneity, which is likely attributable to the large standard deviations of both measurements (90° and 98°, respectively).

There are 3 available thin sections for FA4 sandstone. Compared with FA3, FA4 is overall finer and has higher abundances of quartz and chert (Figure 4.9C and Figure 4.9D).

Interpretation:
FA4 is interpreted to represent the sedimentary product of sinuous channels with perennial water discharge (Kraus, 2002). Because accretion beds are aligned broadly perpendicular to the overall paleoflow direction, they are inferred as lateral accretion beds (Figure 4.10B). These lateral accreted deposits result from the reduced shear stress associated with helicoidal flows, which leads to erosion in the outer bend and lateral migration of the point bar located in the inner bend in the same direction (Bridge, 1993). The coarser-grained lower segment of the sandstone bodies represents the channel lag interval. In general, sinuous channels are believed to result from perennial flow, a relatively low sediment load, a low gradient, and cohesive overbank materials (Church, 2006; Schumm, 1985).

4.4.4 Floodplain facies associations

The floodplain deposits have been described in numerous studies (Abdul Aziz et al., 2003, 2008; Abels et al., 2013; Kraus and Hasiotis, 2006; Kraus and Middleton, 1987; Kraus and Aslan, 1993; Kraus and Davies-Vollum, 2004; Kraus and Gwinn, 1997), and thus only a comprehensive summary is provided here.

Facies Association 5: crevasse splay deposits
Description:
Facies Association 5 (FA5) consists of very fine- to coarse-grained sandstones (Figure 4.11A). It is in many cases composed of multiple beds, with the thickness of an individual bed ranging from 0.1 m to 0.5 m. FA5 sediments are in general well sorted. Trough cross-stratified sandstone (St), low-angle (<15°) cross-stratified sandstone (Sl), and ripple cross-laminated sandstone (Sr) are the most dominant lithofacies, typically presenting upward coarsening

trends. The lateral extent of FA5 can be up to a few kilometers as measured from the photogrammetric model and traced in the field. Burrows are observed oriented in random directions (Sb in Table 4.1). The palaeocurrents measured in FA5 deposits are generally oblique to the main channel from which the deposit originates. FA5 deposits are prevalent in the whole stratigraphy, forming the so-called heteolithic deposits of Abels et al. (2013).

Interpretation:
FA5 is interpreted to represent unconfined flow conditions on the floodplain, as part of a splay complex formed during erosion of the channel levee (Davies-Vollum and Kraus, 2001; Fischer et al., 2007). Multiple beds may represent multiple events of crevasse processes. FA5 has been commonly referred to as heterolithic deposits as the product of avulsion processes (Kraus, 1999; Kraus and Aslan, 1993).

4

Facies Association 6: overbank palaeosol deposits

Description:
Facies Association 6 (FA6) is the most dominant facies association in the study area (Figure 4.11B and Figure 4.11C), and it is mainly composed of claystones, siltstones, and sandy siltstones, with coarser materials (sandy siltstones) in the lower parts and finer materials (siltstones and claystones) in the upper part (Abels et al., 2013). Various matrix colors including light grey, black, (dark) reddish-brown, purple, olive, and bright yellowish-brown. The color of the same palaeosol layer is found to be stronger in the place where sandstone bodies underlie. There are broadly two types of FA6 deposits in terms of pedogenic strength, namely moderately pedogenically modified ones and strongly pedogenically modified ones, the latter of which is featured by abundant mottling and nodules. Similarly, Abels et al. (2013) propose to divide FA6 deposits into three main types according to the colors, including purple, purple-red, and red types, which differ in various aspects, such as the commonly observed carbonate nodules in purple-red and red FA6 deposits and contrastingly absent carbonate nodules in purple FA6 deposits. More details including cyclic features of palaeosols in the study area have been provided and comprehensively analyzed by Abels et al. (2013) and Wang et al. (2021b).

Interpretation:
FA6 is interpreted to result from overbank deposition (Abels et al., 2013; Bown and Kraus, 1987). The extensive presence of intersecting slickensides suggests that FA6 is mainly the result of vertic palaeosol formation (Abels et al., 2013). Different drainage conditions are inferred according to the carbonate content and colors of various palaeosols (Kraus and Hasiotis, 2006). For instance, stronger colors of palaeosols above sandstone bodies are attributed to better drainage conditions since the sandstone bodies commonly constitute the geomorphological highlands in the local. In general, a lower sedimentation rate and a longer hiatus contribute to a more developed soil profile, which is attributed to the more stable channel belt location (Kraus, 1999).
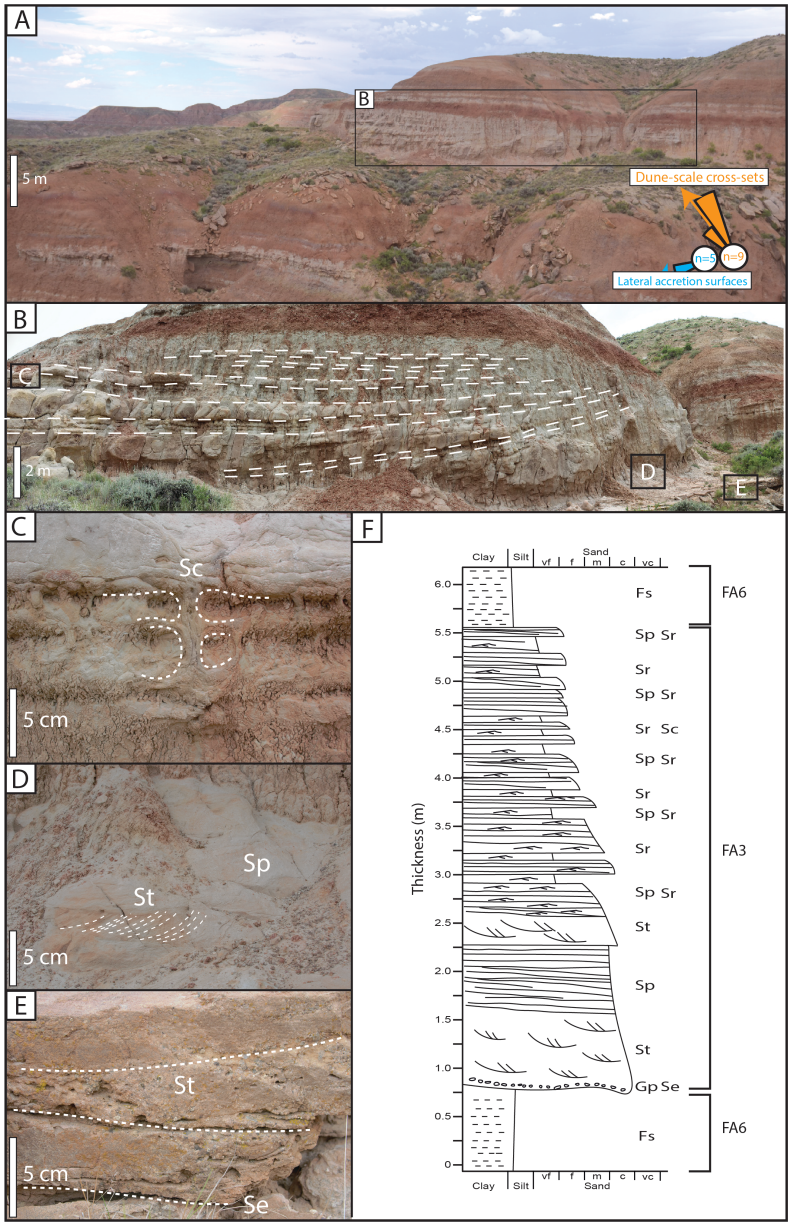
Figure 4.10: Facies Association 4: sinuous channel sandstone deposits. (A) Overview photo showing the juxtaposition between FA4 and surrounding strata. (B) Enlarged view of the FA4 deposits, where lateral accretion deposits are distinct. (C) Convolute sandstone with clear water escape structures. (D) Trough cross-bedding with a dominant flow direction of 10°. (E) Channel-floor clast deposits at the base of FA4. (F) Composite sedimentary log illustrating the vertical succession of lithofacies in FA4. For legend, see Figure 4.3.

4
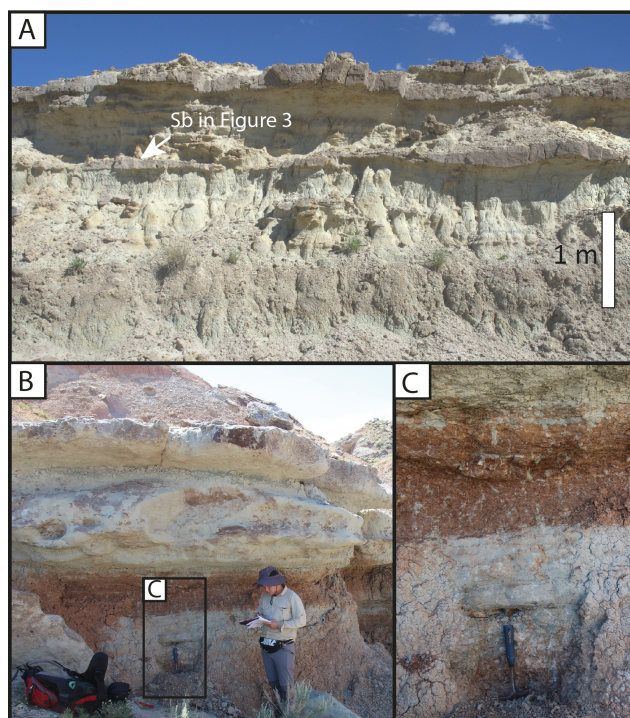
Figure 4.11: Facies Associations 5 and 6. (A) Heterolithic, weakly pedogenic deposit interpreted as crevasse splay deposit. (B-C) Strongly pedogenically-modified deposit interpreted as overbank deposit. The person for scale is ~1.8 m, and the hammer for scale is ~25 cm long.

4.4.5 Distribution of sandstone bodies

We assign the highest point of a channel sandstone body in the 3-D photogrammetric model as the representative point. Thus, we can project the locations of all the channelized sandstone bodies in the 3-D space (Figure 4.12A). Crevasse channels (FA1) are not projected because they are less geologically important, nor are massive trunk-shaped channels (FA2) because they are proportionately insignificant. It can be seen in the XY plane of Figure 4.12A that FA3 braided and FA4 sinuous channel sandstone bodies occur in a mixed manner. In other words, laterally (along XY horizontal plane), FA3 braided or FA4 sinuous systems do not confine to certain portions of the study area, and they are rather mixed. Projection of the channel sandstone bodies onto the YZ plane shows the pseudo-downstream-direction stratigraphic profile since the average paleoflow direction is 004N. With references to several floodplain cycle boundaries, we calibrate the distribution of sandstone bodies in the YZ plane (Figure 4.12A). We show an example of sinuous-dominated stratigraphic interval as well as an example of braided-dominated stratigraphic interval (Figure 4.12A). Projection of the channel sandstone bodies onto the XZ plane doesn't help, because of the mixed influence of paleoflow direction and tectonic tilting. This "automatic" projection brings about uncertain results with respect to the stratigraphic relationship between channel sandstone bodies and corresponding floodplain aggradation cycles. We will present this stratigraphic relationship by manually locating each sandstone body in the corresponding precession-scale floodplain aggradation cycle in Chapter 5.
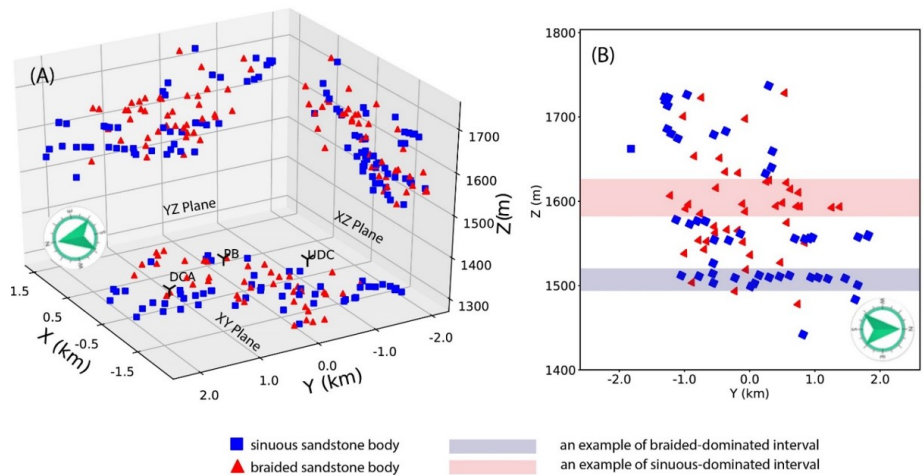
Figure 4.12: (A) Projection of sandstone bodies in 3-D space. (B) Projection of sandstone bodies from 3-D space to 2-D XY horizontal plane. The blue-shaded interval in panel B is calibrated to be horizontal according to field observations although it is inclined in panel A due to topographic variation and tectonic tilting. X and Y coordinates are converted from global UTM coordinates (zone 12N) to local ones, with an applied offset of (673000 m, 49242600 m). Locations of DCA, PB, and UDC sections can be compared with those in Figure 4.2.

4.5 Discussion

Our integrated field analysis allows us to discuss differences in flow conditions associated with major facies association sandstone bodies (FA3 braided, n = 48; FA4 sinuous, n = 39) and explore controls on geomorphic zonation and mixing river styles in the study area.

4.5.1 Bighorn Basin river styles and flow conditions

FA3 braided channel sandstone deposits and FA4 sinuous channel sandstone deposits present both similarities and differences. First of all, the most dominant lithofacies in both of them is the planar cross-stratified sandstone (Sp; Figure 4.7E), which is the result of straight crested bedforms in the subcritical flow regime with intermittent to continuous sand motion (Bourquin et al., 2009; Coleman, 1969; Went and McMahon, 2018). The second most dominant lithofacies in FA3 braided channel sandstone deposits is low-angle (<15°) cross-bedded sandstone (Sl), which is formed in upper flow regimes, accompanied by high sediment concentration and continuous sand motion (Bourquin et al., 2009; Coleman, 1969; Went and McMahon, 2018). In contrast, the second most dominant lithofacies in FA4 sinuous channel sandstone deposits is trough cross-stratified sandstone (St), which is the result of linguoid bedforms that mainly develop in the subcritical lower flow regimes. Based on the two most dominant lithofacies in FA3 and FA4, the flow velocity that produces FA3 braided channel sandstone deposits is in general higher than that produces FA4 sinuous channel sandstone deposits. From the perspective of Froude number (Kennedy, 1969), FA3 braided channel sandstone deposits should be formed in a condition of either higher velocity or shallower water depth or a combination of both than FA4 counterparts.

The narrow and thin single-story units in FA3 indicate short life-spans and quick lateral coalescence of multiple channel stories that may result from multiple phases of ephemeral flow (Gibling, 2006) or spike-like discharge conditions (Fielding et al., 2018). In contrast, the presence of lateral accretional surfaces and the sinuosity index up to 1.8 in FA4 suggest more stable, perennial water flow conditions. More importantly, FA3 braided channel deposits are significantly thinner and insignificantly narrower than FA4 sinuous channel deposits, which indicates FA3 may be formed in flashy-discharge conditions instead of continuously high-discharge conditions (Fielding et al., 2018).

The insignificant difference in paleoflow directions between FA3 and FA4 suggests that they may have developed in channel belts with similar downstream orientation. Measurements of palaeoflow directions in FA4 are not uniform, and this is expected because they vary with the locations with reference to the meander bend and should show a large spread when plotted all together. Meanwhile, those in FA3 are also different from the uniform distribution, and they have large circular deviation (standard deviation = 90°) and present dispersal pattern as the FA4 sinuous channel sandstone deposits do (standard deviation = 98°). Pryor (1960) suggested that the slope of the depositional surface is the most important factor controlling the circular deviation and dispersal pattern of the paleoflow data, with a larger slope contributing to more uniform paleoflow data. Therefore, we may deduce that the slope was gentle for both FA3 and FA4 deposition. In this context, discharge difference might be the main contributor to the fluvial style change (Leopold and Wolman, 1957). Nevertheless, a wide range of palaeocurrents is also expected in braided rivers due to local flow deflection around bars (Miall, 1994). Therefore, the hypothesis on the slope gentleness needs more evidence for examination.

4.5.2 Geomorphic zonation of the Bighorn Basin

Literature shows that braided rivers evolve into sinuous rivers when certain thresholds in discharge and/or slope are exceeded (Bridge, 1993; Leopold and Wolman, 1957). As analyzed in the above section, the study area might be of a gentle slope during the deposition of FA3 and FA4, and thus the discharge condition may play a critical role in determining the river styles. The study area is far from the southern Owl Creek Mountains, and if it is the only catchment, sinuous rivers should develop in the study area according to the geomorphic zonation theory in river basins (Schumm, 1985). However, braided channel deposits do occur in many cases (48 FA3 vs 39 FA4) in the study area. A hypothesis could be that there have been multiple feeding systems influencing the study area from the western catchments (Owen et al., 2019; Wing and Bown, 1985). Given the proximity of the study area to the western catchment and the high gradient from the western basin margin relative to the southern and eastern margins in the early Eocene, the study area will likely have been fed by multiple western systems that confluence with an axial system flowing south to north. Similar depositional models that include transverse and axial fluvial systems have been reported in modern and ancient outcrop analogs as well as flume experiments (Connell et al., 2012; DeCelles and Cavazza, 1999; DeCelles et al., 1991; Giles et al., 2016; Kim et al., 2011; Weissmann et al., 2015). The southern and eastern catchments are thought to have been lower and possibly more dominated by the reworking of Mesozoic fines (DeCelles et al., 1991). With the feeding of basement-rich western source materials into the axial system of the basin, the sinuous systems may have been alternated or changed into braided systems downstream where discharge was temporarily increased. The western Washakie Range, which is now covered by the Absaroka Mountains (Figure 4.2), was present during the deposition of the Willwood Formation, and it is hypothesized to be an important catchment for the transverse system (Owen et al., 2019), which is supported by the presence of fanglomerates in the western margin of the basin (Kraus, 1984). Therefore, the river planform styles indicated by the rock records in the study area are the interfingering products of at least two fluvial systems, namely one axial system and one transverse system. Accordingly, we reconstruct the paleogeography of the Bighorn Basin during the early Eocene (Figure 4.13). Detailed annotations of elements in this map are listed in the figure caption, with the information provided by existing literature. The presented paleogeographic model represents one possible scenario where FA3 braided channel deposits are dominant in the study area during the period of high or ephemeral discharge conditions. There are some other scenarios when the study area hosts FA4 sinuous channel deposits, probably during the low/perennial discharge conditions. To briefly summarize, water discharge in the main stream is determined by contributions from both axial and transverse systems at the upstream part of the study area, and high/ephemeral discharge conditions favor FA3 braided channel development while low/perennial discharge conditions favor FA4 sinuous channel development.

4.5.3 Controls on fluvial styles and geomorphic zonation

River planform styles depend on several controlling conditions, including water discharge, transport material (bedload vs. suspended load), sediment concentration, valley gradient, and bank material strength (Church, 2006; Schumm, 1985). In an equilibrium-state river channel, sediment concentration is in balance with the valley gradient (Muto et al., 2007;

4
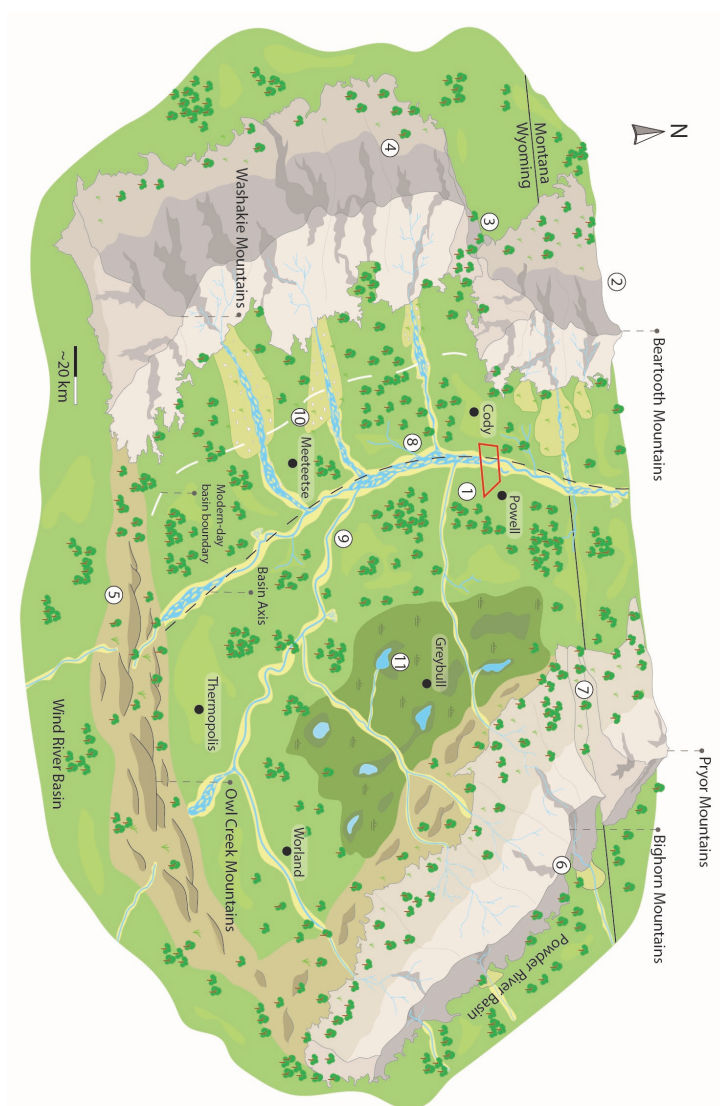
Figure 4.13: Palaeogeographic model of the Bighorn Basin during the Early Eocene. Annotations for elements marked with numbers in the figure are as follows: (1) The McCullough Peaks study area. (2) The Beartooth Mountains with a very steep eastern flank and several ephemeral coarse-grained alluvial fans and braid-plain deposits (DeCelles et al., 1991). (3) The space between the Washakie mountains and the Beartooth during Eocene is uncertain in the literature due to the covering of the Absaroka Mountains. (4) Washakie Mountains not present today (Kraus, 1984), covered by volcanic Absoraka Mountains (Sundell, 1990). (5) The Owl Creek Hills were relatively gentle in Eocene (Wing and Bown, 1985). (6) Unlike the present day, the Bighorn mountains were much smaller and not fully formed in the Eocene (Yonkee and Weil, 2015). The small fine-grained sediment input from the Bighorn Mountains into the Bighorn Basin is due to the large distance and gentle topography from the mountains to the axis. (7) Pryor Gap could be an exit for the rivers during the Eocene (Blackstone, 1940). However, there are no constraints on when it opens. (8) Braided channel belt with mid-channel and side-attached bars. (9) Sinuous channel belt with crevasse splay, local/regional avulsion, and point bars. (10) Fanglomerates on the alluvial fan (Kraus, 1984), indicating a near-source system. (11) Swampy and lacustrine environment in front of the Bighorn Mountains (Davies-Vollum and Wing, 1998; Wing and Bown, 1985)

Wang et al., 2021c). These controlling conditions are also influenced by upstream factors, and the sediment concentration can at times be greater than the transport capacity determined by valley gradient and stream power. When this happens, aggrading and braiding fluvial conditions tend to occur (Church, 2006; Muto et al., 2007; Schumm, 1985). In contrast, the river will tend to entrain sediment and degrade when sediment concentration is lower than the transport capacity, and the preferred mode of transient degradation for the channel is to become more sinuous until the channel gradient is reduced to the required value (Bettess et al., 1983) unless bank strength prevents it from reaching the equilibrium gradient (Church, 2006).

The early Eocene river systems in the Bighorn Basin experienced strong climate alternations likely driven by orbital forcing (Abels et al., 2013), which were signatured by changes in temperature, precipitation, vegetation cover, bank erodibility, suspended load-/bedload ratio, and seasonal contrast (Vandenberghe, 1995, 2003). We posit that other independent proxies (e.g., mature vs. immature paleosols from floodplain deposit; Kraus et al. (2015)) may provide constraints for inference of wetter versus drier periods. However, sandbody data of channel facies associations and other proxy data, such as paleosol data, are not combinedly analyzed yet in Bighorn Basin studies towards paleoclimatic reconstruction. Therefore, a detailed stratigraphic analysis is needed to distinguish stratigraphically and statistically a possible relation between floodplain aggradational cycles (Wang et al., 2021b) and sandstone bodies and their styles to improve the climatic reconstruction in the Bighorn Basin.

4.6 Conclusions

In this study, a comprehensive sedimentological analysis is carried out on outcrops of the lower Eocene Willwood Formation in the Bighorn Basin, USA, using both field-documented data and UAV-photogrammetric model measurements. Four channel lithofacies associations are recognized, which are interpreted to be deposits of four river planform styles: crevasse channel, massive trunk-shaped channel, braided channel, and sinuous channel, respectively, with the latter two styles as dominant ones. Braided and sinuous channel bodies differ significantly in the thickness (on average 6.1 m vs 9.0 m) whereas insignificantly in the width (on average 231 m) and paleoflow directions (on average N003). They are different in lithofacies compositions, but planar cross-stratified sandstone is the most dominant lithofacies in both types of deposits. The alternating presence of sinuous and braided river styles recorded in the stratigraphy offer insights towards the reconstruction of a palaeogeographic model for the early Eocene period. In the schematized model, several transverse systems confluence with an axial system roughly following the basin axis. Contributions from both transverse and axial systems determine water discharge and sediment supply in the channel belt and thus the river style. Findings from our study suggest that channel sandstone body data can be undertaken in an integrated analysis aiming for improved paleoclimatic reconstruction in the Bighorn Basin.

4.7 Acknowledgements

4

5

Astronomical control on the fluvial stratigraphy of the lower Eocene Willwood Formation

Precession-scale climate control was recently demonstrated in the lower Eocene Willwood Formation of the Bighorn Basin. Phases of floodplain aggradation are related to channel avulsion, while phases of floodplain stability are related to channel stability and overbank deposition. Channel sandstone bodies should stratigraphically, geometrically, and spatially relate to these floodplain aggradation cycles. Also, eccentricity may play an important role since it modulates the amplitude of precession cycles. Here, we placed 92 channelized sandstone bodies of different river styles within ca. 300 m stratigraphy straddling 44 precession-driven cycles. We find multiple cases where channel sandstone bodies aggrade upwards from the avulsion-belt deposits and continue to grow during overbank phases. Nearby the channels, the floodplain is subjected to rapid aggradation related to levee and splay deposition, which grade laterally into paleosols. After channel avulsion, on top of the previous channel sandbodies, an avulsion belt lacks, and, instead, overbank fines with pronounced paleosols are present. This could indicate channel superelevation before avulsion with the avulsion belt filling the distant landscape but not the superelevated area on and surrounding the channel belt. Braided and sinuous channel styles occur seemingly mixed in stratigraphy, but they also seem to dominate different stratigraphic intervals. The age control by the early Eocene carbon isotope excursions related to ETM2 and H2 and the 44 precession-controlled floodplain aggradation cycles, allows comparison with a target eccentricity curve. This strongly suggests that the braided channel-dominated interval occurs during 405-kyr eccentricity minima and the sinuous channel-dominated interval occurs during 405-kyr eccentricity maxima. A preliminary model could be to link flashy runoff, less dense vegetation cover, and increased sediment load to eccentricity minima, and more constant runoff, denser vegetation cover, and lower sediment loads to eccentricity maxima.

5.1 Introduction

Alluvial stratigraphy carries informative signatures of environmental signals as climate, tectonics, and eustacy (Blum and Törnqvist, 2000; Hajek and Straub, 2017) in combination with autogenic processes (Hajek et al., 2012). When these signals are periodic and thus quasi-predictive, cyclic patterns could potentially be preserved in the stratigraphic record, depending on the signal robustness (Wang et al., 2021c). Research on base-level-driven fluvial cyclicity that integrates channelized sandstone bodies in the coal/paleosol-formed stratigraphic framework has proliferated (Atchley et al., 2004; Hampson et al., 2013). However, in some fluvial settings, these cycles are rarely influenced by base-level changes at orbital timescales, and instead, they are driven by orbital climate change controlling water discharge and sediment load (Noorbergen et al., 2018, 2020). With its ability to incur climatic variability over 10^4–10^5 year timescales, orbital forcing has been demonstrated in extensive marine and lacustrine sedimentary archives (Abels et al., 2010; Huang and Hinnov, 2019; Kuiper et al., 2008; Littler, 2014; Lourens et al., 2005), with proxies like stable carbon isotope ($\delta^{13}C$) and oxygen isotope ($\delta^{18}O$) ratios of deep-sea foraminifera (Kocken et al., 2019). However, it is challenging to be proven in the fluvial realm that is subjected to fragmentary sedimentation and stratigraphic incompleteness (Fielding and Webb, 1996; Hilgen et al., 2015). Successes have been achieved in several successions across several sedimentary basins (Abdul Aziz et al., 2003, 2008; Aswasereelert et al., 2013; de Boer et al., 1991; Fielding and Webb, 1996; Noorbergen et al., 2018, 2020; Olsen, 1990, 1994; Smith et al., 2014).

Continuous aggradation in pace with accommodation generation is one of the key factors that help reveal the allogenic forcing on alluvial architecture. The recently reported floodplain cyclicity in the Bighorn Basin provides an opportunity to investigate the impact of orbital climate change on alluvial stratigraphy (Abels et al., 2013), which reveals the presence of precession and possible eccentricity. More recently, highly-detailed mapping and characterization of paleosols and sandstone bodies are implemented in a fully-georeferenced UAV-based photogrammetric model that covers an area of ~10 km² and a composite stratigraphy of ~300 m (Chapters 3 and 4). With these studies, more insights are gained into the spatial consistency and variability of floodplain aggradation cycles as well as the characteristics and interpreted paleoclimate-paleoenvironment of sandstone deposits. Here, we now integrate the floodplain aggradation cycles and the channel sandstone bodies in a detailed stratigraphic context, to determine the regularity and thus predictability of sandstone bodies in the orbitally-forced stratigraphy. The objective of this study is threefold: (1) to reveal the lateral configuration between different styles of channelized sandstone bodies and precession-driven floodplain aggradation cycle boundaries; (2) to determine possible eccentricity-control on these sandstone bodies within the stratigraphic framework built by floodplain aggradation cycles; (3) to develop a stratigraphic model that can explain the genetic mechanism of the channel sandstone bodies.

5.2 Dataset and methods

The study area lies in the McCullough Peaks, Wyoming (Figure Figure 5.1), where Paleocene-Eocene alluvial deposits of the Willwood Formation exhibit sandstone body architecture that was dominantly controlled by alternating avulsion and overbank phases (Abels et al.,
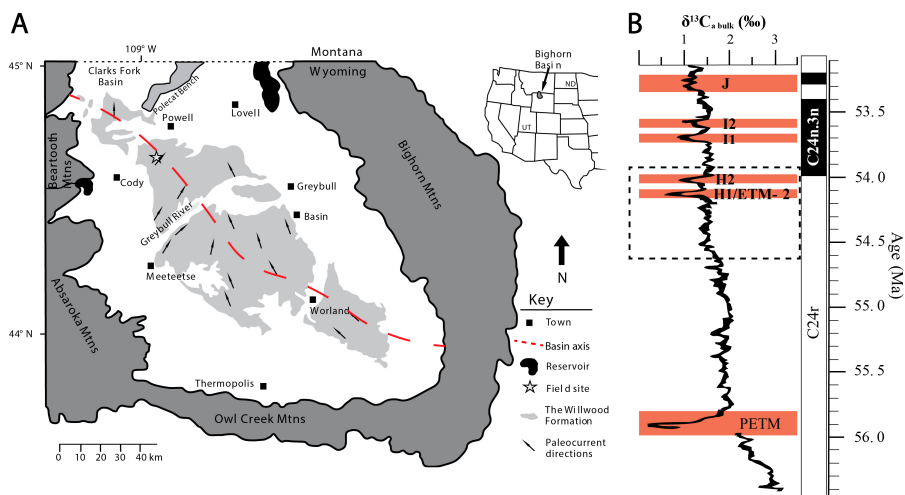
Figure 5.1: (A) The location of the study area, the McCullough Peaks, in the northern Bighorn Basin, Wyoming, USA (after Wang et al. (2017)). Paleoflow data indicated by the arrows are from Neasham and Vondra (1972). Note that the Washakie Range present during the Eocene is now covered by the Absaroka Mountains (Yonkee and Weil, 2015), and the Pryor Mountains present during the Eocene are now not distinguishable from the Bighorn Mountains (Blackstone, 1940). (B) Adjusted $\delta^{13}C_{a\ bulk}$ data from Zachos et al. (2010) by Birgenheier et al. (2019), with orange rectangles indicating hyperthermal events and the dashed rectangle indicating the study interval.

5

2013). The Willwood Formation is a 1400-m-thick succession of mudstone and sandstone interpreted as distal- and proximal-overbank alluvial deposits and trunk-channel deposits, all of which are modified by varying degrees of pedogenesis (Kraus, 2002).

Lithofacies and lithofacies associations were characterized in the field survey, including grain size, lithology, sedimentary structure, geometry, boundaries, palaeo-flow directions, and dimensions. Based on this dataset, a stratigraphic analysis was implemented based on high-resolution (~10 cm) georeferenced photogrammetric data covering ~10 km² of the McCullough Peaks area and straddling a composite stratigraphy of ~300 m. Methods for the acquisition and processing of unmanned aerial vehicle (UAV) images into photogrammetric models have been detailed in Chapter 3 of this dissertation. The stratigraphic level with the sharpest transition from the colored paleosol layer to the whitish avulsion belt deposit is defined as the cycle boundary and has been extensively mapped in the photogrammetric model (Chapter 3 of this dissertation). Channelized sandstone bodies are systematically characterized and interpreted in our previous work (Chapter 4 of this dissertation), and they are grouped into three broad categories: (1) single-story sinuous channel sandstone bodies with typical lateral accretion; (2) multiple-story (average: 3.5 stories) braided channel sandstone bodies with typical vertical and downstream accretion; and (3) sharply-confined massive trunk sandstone bodies lacking obvious internal architecture. The stratigraphic framework is largely overlapping with the carbon isotope records of pedogenic carbonate produced by Abels et al. (2012, 2016) where Eocene hyperthermals ETM2 and H2 are recognized and represented by the carbon isotope excursions (CIEs). The 44 floodplain aggradation cycles are regarded as driven by precession, and thus each cycle is assumed to have a duration of ca. 20 kyr (Zeebe and Lourens, 2019).

5.3 Results

5.3.1 Stratigraphic Relation Between Sandstone Bodies and Flood-plain Aggradation Cycles

We locate the 92 sandstone bodies within the stratigraphic framework of the adjacent floodplain aggradation cycles both in the field and in the UAV-based photogrammetric model. Detailed stratigraphic placement of all channel sandstone bodies in relation to floodplain aggradation cycles is impossible due to outcrop quality and in many cases model resolution limitations. Floodplain sediments near channel sandstone bodies are relatively coarse-grained and therefore covered by more vegetation and recent debris, making it difficult to recognize floodplain aggradation cycle boundaries. In areas distant from the channel sandstone bodies, floodplain aggradation cycles are relatively easy to recognize, and they are featured by intervals of sandy, heterolithic bedded deposits alternating with floodplain fines on which paleosols developed. Similar alternations are more frequent in the proximity of channel sandstone bodies, but they are not laterally consistent. Paleosols directly on top of channel sandstone bodies are very well developed, while splay and levee deposits dominate in the lateral of channel sandstone bodies (Figure 5.2A).

In our current work, we do not discriminate the precession-scale stratigraphic relationships between different river styles of sandstone bodies and adjacent floodplain aggradation cycles because we are not sufficiently confident yet about them due to the limited amount of channel sandstone body-floodplain contacts that can be clearly observed in the field and photogrammetric model. Lack of fieldwork in 2020 due to the global pandemic halted additional data gathering in the field by clearing surface weathering for example and observing outcrops from angles not documented in the UAV-based photogrammetric model. Therefore, for now, we regard the channel sandstone bodies as of similar styles, even though we anticipate that each style may have a (slightly) different stratigraphic and genetic relation with the floodplain aggradation cycle.

Channel sandstone bodies are in many cases found to initiate at the end of the avulsion phase, possibly at the place of the splay channel. They in many cases scour deep into the floodplain deposits, making it difficult or impossible to relate their initiation at a certain location stratigraphically to the adjacent floodplain. Scouring occurs typically in the five massive trunk-shaped channel sandstone bodies, but it is also seen in sinuous and braided counterparts. Following scouring, the channel bodies continue to grow throughout the whole overbank phase, as is indicated by intercalations of connected levees and splays with the adjacent floodplain stratigraphy (Figure 5.2A). Lateral tracing of these dm-thick sandy beds starting from the channel sandstone bodies reveals that these beds are eventually completely incorporated into the floodplain deposits at a scale of up to 1 km. Soil intensity and thickness increase away from the channel sandstone bodies. On top of channel sandstone bodies, we usually find intervals of strong soil development, which are demonstrated to relate to the overbank phases of the floodplain aggradation cycle by tracing them laterally (e.g. the top of Cycle 3 in Figure 5.2B). The floodplain sediment directly adjacent to the sandbodies also relates to an overbank interval (e.g. the top of Cycle 2 in Figure 5.2B). The intermediate avulsion-belt deposits thicken laterally away from the channel sandstone bodies, while they are absent or thin near and above the channel sandstone bodies (e.g. the avulsion phase at the bottom of Cycle 3 in Figure 5.2B).

5.3.2 Stratigraphic Variations of River Styles

The 92 channelized sandstone bodies of different fluvial styles are subsequently placed in a stratigraphic framework of 44 precession-driven floodplain aggradation cycles. There are 48 braided channel sandstone bodies, 39 sinuous channel sandstone bodies, and 5 massive trunk-shaped channel sandstone bodies (Figure 5.3). The stratigraphy is produced using the photogrammetric model from roughly north to south, and channel sandstone bodies are placed roughly at their respective lateral positions within the photogrammetric model. Their widths are calibrated using the average paleoflow direction (N004).

In the very basal parts of the successions, we find two braided systems and one sinuous system (i.e. cycles A-4, A, and B, Figure 5.3). From cycle D until cycle Q, there are 25 sinuous channel sandstone bodies, 9 braided channel sandstone bodies, and 4 potentially braided channel sandstone bodies. Sinuous channel sandstone bodies in this interval (n = 25, on average 323 m wide and 9.3 m thick) are significantly wider (t = 2.1, p = 0.04) and significantly thicker (t = 3.4, p = 0.002) than braided ones (n = 13, on average 230 m wide and 5.9 m thick). The interval can thus be regarded to be dominated by sinuous river styles. Moreover, in this sinuous river dominated interval, the sinuous channel thickness seems to first increase (i.e. cycle D to H), then decrease (i.e. cycle H to J), again increase (i.e. cycle J to M), and then decrease (i.e. cycle M to Q). Above cycle Q up until cycle Z, there are 22 braided channel sandstone bodies, 2 possibly braided channel sandstone bodies, 3 sinuous channel sandstone bodies, and 1 or 2 massive trunk-shaped channel sandstone bodies. In this interval, the number of braided channel sandstone bodies is much larger than that of sinuous counterparts. The interval is thus clearly dominated by braided river styles. In this interval, the braided channel thickness seems to first increase from cycle Q to cycle U and then decrease from cycle Q to cycle Z. Moreover, we compared the braided channel sandstone bodies in the sinuous-dominated interval and those in the braided-dominated interval, and we find the former (n = 13, on average 170 m wide and 6.2 m thick) is insignificantly narrower (t = 1.1, p = 0.3) and insignificantly thicker (t = 0.4, p = 0.7) than the latter (n = 24, on average 230 m wide and 5.9 m thick). From cycle P1 upwards, there are 11 sinuous channel sandstone bodies, 7 braided channel sandstone bodies, and 3 massive trunk-shaped channel sandstone bodies. This interval, with the presence of hyperthermal ETM2 and H2, is slightly dominated by sinuous river systems. Spatially, we do not see a dominance of river styles in different regions of the study area (see Chapter 4).

The floodplain aggradation cycle-framed stratigraphy is compared to the marine-deposit color record and eccentricity target curves generated by Zeebe and Lourens (2019). This is done with carbon isotope excursions of ETM2 and H2 as constraints (Abels et al., 2016), and the curves are linearly scaled according to our precession cycle counting. For example, there are 25 precession cycles in the interval of 54-54.5 Ma, assuming that each precession cycle lasts ca. 20 kyr and each long eccentricity cycle lasts 405 kyr. The sinuous-dominated interval between cycles D and Q coincides roughly with the maximum of the 405-kyr long eccentricity (see the corresponding blue interval in the target curves of Figure 5.3). In contrast, the braided-dominated interval between cycles Q and Z coincides roughly with the 405-kyr eccentricity minimum (see the corresponding orange interval in the target curves of Figure 5.3). The upper interval, above cycle Z until cycle P8, which is slightly dominated by sinuous systems, occurs during the next 405-kyr maximum, while the very upper part, from cycle P8 to cycle P16, coincides with the subsequent eccentricity minimum.

At the 100-kyr short eccentricity scale, it is more difficult to compare sandstone bodies of different fluvial styles with the target curves, because of the likely present undercounting or overcounting of individual precession cycles in some intervals. Also, it is not always certain where to stratigraphically place the sandstone bodies with respect to the floodplain aggradation cycles due to unclear channel-floodplain contacts obscured by recent debris, vegetation, and insufficient model resolution. It could be tempting to relate the occurrences of some fluvial styles to short eccentricity changes, such as the sinuous system in cycle W that corresponds to the short eccentricity maximum and the braided system in cycle Z that corresponds to the short eccentricity minimum. However, cycles P and Q in the short eccentricity minimum lack the expected braided systems, and cycle M in the short eccentricity maximum lacks expected sinuous systems. Moreover, the interval above P1 that contains ETM2 and H2 hyperthermal events shows a more seemingly chaotic occurrence of river styles with respect to the short eccentricity curve, partly because this interval is of limited outcrop exposure and thus some stratigraphic levels are found with no channel sandstone bodies (e.g. cycles P5 and P6 in Figure 5.3).

5.4 Discussion

5.4.1 Precession-Driven Sedimentary Cycles

The vertically repetitive and laterally consistent precession-driven floodplain aggradation cycles would logically result in related geometry, character, and stratigraphy of channel sandstone bodies. Floodplain aggradation cycles have been interpreted as alternating phases of channel stability and channel avulsion (Abels et al., 2013). The thickness of channel sandstone bodies is thus expected to relate to the thickness of floodplain aggradation cycles, although lateral cycle thickness variability due to channel belt locations and splaying renders the exact relationship between them unknown. The average channel sandstone body thickness of the 92 sandstone bodies in Figure 5.3 is 7.4 m, while the average floodplain aggradation cycle thickness is 6.8 m (see Figure 3.6 in Chapter 3). Whether such proximity of thicknesses of floodplain aggradation cycles and channel sandstone bodies represents a stratigraphic rule remains to be sorted out.

Channel sandstone bodies seem to stratigraphically originate at the top of avulsion-belt deposits, and they are probably related to the splay channel at that location, which gradually evolves into the main channel that sustains in the overbank phase. The occasional deep scouring of channel sandstone bodies prevents the determination of their exact stratigraphic position with respect to the floodplain aggradation cycles. Such scouring should relate to phases of increased discharge lowering fluvial gradients Chapter 2. Possibly, deeper scouring and rapid filling in most cases relate to massive trunk river systems and braided river systems, while gradual building-up processes contribute to more sinuous systems. However, we did not observe this character in contrast to some other sandstone body descriptions elsewhere (Noorbergen et al., 2018, 2020).

The gradual building-up of the channel-belt sandstone body in pace with the overbank floodplain aggradation fits the model of Abels et al. (2013), in which overbank phases are characterized by relative channel stability during which superelevation is steadily reached. Part of the lateral thickness variability of floodplain aggradation cycles observed in Chapter 3 can thus be explained by a thicker overbank interval in the proximity to channel belts

and less overbank deposition farther away from the channels. Well-developed paleosols on top of the channel sandstone bodies may reflect the influence of the paleohigh that results from rapid sedimentation and superelevation of the channel belt before avulsion took place. It could indeed be possible to characterize channel sandstone bodies using the floodplain-framed stratigraphy, at least in terms of sandstone body thickness but possibly also in terms of lateral location and stratigraphic position of these sandstone bodies. However, to provide a full model for the latter, we need more observations concerning the lateral character and relation of floodplain deposits and the stratigraphy away from channel belt sandstone bodies.

We reproduce the cross-section surface topography of two scenarios (non-cyclic Scenario NC and cyclic Scenario A10) that have been introduced above (Chapter 2), with timelines of shorter intervals and indications of channel belt locations (Figure 5.4). In Scenario NC (Figure 5.4A), channel belt locations are more randomly scattered with various lifespans, and there are no regular alternations between "overbank phases" represented by highly overlapped timelines indicating non/slow-deposition and "avulsion phases" represented by vertically spaced timelines indicating rapid aggradation. In contrast, in Scenario A10 (Figure 5.4B), we observe clear distinctions between overbank phases with channel stability and avulsion phases with channel instability. Meanwhile, more significant superelevation is commonly seen in the clustered channel belt location, such as the channel belt at the top of Cycle 1 (Figure 5.4B). Moreover, these channel belts are indeed initiated at the end of the avulsion phase, which is consistent with our above analysis based on field observations (i.e. Figure 5.2). An increase in the amplitude of the water discharge/sediment supply ratio would strengthen the difference between Scenarios A10 and NC we illustrated here, which has been presented in Chapter 2, including clearer distinctions between overbank and avulsion phases, deeper channel scouring and higher channel stability in the overbank phases, and more rapid aggradation in the avulsion phase (see Figure 2.9 in Chapter 2). The similarity between model behaviors and outcrop features may indicate similar processes that happen in numerical models and reality.

5.4.2 Impact of Eccentricity on River Styles

The essential geomorphological distinction between braided and sinuous river styles is the sinuosity index (Alabyan and Chalov, 1998; Bettess et al., 1983; Candel et al., 2021; Carson, 1984; Schumm, 1985), which is indeed a continuum, generally with a gradual downstream increasing trend. Sinuous river planform could be changed into braided counterpart under certain conditions (Skirrow et al., 2021), including (1) increased sediment supply driven by vegetation change and sediment availability (Kasse et al., 2005; Leigh, 2006); (2) increased river discharge (Leigh, 2006; Peirce et al., 2018); (3) increased discharge variability caused by enhanced seasonality (Fielding et al., 2018; Manna et al., 2021). When a certain threshold is exceeded and the sinuosity index decreases below a certain value, the obvious sinuous river patterns are replaced by obvious braided ones. There are some uncertain fluvial styles in our interpretation due to lack in obvious discriminant features, which may correspond to the transitional state between braided and sinuous river planforms.

The 100 kyr and 405 kyr eccentricity have strong imprints on the Cenozoic climate (Westerhold et al., 2011). They have minor effects on the total annual insolation (Laskar et al., 2011), but they dominantly act on the climate system as an amplitude modulator

5
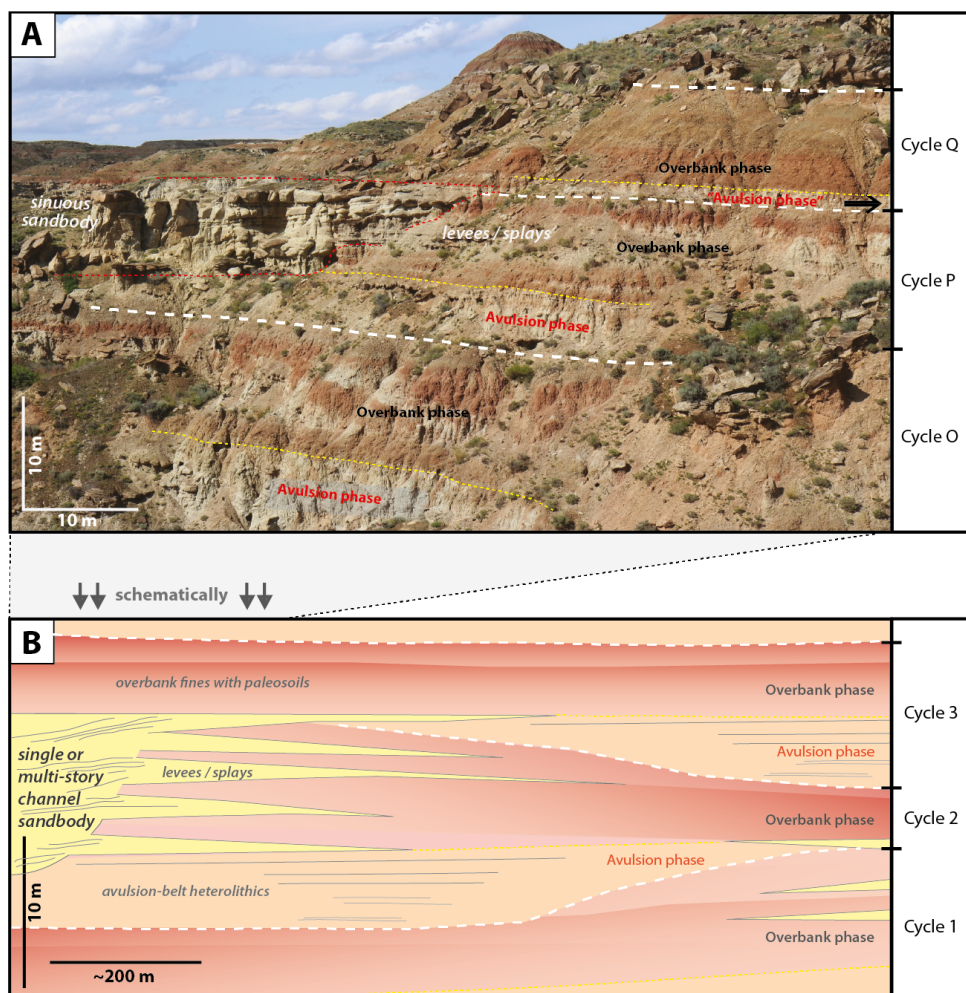
Figure 5.2: (A) Outcrop photograph of the contact between multi-story sinuous channel sandstone bodies and the adjacent floodplain deposits showing the interfingering of levees and splays with the floodplain paleosols. Floodplain aggradation cycles O, P, and Q have been identified in this outcrop based on the lateral tracing of these cycles in the complete photogrammetric model. The respective overbank and avulsion phases are indicated. Note the absence of the avulsion phase related to cycle Q, likely because the location was a topographic high due to the channel belt build-up at this location. White dashed lines indicate the overbank to avulsion phase cycle boundaries and yellow dashed lines avulsion to overbank phase changes. (B) Schematic model incorporating channel sandstone body into the precession-driven overbank-avulsion cycles. The model is based on all observations, not only those in subfigure 5.2A. Note the larger lateral scale compared to subfigure 5.2A to denote the more distant sedimentary and stratigraphic character away from the channel.
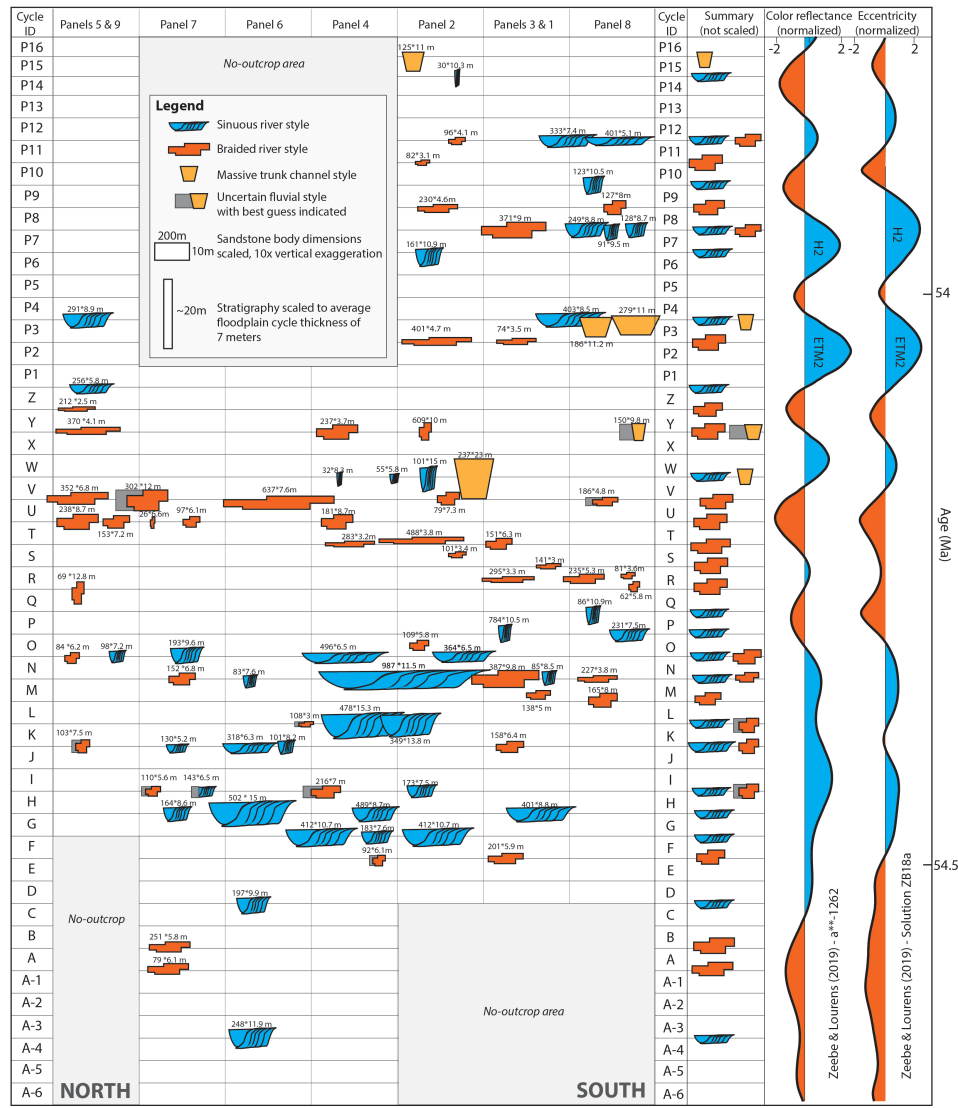
Figure 5.3: Stratigraphic occurrence of channel sandstone bodies and their geometries and river styles throughout the stratigraphy in the lower Eocene Willwood Formation in the Deer Creek area of the McCullough Peaks, Bighorn Basin, WY. Sandstone bodies are depicted in stratigraphy from roughly north to south following the photogrammetric panel numbers given above, which can be found in Chapter 3. Some areas lack outcrops for certain stratigraphic intervals. Floodplain aggradation cycle labels are provided in Chapter 3. To the right, a summary is given about the river style of channels in each floodplain aggradation cycle. To the very right, one marine-deposit color reflectance curve and one eccentricity curve provided by Zeebe and Lourens (2019) are calibrated against the known ETM2 and H2 intervals and linearly scaled according to our precession cycle counting, with arbitrary threshold lines separating high values from low values.
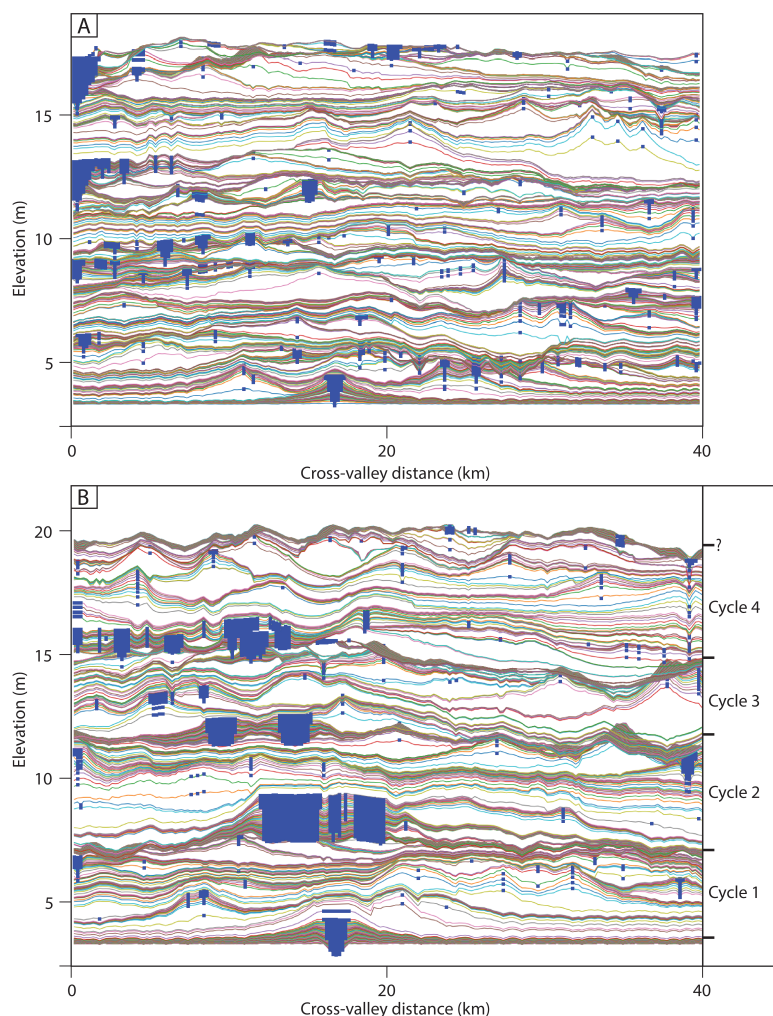
Figure 5.4: Cross-section surface topography along line BB' (see its position in Chapter 2) of multiple moments with a time interval of 100 years. (A) Scenario NC with a constant water discharge/sediment load ratio. (B) Scenario A10 with the cyclic variation of water discharge/sediment load ratio. Colored lines indicate the topography at different time moments, while blue squares indicate the location of the channel belt at a certain time moment, without indication of the channel belt thickness. Note the more ordered alternation of avulsion and overbank phases in subfigure A and the constant aggradation in subfigure B.

of precession, causing a greater seasonal contrast during eccentricity maxima and driving carbon cycle dynamics and early Eocene hyperthermal events (Abels et al., 2016; Zeebe and Lourens, 2019). The insolation variation can result in precipitation fluctuation, which can further lead to river discharge variations at precession and eccentricity scales (Rossignol-Strick, 1983). In this study, we find a seemingly good correlation between dominant river styles and long eccentricity (405 kyr; Figure 5.3), making it tempting to consider the role

of eccentricity in controlling river styles in the early Eocene Bighorn Basin.

The channel thickness variability seems to follow regular rules related to the eccentricity curve (Figure 4.3). The increasing-decreasing-increasing-decreasing sinuous channel depth in the sinuous river-dominated interval may be directly related to the precession-driven insolation changes modulated by short and long eccentricity. Similar phenomenon has been reported by Olsen (1990), who presents meandering river behaviors driven by precession cycles with modulation by short eccentricity mega-cycles.

Eccentricity may directly influence local climates as the amplitude modulator of precession and thus influence water discharge and sediment load within the early Eocene river systems. As precession strongly impacts seasonality, it would be tempting to relate river style changes to seasonality variation. However, eccentricity may also control climate more remotely or even globally at this time and climatic teleconnections change local climates. The carbon cycle in this period of time is dominated by short and long eccentricity, also in the periods without pronounced hyperthermal events, and the carbon cycle lacks a lot of signs of precession or obliquity's influence (Lauretano et al., 2018). This could point to a relative dominance of eccentricity on global climate change, even though the local record in the Bighorn Basin is shown to be dominantly influenced by precession that drives the floodplain aggradation cycles (Abels et al., 2013). At this stage, we are not sufficiently confident to relate the observed changes to either local eccentricity controls via seasonality changes or global eccentricity-related climatic changes, and more field evidence is needed.

One would expect that ETM2 and H2 hyperthermal events had considerable impacts on fluvial systems as these events are shown to have impacted local systems (Abels et al., 2010; D'Ambrosia et al., 2017; Smith et al., 2014) with severe global change. Our observations of fluvial channel sandstone bodies do not provide a straightforward linear response to either of the hyperthermal events. In contrast, the lower interval, from cycle D to Z seems much more linearly relating to eccentricity forcing with a long interval dominated by sinuous river systems followed by an interval dominated by braided river systems. The hyperthermal interval is dominated by a mix of both styles interfingered by the enigmatic massive trunk-shaped channel systems. Clearly, the ETM2 does not behave like a smaller version of the preceding PETM event that is known by its very extensive and thick braided channel sandbody in the same parts of the Bighorn Basin (Foreman, 2014).

Moreover, the scattered braided channels in the sinuous-dominated interval (cycles D to Q) might be related to flashy discharge conditions in the high seasonal contrast period (Fielding et al., 2018; Manna et al., 2021), while those in the braided-dominated interval (cycles R to Z) might be related to high discharge conditions in the low seasonal contrast period (Fielding et al., 2018; Manna et al., 2021). More field evidence is needed to examine this. Vegetation could play a very important role in determining sediment availability in the catchment and bank erodibility in the river course (Vandenberghe, 1995, 2003), which, however, is not considered here.

The precession-scale stratigraphic model provides important information on the predictability of sandstone body stratigraphy, geometry, and character. Moreover, the observed eccentricity control further enriches such an orbitally forced stratigraphic model as thicker and narrower sinuous channel sandstone bodies may dominate during eccentricity maxima, while thinner and wider braided channel sandstone bodies may occur more

during eccentricity minima. Intervals of different connectivity, N/G ratios, and lithologic heterogeneity may be pinpointed in this way, accompanied by proposals of different exploration and exploitation strategies for different intervals. Nonetheless, at this stage, the study leaves a lot of detailed questions as to how exactly the difference between braided and sinuous river styles originates and what is the meaning and cause of the few massive trunk-shaped channel sandbodies within the stratigraphy. These puzzles will be the topics of our future research.

5.5 Conclusions

In this study, an integrated field study is performed to investigate the role of astronomical climate change in the lower Eocene alluvial stratigraphy of the Willwood Formation in the northern Bighorn Basin, Wyoming, USA. We studied sandstone bodies intercalated in a ca. 300 m thick stratigraphy that has revealed 44 precession-driven floodplain aggradation cycles. Channel sandstone bodies mostly start their build-up at the end of the avulsion phase, likely at the location of the main crevasse channel. The bodies subsequently grow upwards during the so-called overbank phases characterized by distant floodplain sedimentation on which mature paleosols develop. When superelevation of the channel belt is reached over the distal floodplains, channels avulse, leaving a topographic high location on which only fine sediments arrive and thus mature paleosols develop. Our dataset provides evidence for an intrinsic relation between precession-driven floodplain aggradation cycles and intercalated sandstone bodies. In the long term, we find intervals dominated by sinuous channel sandstone bodies and intervals dominated by braided channel sandstone bodies. The stratigraphic variation of river styles is then compared with the marine proxy curve and the eccentricity target curve, which demonstrates the relation of sinuous river styles to 405 kyr eccentricity maxima and that of braided river styles to 405 kyr eccentricity minima. While there remain a lot of details to be studied, these findings demonstrate that orbital climate forcing was the main driver in controlling alluvial architecture in the early Eocene Bighorn Basin, Wyoming.

5.6 Acknowledgement

6

Synopsis

In this chapter, we recap the achievements that have been made in this Ph.D. project and look forward to the bright future when we can potentially extend understandings gained in this project to a wider field.

6

6.1 Synthesis

The results presented in this dissertation demonstrate the alluvial stratigraphic response to orbital climate change from perspectives of both sedimentary processes and products using numerical modelling and outcrop analysis. Our numerical exercises elucidate the requirement on signal robustness (i.e. wavelength and amplitude) for signal preservation in the stratigraphic record. Moreover, compensational stacking is explored in numerically modelled stratigraphy. Outcrop results fit well with our numerical model run results from many perspectives. Regionally mapped paleosol layers as floodplain aggradation cycle boundaries show strong regional consistency and also both vertical and lateral variability. Sedimentological analysis of channelized sandstone bodies reveals sedimentary processes in different river planforms, based on which we reconstruct the paleogeomorphology of the Bighorn Basin that fits the geological context provided by existing studies. With paleosol layers as the stratigraphic framework with good time control and sandstone bodies as the fillings within the framework, we establish stratigraphic models that explain vertical alternation of river styles and provide a predictive link between orbital climate forcing and alluvial architecture. More detailed synthesis is presented below to address the hypotheses that we have made in the Introduction chapter.

6

6.1.1 Process-based numerical modelling

In Chapter 2, we evaluate the effect of cyclic and non-cyclic upstream forcing on alluvial stratigraphy using a process-based alluvial architecture model (Karssenberg Bridge, 2008). We find cyclicity is preserved in the sedimentary records when the sediment load over water discharge (Q_s/Q_w) ratio has sufficiently large amplitudes and long, but not very long, wavelengths, the absolute values of which depend on inherent properties of the modelled basin. Within one allogenic cycle, there are a non-deposition phase and an aggradation phase. After the Q_s/Q_w ratio starts to decrease, the non-deposition phase occurs, during which channel belts are confined and stable at certain locations, and the vast floodplain undergoes very low sedimentation. The aggradation phase occurs after the Q_s/Q_w ratio starts to increase for a while, accompanied by sedimentary filling in the channel belt and creation of channel belt superelevation over the adjacent floodplains. Frequently shifting channel belts cause rapid sedimentation over the entire basin. The non-deposition and aggradation phases are comparable to the overbank- and avulsion-phases as identified in field successions in the Bighorn Basin, Wyoming, USA, which are attributed to precession-paced climate changes. In the KB08 model, larger forcing amplitudes result in longer non-deposition phases due to the fact that longer time is needed to fill the deeper-incised channel belts before superelevation can be reached. The upstream Q_s/Q_w signal is shredded in the downstream transmission process, and large amplitudes are more favorable for Q_s/Q_w signal preservation. We identify compensational time scales in the fully autogenic model runs by applying the method of Straub et al. (2009), and we find that the presence of an allogenic forcing will strongly influence the compensational time scale of a transport system. Findings of this study provide insights into the transmission and preservation processes of upstream cyclic Q_s/Q_w signals, during which allogenic and autogenic forcings interact with each other to produce alluvial stratigraphy.

6.1.2 Characterization of floodplain aggradational cycle

In Chapter 3, we present a fully-georeferenced 3D photogrammetry model that covers an area of 10 km² and a succession thickness of 300 m in the McCullough Peaks Area of the Bighorn Basin. There are a total of 44 fluvial aggradational cycles recognized in the studied stratigraphy, with an average thickness of 6.8 m and a standard deviation of 2.0 m, which is in line with previous studies. Most cycles are consistently traceable over the entire model, indicating spatial consistency and in line with allogenic climate forcing by the astronomical precession cycle. Individual floodplain aggradation cycles may change in thickness rapidly when traced laterally, with rates up to 1 m over a lateral distance of 100 m and a maximum of 4 m. Detailed mapping of seven successive cycles reveals differences in their regionally-averaged thicknesses of 3.7 m to 9.7 m, with their coefficients of variation ranging between 17% and 28%. Variogram analysis demonstrates that the thickness of a cycle at one locality is statistically related to that at another locality over an average distance of 1.3 km in the paleoflow direction and 0.6 km perpendicular to the paleoflow direction. These different directional trends are interpreted to result from morphological elements oriented in paleoflow directions in the fluvial landscapes shaping more consistency of the sedimentary elements in paleoflow direction. Two different metrics suggest that full-compensational stacking occurs after deposition of 6 to 7 cycles, or timescales of ca. 120 to 140 kyr, although strong thickness compensation is shown to start at the subsequent one and two floodplain aggradation cycles, so at ca. 20-40 kyr time scales.

6.1.3 Channelized sandstone characterization

In Chapter 4, a comprehensive sedimentological analysis has been carried out on outcrops of sedimentary deposits of the Eocene Willwood Formation in the Bighorn Basin. A total of four styles of channel sandstone bodies are recognized, which are interpreted to be deposits of floodplain distributary channel, large-scale massive trunk-shaped channel, sinuous channel, and braided channel, with the latter two taking volumetric dominance. Specifically, braided and sinuous deposits are different in lithofacies compositions, yet planar cross-stratified sandstone is the most dominant lithofacies in both types of deposits. Moreover, sinuous channel sandstone bodies (averaging 8.9 m) are generally thicker than braided ones (averaging 5.6 m), while sinuous channel belts (averaging 0.7 km) are narrower than braided ones (averaging 2.0 km). The alternating dominance of sinuous and braided river planforms recorded in the stratigraphy is explained by the newly established depositional models with three possible scenarios. The study area is mainly influenced by the axial far-source fluvial system and the transverse near-source system. Whether the study area archives braided or sinuous channel deposits depends on whether the geomorphic sinuous-braided threshold of bankfull discharge is crossed when the transverse system joins the axial system. More detailed stratigraphic analysis, assisted by palaeosol layers as the marker beds, is required to more detailedly investigate the alluvial response to climate changes.

6.1.4 Fluvial cyclostratigraphic analysis

In Chapter 5, we locate 92 channelized sandstone bodies of different fluvial styles (i.e. sinuous and braided) in the 300 m stratigraphy that straddles 44 cycles. Here we report different stratigraphic locations of sandstone bodies of different fluvial styles. Specifi-

cally, sinuous channel sandstone bodies are initiated at the end of the avulsion phase and they continue growing through the whole overbank phase until the next avulsion phase starts. In contrast, braided channel sandstone bodies are initiated in the avulsion phase and stopped before the overbank phase. Moreover, a dominant sinuous channel interval with scattered braided channel sandstone bodies is found to well relate to the eccentricity maxima of a proxy curve from the marine record, while a dominant braided channel interval with no sinuous hannel sandstone bodies is found to well relate to the eccentricity minima of that curve. In this way, we build predictive genetic links between river styles and orbital climate forcing.

6.2 The bright future

The application of cyclostratigraphy is challenging in the fluvial realm that is vulnerable to fragmentary sedimentation (Hilgen et al., 2015). Our results present promising insights on favorable conditions for environmental signal preservation in the fluvial record, which can act as a foundation to extend the research to either the upstream source area or the downstream deltaic and marine environments. Moreover, extreme climatic events can be also investigated in the future to constrain findings of this dissertation concerning longer-period orbital forcing. The predictive link between orbital forcing and alluvial response can be potentially applied in the subsurface energy exploitation to reduce the exploration risk, because the rules extracted from our conceptual models are based on extensive datasets from suitable outcrops while subsurface cases normally have much more limited datasets.

6.2.1 Catchment modelling

Many interpretations of numerical modelling and outcrop analysis results made in this study are based on simplified assumptions, especially when it comes to the sediment calibre and water discharge in the catchment. However, the reality is much more complex than the assumptions this dissertation has made. As a countermeasure, landscape evolution models should be employed to output more realistic environmental signals that can be used as inputs for the processed-based alluvial model. There are mainly two types of models on this, namely the stream-power river incision model and the diffusive transport-limited model (Armitage et al., 2013, 2017; Whipple et al., 1998; Whipple, 2001).

Moreover, tectonic forcing should also by some moment be involved to test the alluvial response to sudden tectonic changes. Basin subsidence rate is an important term in the numerical modelling. It is mimicked by base level change and set to be constant in Chapter 2, whereas over a longer timescale, a sudden increase or decrease of it might significantly influence the sediment generation in the catchment, sediment preservation in the transfer zone, and eventually sediment accumulation in the sink (Whittaker and Boulton, 2012).

6.2.2 Impact of orbitally forced rivers on lacustrine and marine environments

In the context of the source-to-sink system, there are mainly three zones: source zone where weathering and erosion takes place, transfer zone where fluvial processes occur, and sink zone where sediment finally accumulate (Romans et al., 2016). It is important

to look into the sediment flux variation at the sink zone considering signals generated in the catchment and sediment stored and released in the transfer zone. This has been tentatively mentioned in Chapter 5, where there seems to be climatically forced transgression and regression (Figure 2.8). A more straightforward application is to investigate the shale deposition in the marine/lacustrine environments. For instance, sediment flux in rivers may vary with time and processes, and sediment composition may also vary. In this case, there might be regularly alternating mud-rich and calcite-rich deposit in a shale laminae. If this process is linked to eccentricity, it will become feasible to predict shale deposition features over a long timescale, which will facilitate the resource evaluation and exploitation.

Moreover, base level variation has been extensively studied in the past decades (Hampson et al., 2012, 2013). However, it has not been tested how upstream climate forcing interacts with downstream base level variation with various amplitude, wavelength, and phasing issues. A practical exercise would be to evaluate how high-frequency sediment/water cycles (e.g. 20 kyr) interact with low-frequency base level cycles (e.g. 100 kyr or higher). Interaction is expected to be somewhere in the central part of the basin. But where exactly and how they interact are not known, and what parameters are key to determine these is to be explored.

6.2.3 Longer-period orbital forcing and extreme climate event modelling

This dissertation mainly targets at precession-scale fluvial sedimentology and stratigraphy, whereas the impact of eccentricity remains poorly constrained. We have tested the influence of precession amplitude (Chapter 5), which can mimic the eccentricity's modulation, and we also have ascribed river style alternation to eccentricity that determines intensity of climatic transitions. More evidences are needed from numerical, experimental, and field analysis to clarify the role of eccentricity.

Extreme climate events are, to some degree, comparable to precession with high amplitude at eccentricity maxima (Wang et al., 2021c). Indeed, the PETM, as the most significant hyperthermal event, occurs in an eccentricity maxima (Zachos et al., 2010). How the alluvial stratigraphy reacts to this kind of extreme event awaits more evidence and examination (Foreman, 2014; Foreman et al., 2012).

6.2.4 Implications for subsurface energy exploitation

Stratigraphic organization and heterogeneity within fluvial successions are of great values for different industries such as groundwater exploitation, carbon oxide storage, geothermal energy, and hydrocarbon exploration. Short-term river style alternation has been ascribed to autogenic dynamics or geomorphic control, which fail to provide an overview over a larger temporal/stratigraphic scale. Chapter 5 presents information on the predictability of sandstone occurrence and distribution linked to orbital forcing. Specific exploration and development strategies can then be designed to target reservoirs of different fluvial origins and thus different physical properties (i.e. connectivity, N/G, heterogeneity). This would significantly enhance the exploration efficiency and reduce the risk.

Bibliography

References

H. Abdul Aziz, W. Krijgsman, F. J. Hilgen, D. S. Wilson, and J. P. Calvo. An astronomical polarity timescale for the late middle Miocene based on cyclic continental sequences: APTS for the late middle Miocene. *Journal of Geophysical Research: Solid Earth*, 108(B3), Mar. 2003. ISSN 01480227. doi: 10.1029/2002JB001818. URL http://doi.wiley.com/10.1029/2002JB001818.

H. Abdul Aziz, F. J. Hilgen, G. M. van Luijk, A. Sluijs, M. J. Kraus, J. M. Pares, and P. D. Gingerich. Astronomical climate control on paleosol stacking patterns in the upper Paleocene–lower Eocene Willwood Formation, Bighorn Basin, Wyoming. *Geology*, 36 (7):531–534, July 2008. ISSN 0091-7613. doi: 10.1130/G24734A.1. URL https://doi.org/10.1130/G24734A.1.

H. A. Abels, H. A. Aziz, W. Krijgsman, S. J. B. Smeets, and F. J. Hilgen. Long-period eccentricity control on sedimentary sequences in the continental Madrid Basin (middle Miocene, Spain). *Earth and Planetary Science Letters*, 289(1):220–231, Jan. 2010. ISSN 0012-821X. doi: 10.1016/j.epsl.2009.11.011. URL https://www.sciencedirect.com/science/article/pii/S0012821X0900658X.

H. A. Abels, W. C. Clyde, P. D. Gingerich, F. J. Hilgen, H. C. Fricke, G. J. Bowen, and L. J. Lourens. Terrestrial carbon isotope excursions and biotic change during Palaeogene hyperthermals. *Nature Geoscience*, 5(5):326–329, May 2012. ISSN 1752-0894, 1752-0908. doi: 10.1038/ngeo1427. URL http://www.nature.com/articles/ngeo1427.

H. A. Abels, M. J. Kraus, and P. D. Gingerich. Precession-scale cyclicity in the fluvial lower Eocene Willwood Formation of the Bighorn Basin, Wyoming (USA). *Sedimentology*, 60(6):1467–1483, 2013. ISSN 1365-3091. doi: https://doi.org/10.1111/sed.12039. URL https://onlinelibrary.wiley.com/doi/abs/10.1111/sed.12039. _eprint: https://onlinelibrary.wiley.com/doi/pdf/10.1111/sed.12039.

H. A. Abels, V. Lauretano, A. E. van Yperen, T. Hopman, J. C. Zachos, L. J. Lourens, P. D. Gingerich, and G. J. Bowen. Environmental impact and magnitude of paleosol carbonate carbon isotope excursions marking five early Eocene hyperthermals in the Bighorn Basin, Wyoming. *Climate of the Past*, 12(5):1151–1163, May 2016. ISSN 1814-9332. doi: 10.5194/cp-12-1151-2016. URL https://cp.copernicus.org/articles/12/1151/2016/.

A. M. Alabyan and R. S. Chalov. Types of river channel patterns and their natural controls. *Earth Surface Processes and Landforms*, 23(5):467–474, 1998. ISSN 1096-9837. doi: https://doi.org/10.1002/(SICI)1096-9837(199805)23:5<467::AID-ESP861>3.0.CO;2-T. URL https://onlinelibrary.wiley.com/doi/abs/10.1002/

%28SICI%291096-9837%28199805%2923%3A5%3C467%3A%3AAID-ESP861%3E3.0.CO%3B2-T.
_eprint: https://onlinelibrary.wiley.com/doi/pdf/10.1002/%28SICI%291096-
9837%28199805%2923%3A5%3C467%3A%3AAID-ESP861%3E3.0.CO%3B2-T.

J. Allen. Studies in fluviatile sedimentation: an exploratory quantitative model for the
architecture of avulsion-controlled alluvial suites. *Sedimentary Geology*, 21(2):129–
147, Aug. 1978. ISSN 00370738. doi: 10.1016/0037-0738(78)90002-7. URL https:
//linkinghub.elsevier.com/retrieve/pii/0037073878900027.

J. P. Allen, C. R. Fielding, M. R. Gibling, and M. C. Rygel. Recognizing products of
palaeoclimate fluctuation in the fluvial stratigraphic record: An example from the
Pennsylvanian to Lower Permian of Cape Breton Island, Nova Scotia. *Sedimentology*,
pages n/a–n/a, Dec. 2013. ISSN 00370746. doi: 10.1111/j.1365-3091.2013.12102.x. URL
http://doi.wiley.com/10.1111/j.1365-3091.2013.12102.x.

J. R. L. Allen. Studies in fluviatile sedimentation: Bars, bar-complexes and sandstone
sheets (low-sinuosity braided streams) in the brownstones (L. devonian), welsh bor-
ders. *Sedimentary Geology*, 33(4):237–293, Jan. 1983. ISSN 0037-0738. doi: 10.1016/
0037-0738(83)90076-3. URL https://www.sciencedirect.com/science/article/pii/
0037073883900763.

P. A. Allen. From landscapes into geological history. *Nature*, 451(7176):274–276, Jan. 2008.
ISSN 0028-0836, 1476-4687. doi: 10.1038/nature06586. URL http://www.nature.com/
articles/nature06586.

J. J. Armitage, T. Dunkley Jones, R. A. Duller, A. C. Whittaker, and P. A. Allen. Tempo-
ral buffering of climate-driven sediment flux cycles by transient catchment response.
Earth and Planetary Science Letters, 369-370:200–210, May 2013. ISSN 0012821X.
doi: 10.1016/j.epsl.2013.03.020. URL https://linkinghub.elsevier.com/retrieve/
pii/S0012821X13001416.

J. J. Armitage, A. C. Whittaker, M. Zakari, and B. Campforts. Numerical modelling
landscape and sediment flux response to precipitation rate change. preprint, Physi-
cal: Landscape Evolution: modelling and field studies, May 2017. URL https://esurf.
copernicus.org/preprints/esurf-2017-34/esurf-2017-34.pdf.

J. J. Armitage, A. C. Whittaker, M. Zakari, and B. Campforts. Numerical modelling of
landscape and sediment flux response to precipitation rate change. *Earth Surface Dy-
namics*, 6(1):77–99, Feb. 2018. ISSN 2196-632X. doi: 10.5194/esurf-6-77-2018. URL
https://esurf.copernicus.org/articles/6/77/2018/.

P. J. Ashworth, J. L. Best, and M. Jones. Relationship between sediment supply and
avulsion frequency in braided rivers. *Geology*, 32(1):21, 2004. ISSN 0091-7613. doi:
10.1130/G19919.1. URL https://pubs.geoscienceworld.org/geology/article/32/1/
21-24/129198.

W. Aswasereelert, S. Meyers, A. Carroll, S. Peters, M. Smith, and K. Feigl. Basin-scale cy-
clostratigraphy of the Green River Formation, Wyoming. *Geological Society of America
Bulletin*, 125(1-2):216–228, Jan. 2013. ISSN 0016-7606, 1943-2674. doi: 10.1130/B30541.

1. URL https://pubs.geoscienceworld.org/gsabulletin/article/125/1-2/216-228/125855.

S. C. Atchley, L. C. Nordt, and S. I. Dworkin. Eustatic Control on Alluvial Sequence Stratigraphy: A Possible Example from the Cretaceous-Tertiary Transition of the Tornillo Basin, Big Bend National Park, West Texas, U.S.A. *Journal of Sedimentary Research*, 74(3):391–404, May 2004. ISSN 1527-1404. doi: 10.1306/102203740391. URL https://pubs.geoscienceworld.org/jsedres/article/74/3/391-404/114147.

A. Berger, M. F. Loutre, and J. Laskar. Stability of the Astronomical Frequencies Over the Earth's History for Paleoclimate Studies. *Science*, 255(5044):560–566, Jan. 1992. ISSN 0036-8075, 1095-9203. doi: 10.1126/science.255.5044.560. URL https://www.sciencemag.org/lookup/doi/10.1126/science.255.5044.560.

R. Bettess, W. White, and HRS. Meandering and braiding of alluvial channels. *Proceedings of the Institution of Civil Engineers*, 75(3):525–538, Sept. 1983. ISSN 1753-7789. doi: 10.1680/iicep.1983.1443. URL http://www.icevirtuallibrary.com/doi/10.1680/iicep.1983.1443.

J. F. Bijkerk, J. ten Veen, G. Postma, D. Mikeš, W. van Strien, and J. de Vries. The role of climate variation in delta architecture: lessons from analogue modelling. *Basin Research*, 26(3):351–368, June 2014. ISSN 0950091X. doi: 10.1111/bre.12034. URL http://doi.wiley.com/10.1111/bre.12034.

L. Birgenheier, M. Vanden Berg, P. Plink-Bjorklund, R. Gall, E. Rosencrans, M. Rosenberg, L. Toms, and J. Morris. Climate impact on fluvial-lake system evolution, Eocene Green River Formation, Uinta Basin, Utah, USA. *GSA Bulletin*, 132, June 2019. doi: 10.1130/B31808.1.

D. L. Blackstone. Structure of the Pryor Mountains Montana. *The Journal of Geology*, 48(6):590–618, 1940. ISSN 0022-1376. URL https://www.jstor.org/stable/30058701. Publisher: University of Chicago Press.

M. D. Blum and A. Aslan. Signatures of climate vs. sea-level change within incised valley-fill successions: Quaternary examples from the Texas GULF Coast. *Sedimentary Geology*, 190(1-4):177–211, Aug. 2006. ISSN 00370738. doi: 10.1016/j.sedgeo.2006.05.024. URL https://linkinghub.elsevier.com/retrieve/pii/S0037073806001382.

M. D. Blum and T. E. Törnqvist. Fluvial responses to climate and sea-level change: a review and look forward: Fluvial responses to climate and sea-level change. *Sedimentology*, 47:2–48, Feb. 2000. ISSN 00370746. doi: 10.1046/j.1365-3091.2000.00008.x. URL http://doi.wiley.com/10.1046/j.1365-3091.2000.00008.x.

S. Bourquin, F. Guillocheau, and S. Péron. Braided rivers within an arid alluvial plain (example from the Lower Triassic, western German Basin): recognition criteria and expression of stratigraphic cycles. *Sedimentology*, 56, Dec. 2009. doi: 10.1111/j.1365-3091.2009.01078.x.

G. J. Bowen, B. J. Maibauer, M. J. Kraus, U. Röhl, T. Westerhold, A. Steimke, P. D. Gingerich, S. L. Wing, and W. C. Clyde. Two massive, rapid releases of carbon during the onset of the Palaeocene–Eocene thermal maximum. *Nature Geoscience*, 8(1):44–47, Jan. 2015. ISSN 1752-0908. doi: 10.1038/ngeo2316. URL https://www.nature.com/articles/ngeo2316. Bandiera_abtest: a Cg_type: Nature Research Journals Number: 1 Primary_atype: Research Publisher: Nature Publishing Group Subject_term: Biogeochemistry;Geochemistry;Palaeoclimate;Palaeoecology Subject_term_id: biogeochemistry;geochemistry;palaeoclimate;palaeoecology.

T. M. Bown and M. Kraus. Integration of Channel and Floodplain Suites, I. Developmental Sequence and Lateral Relations of Alluvial Paleosols. *SEPM Journal of Sedimentary Research*, Vol. 57, 1987. ISSN 1527-1404. doi: 10.1306/212F8BB1-2B24-11D7-8648000102C1865D. URL https://pubs.geoscienceworld.org/jsedres/article/57/4/587-601/97970.

T. M. Bown and M. J. Kraus. Lower Eocene alluvial paleosols (Willwood Formation, Northwest Wyoming, U.S.A.) and their significance for paleoecology, paleoclimatology, and basin analysis. *Palaeogeography, Palaeoclimatology, Palaeoecology*, 34:1–30, Jan. 1981. ISSN 00310182. doi: 10.1016/0031-0182(81)90056-0. URL https://linkinghub.elsevier.com/retrieve/pii/0031018281900560.

R. W. Bradley and J. G. Venditti. Reevaluating dune scaling relations. *Earth-Science Reviews*, 165:356–376, Feb. 2017. ISSN 0012-8252. doi: 10.1016/j.earscirev.2016.11.004. URL https://www.sciencedirect.com/science/article/pii/S0012825216301295.

J. Bridge and B. Tye. Interpreting the dimensions of ancient fluvial channel bars, channels, and channel belts from wireline-logs and cores. *AAPG Bulletin*, 84:1205–1228, Aug. 2000.

J. S. Bridge. The interaction between channel geometry, water flow, sediment transport and deposition in braided rivers. *Geological Society, London, Special Publications*, 75 (1):13–71, 1993. ISSN 0305-8719, 2041-4927. doi: 10.1144/GSL.SP.1993.075.01.02. URL http://sp.lyellcollection.org/lookup/doi/10.1144/GSL.SP.1993.075.01.02.

J. S. Bridge and M. R. Leeder. A simulation model of alluvial stratigraphy. *Sedimentology*, 26(5):617–644, Oct. 1979. ISSN 0037-0746, 1365-3091. doi: 10.1111/j.1365-3091.1979.tb00935.x. URL http://doi.wiley.com/10.1111/j.1365-3091.1979.tb00935.x.

I. Bryant, D. Carr, P. Cirilli, N. Drinkwater, D. McCormick, P. Tilke, and J. Thurmond. Use of 3D digital analogues as templates in reservoir modelling. *Petroleum Geoscience*, 6:195–201, 2000.

S. J. Buckley, J. Vallet, A. Braathen, and W. Wheeler. Oblique helicopter-based laser scanning for digital terrain modelling and visualisation of geological outcrops. *International Archives of the Photogrammetry, Remote Sensing and Spatial Information Sciences*, 37 (B4):493–498, 2008.

S. J. Buckley, K. Ringdal, N. Naumann, B. Dolva, T. H. Kurz, J. A. Howell, and T. J. Dewez. LIME: Software for 3-D visualization, interpretation, and communication of virtual geoscience models. *Geosphere*, 15(1):222–235, Feb. 2019. ISSN 1553-040X.

doi: 10.1130/GES02002.1. URL https://pubs.geoscienceworld.org/gsa/geosphere/article/15/1/222/568217/LIME-Software-for-3D-visualization-interpretation.

J. Candel, M. Kleinhans, B. Makaske, and J. Wallinga. Predicting river channel pattern based on stream power, bed material and bank strength. *Progress in Physical Geography: Earth and Environment*, 45(2):253–278, Apr. 2021. ISSN 0309-1333. doi: 10.1177/0309133320948831. URL https://doi.org/10.1177/0309133320948831. Publisher: SAGE Publications Ltd.

M. Carson. The meandering-braided river threshold: A reappraisal. *Journal of Hydrology*, 73(3-4):315–334, Aug. 1984. ISSN 00221694. doi: 10.1016/0022-1694(84)90006-4. URL https://linkinghub.elsevier.com/retrieve/pii/0022169484900064.

M. Church. Bed material transport and the morphology of alluvial river channels. *Annual Review of Earth and Planetary Sciences*, 34(1):325–354, May 2006. ISSN 0084-6597, 1545-4495. doi: 10.1146/annurev.earth.33.092203.122721. URL http://www.annualreviews.org/doi/10.1146/annurev.earth.33.092203.122721.

D. M. Cleveland, S. C. Atchley, and L. C. Nordt. Continental Sequence Stratigraphy of the Upper Triassic (Norian Rhaetian) Chinle Strata, Northern New Mexico, U.S.A.: Allocyclic and Autocyclic Origins of Paleosol-Bearing Alluvial Successions. *Journal of Sedimentary Research*, 77(11):909–924, Nov. 2007. ISSN 1527-1404. doi: 10.2110/jsr.2007.082. URL https://pubs.geoscienceworld.org/jsedres/article/77/11/909-924/145114.

W. Clyde, J. Stamatakos, and P. Gingerich. Chronology of the Wasatchian Land-Mammal Age (Early Eocene): Magnetostratigraphic Results from the McCullough Peaks Section, Northern Bighorn Basin, Wyoming. *Journal of Geology*, 102, July 1994. doi: 10.1086/629680.

W. C. Clyde and Christensen. Testing the relationship between pedofacies and avulsion using Markov analysis. *American Journal of Science*, 303(1):60–71, Jan. 2003. ISSN 0002-9599. doi: 10.2475/ajs.303.1.60. URL http://www.ajsonline.org/cgi/doi/10.2475/ajs.303.1.60.

J. M. Coleman. Brahmaputra river: Channel processes and sedimentation. *Sedimentary Geology*, 3(2):129–239, Aug. 1969. ISSN 0037-0738. doi: 10.1016/0037-0738(69)90010-4. URL https://www.sciencedirect.com/science/article/pii/0037073869900104.

L. Colombera, M. N. Shiers, and N. P. Mountney. Assessment of Backwater Controls On the Architecture of Distributary-Channel Fills In A Tide-Influenced Coastal-Plain Succession: Campanian Neslen Formation, U.S.A. *Journal of Sedimentary Research*, 86(5):476–497, May 2016. ISSN 1527-1404. doi: 10.2110/jsr.2016.33. URL https://pubs.geoscienceworld.org/jsedres/article/86/5/476-497/145531.

L. Colombera, O. J. Arévalo, and N. P. Mountney. Fluvial-system response to climate change: The Paleocene-Eocene Tremp Group, Pyrenees, Spain. *Global and Planetary Change*, 157:1–17, Oct. 2017. ISSN 09218181. doi: 10.1016/j.gloplacha.2017.08.011. URL https://linkinghub.elsevier.com/retrieve/pii/S0921818117302904.

S. D. Connell, W. Kim, C. Paola, and G. A. Smith. Fluvial Morphology and Sediment-Flux Steering of Axial-Transverse Boundaries In An Experimental Basin. *Journal of Sedimentary Research*, 82(5):310–325, June 2012. ISSN 1527-1404. doi: 10.2110/jsr.2012.27. URL https://pubs.geoscienceworld.org/jsedres/article/82/5/310-325/145367.

K. Davies-Vollum and M. Kraus. A relationship between alluvial backswamps and avulsion cycles: an example from the Willwood Formation of the Bighorn Basin, Wyoming. *Sedimentary Geology*, 140(3-4):235–249, Apr. 2001. ISSN 00370738. doi: 10.1016/S0037-0738(00)00186-X. URL https://linkinghub.elsevier.com/retrieve/pii/S003707380000186X.

K. S. Davies-Vollum and S. L. Wing. Sedimentological, Taphonomic, and Climatic Aspects of Eocene Swamp Deposits (Willwood Formation, Bighorn Basin, Wyoming). *PALAIOS*, 13(1):28, Feb. 1998. ISSN 08831351. doi: 10.2307/3515279. URL https://pubs.geoscienceworld.org/palaios/article/13/1/28-40/246708.

P. L. de Boer, J. S. J. Pragt, and A. P. Oost. Vertically persistent sedimentary facies boundaries along growth anticlines and climate-controlled sedimentation in the thrust-sheet-top South Pyrenean Tremp-Graus Foreland Basin. *Basin Research*, 3(2): 63–78, 1991. ISSN 1365-2117. doi: 10.1111/j.1365-2117.1991.tb00140.x. URL https://onlinelibrary.wiley.com/doi/abs/10.1111/j.1365-2117.1991.tb00140.x. _eprint: https://onlinelibrary.wiley.com/doi/pdf/10.1111/j.1365-2117.1991.tb00140.x.

P. DeCelles and W. Cavazza. A comparison of fluvial megafans in the Cordilleran (Upper Cretaceous) and modern Himalayan foreland basin systems. *Geological Society of America Bulletin*, page 20, 1999.

P. G. DeCelles, M. B. Gray, K. D. Ridgway, R. B. Cole, D. A. Pivnik, N. Pequera, and P. Srivastava. Controls on synorogenic alluvial-fan architecture, Beartooth Conglomerate (Palaeocene), Wyoming and Montana. *Sedimentology*, 38(4):567–590, Aug. 1991. ISSN 0037-0746, 1365-3091. doi: 10.1111/j.1365-3091.1991.tb01009.x. URL http://doi.wiley.com/10.1111/j.1365-3091.1991.tb01009.x.

T. M. Demko, B. S. Currie, and K. A. Nicoll. Regional paleoclimatic and stratigraphic implications of paleosols and fluvial/overbank architecture in the Morrison Formation (Upper Jurassic), Western Interior, USA. *Sedimentary Geology*, 167(3-4):115–135, May 2004. ISSN 00370738. doi: 10.1016/j.sedgeo.2004.01.003. URL https://linkinghub.elsevier.com/retrieve/pii/S0037073804000065.

A. R. D'Ambrosia, W. C. Clyde, H. C. Fricke, P. D. Gingerich, and H. A. Abels. Repetitive mammalian dwarfing during ancient greenhouse warming events. *Science Advances*, 3(3):e1601430, Mar. 2017. ISSN 2375-2548. doi: 10.1126/sciadv.1601430. URL https://advances.sciencemag.org/lookup/doi/10.1126/sciadv.1601430.

A. Eltner, A. Kaiser, C. Castillo, G. Rock, F. Neugirg, and A. Abellan. Image-based surface reconstruction in geomorphometry - merits, limits and developments. *Earth Surface Dynamics*, 4:359–389, May 2016. doi: 10.5194/esurf-4-359-2016.

H. D. Enge, S. J. Buckley, A. Rotevatn, and J. A. Howell. From outcrop to reservoir simulation model: Workflow and procedures. *Geosphere*, 3(6):469, 2007. ISSN 1553-040X. doi: 10.1130/GES00099.1. URL https://pubs.geoscienceworld.org/geosphere/article/3/6/469-490/31177.

W.-J. Feng, C.-M. Zhang, T.-J. Yin, Y.-S. Yin, J.-L. Liu, R. Zhu, Q.-H. Xu, and Z. Chen. Sedimentary characteristics and internal architecture of a river-dominated delta controlled by autogenic process: implications from a flume tank experiment. *Petroleum Science*, 16 (6):1237–1254, Dec. 2019. ISSN 1672-5107, 1995-8226. doi: 10.1007/s12182-019-00389-x. URL http://link.springer.com/10.1007/s12182-019-00389-x.

C. Fielding and J. Webb. Facies and cyclicity of the Late Permian Bainmedart Coal Measures in the Northern Prince Charles Mountains, MacRobertson Land, Antarctica. *Sedimentology*, 43:295–322, 1996. doi: 10.1046/j.1365-3091.1996.d01-6.x.

C. R. Fielding, J. Alexander, and J. P. Allen. The role of discharge variability in the formation and preservation of alluvial sediment bodies. *Sedimentary Geology*, 365:1–20, Mar. 2018. ISSN 00370738. doi: 10.1016/j.sedgeo.2017.12.022. URL https://linkinghub.elsevier.com/retrieve/pii/S0037073817302981.

G. Fischer, F. N. Tubiello, H. van Velthuizen, and D. A. Wiberg. Climate change impacts on irrigation water requirements: Effects of mitigation, 1990–2080. *Technological Forecasting and Social Change*, 74(7):1083–1107, Sept. 2007. ISSN 00401625. doi: 10.1016/j.techfore.2006.05.021. URL https://linkinghub.elsevier.com/retrieve/pii/S0040162506001429.

R. M. Foose, D. U. Wise, and G. S. Garbarini. Structural Geology of the Beartooth Mountains, Montana and Wyoming. *Geological Society of America Bulletin*, 72(8):1143, 1961. ISSN 0016-7606. doi: 10.1130/0016-7606(1961)72[1143:SGOTBM]2.0.CO;2. URL https://pubs.geoscienceworld.org/gsabulletin/article/72/8/1143-1172/5337.

B. Z. Foreman. Climate-driven generation of a fluvial sheet sand body at the Paleocene-Eocene boundary in north-west Wyoming (USA). *Basin Research*, 26(2):225–241, Apr. 2014. ISSN 0950091X. doi: 10.1111/bre.12027. URL http://doi.wiley.com/10.1111/bre.12027.

B. Z. Foreman and K. M. Straub. Autogenic geomorphic processes determine the resolution and fidelity of terrestrial paleoclimate records. *Science Advances*, 3(9):e1700683, Sept. 2017. ISSN 2375-2548. doi: 10.1126/sciadv.1700683. URL https://advances.sciencemag.org/lookup/doi/10.1126/sciadv.1700683.

B. Z. Foreman, P. L. Heller, and M. T. Clementz. Fluvial response to abrupt global warming at the Palaeocene/Eocene boundary. *Nature*, 491(7422):92–95, Nov. 2012. ISSN 1476-4687. doi: 10.1038/nature11513. URL https://www.nature.com/articles/nature11513. Number: 7422 Publisher: Nature Publishing Group.

A. Forzoni, J. E. Storms, A. C. Whittaker, and G. de Jager. Delayed delivery from the sediment factory: modeling the impact of catchment response time to tectonics on sediment flux and fluvio-deltaic stratigraphy: MODELING DELAYED DELIVERY FROM THE

SEDIMENT FACTORY. *Earth Surface Processes and Landforms*, 39(5):689–704, Apr. 2014. ISSN 01979337. doi: 10.1002/esp.3538. URL http://doi.wiley.com/10.1002/esp.3538.

M. Ghinassi and A. Ielpi. Morphodynamics and facies architecture of streamflow-dominated, sand-rich alluvial fans, Pleistocene Upper Valdarno Basin, Italy. *Geological Society, London, Special Publications*, 440(1):175–200, 2018. ISSN 0305-8719, 2041-4927. doi: 10.1144/SP440.1. URL http://sp.lyellcollection.org/lookup/doi/10.1144/SP440.1.

M. R. Gibling. Width and Thickness of Fluvial Channel Bodies and Valley Fills in the Geological Record: A Literature Compilation and Classification. *Journal of Sedimentary Research*, 76(5):731–770, May 2006. ISSN 1527-1404. doi: 10.2110/jsr.2006.060. URL https://pubs.geoscienceworld.org/jsedres/article/76/5/731-770/145064.

P. Giles, B. Whitehouse, and E. Karymbalis. Interactions between alluvial fans and axial rivers in Yukon, Canada and Alaska, USA. *Geological Society, London, Special Publications*, 440, Feb. 2016. doi: 10.1144/SP440.3.

P. Gingerich. Paleocene-Eocene faunal zones and a preliminary analysis of Laramide structural deformation in the Clark's Fork Basin, Wyoming. *Geology of the Bighorn Basin*, 34, Jan. 1983.

P. Gingerich and V. Palasiatica. Mammalian Faunal Succession Through The Paleocene–Eocene Thermal Maximum (PETM) In Western North America. *Vertebrata Palasiatica*, Oct. 2010.

V. Godard, G. E. Tucker, G. Burch Fisher, D. W. Burbank, and B. Bookhagen. Frequency-dependent landscape response to climatic forcing: landscapes and climate oscillations. *Geophysical Research Letters*, 40(5):859–863, Mar. 2013. ISSN 00948276. doi: 10.1002/grl.50253. URL http://doi.wiley.com/10.1002/grl.50253.

E. A. Hajek and K. M. Straub. Autogenic Sedimentation in Clastic Stratigraphy. *Annual Review of Earth and Planetary Sciences*, 45(1):681–709, Aug. 2017. ISSN 0084-6597, 1545-4495. doi: 10.1146/annurev-earth-063016-015935. URL http://www.annualreviews.org/doi/10.1146/annurev-earth-063016-015935.

E. A. Hajek and M. A. Wolinsky. Simplified process modeling of river avulsion and alluvial architecture: Connecting models and field data. *Sedimentary Geology*, 257-260:1–30, June 2012. ISSN 00370738. doi: 10.1016/j.sedgeo.2011.09.005. URL https://linkinghub.elsevier.com/retrieve/pii/S0037073811002260.

E. A. Hajek, P. L. Heller, and B. A. Sheets. Significance of channel-belt clustering in alluvial basins. *Geology*, 38(6):535–538, June 2010. ISSN 1943-2682, 0091-7613. doi: 10.1130/G30783.1. URL http://pubs.geoscienceworld.org/geology/article/38/6/535/130307/Significance-of-channelbelt-clustering-in-alluvial.

E. A. Hajek, P. L. Heller, and E. L. Schur. Field test of autogenic control on alluvial stratigraphy (Ferris Formation, Upper Cretaceous-Paleogene, Wyoming). *Geological*

Society of America Bulletin, 124(11-12):1898–1912, Nov. 2012. ISSN 0016-7606, 1943-2674. doi: 10.1130/B30526.1. URL https://pubs.geoscienceworld.org/gsabulletin/article/124/11-12/1898-1912/125812.

O. Hammer, D. A. T. Harper, and P. D. Ryan. PAST: Paleontological Statistics Software Package for Education and Data Analysis. *Palaeontologia Electronica*, 4(1):9, June 2001.

G. J. Hampson, M. Royhan Gani, H. Sahoo, A. Rittersbacher, N. Irfan, A. Ranson, T. O. Jewell, N. D. S. Gani, J. A. Howell, S. J. Buckley, and B. Bracken. Controls on large-scale patterns of fluvial sandbody distribution in alluvial to coastal plain strata: Upper Cretaceous Blackhawk Formation, Wasatch Plateau, Central Utah, USA. *Sedimentology*, 59(7): 2226–2258, Dec. 2012. ISSN 0037-0746, 1365-3091. doi: 10.1111/j.1365-3091.2012.01342.x. URL https://onlinelibrary.wiley.com/doi/abs/10.1111/j.1365-3091.2012.01342.x.

G. J. Hampson, T. O. Jewell, N. Irfan, M. R. Gani, and B. Bracken. Modest Change In Fluvial Style With Varying Accommodation In Regressive Alluvial-To-Coastal-Plain Wedge: Upper Cretaceous Blackhawk Formation, Wasatch Plateau, Central Utah, U.S.A. *Journal of Sedimentary Research*, 83(2):145–169, Feb. 2013. ISSN 1527-1404. doi: 10.2110/jsr.2013.8. URL https://pubs.geoscienceworld.org/jsedres/article/83/2/145-169/330482.

J. D. Hays, J. Imbrie, and N. J. Shackleton. Variations in the Earth's Orbit: Pacemaker of the Ice Ages. 194:13, 1976.

F. J. Hilgen. Astronomical calibration of Gauss to Matuyama sapropels in the Mediterranean and implication for the Geomagnetic Polarity Time Scale. *Earth and Planetary Science Letters*, 104(2):226–244, June 1991a. ISSN 0012-821X. doi: 10.1016/0012-821X(91)90206-W. URL https://www.sciencedirect.com/science/article/pii/0012821X9190206W.

F. J. Hilgen. Extension of the astronomically calibrated (polarity) time scale to the Miocene/Pliocene boundary. *Earth and Planetary Science Letters*, 107(2):349–368, Nov. 1991b. ISSN 0012-821X. doi: 10.1016/0012-821X(91)90082-S. URL https://www.sciencedirect.com/science/article/pii/0012821X9190082S.

F. J. Hilgen, L. A. Hinnov, H. Abdul Aziz, H. A. Abels, S. Batenburg, J. H. C. Bosmans, B. de Boer, S. K. Hüsing, K. F. Kuiper, L. J. Lourens, T. Rivera, E. Tuenter, R. S. W. Van de Wal, J.-F. Wotzlaw, and C. Zeeden. Stratigraphic continuity and fragmentary sedimentation: the success of cyclostratigraphy as part of integrated stratigraphy. *Geological Society, London, Special Publications*, 404(1):157–197, 2015. ISSN 0305-8719, 2041-4927. doi: 10.1144/SP404.12. URL http://sp.lyellcollection.org/lookup/doi/10.1144/SP404.12.

J. Holbrook, R. W. Scott, and F. E. Oboh-Ikuenobe. Base-Level Buffers and Buttresses: A Model for Upstream Versus Downstream Control on Fluvial Geometry and Architecture Within Sequences. *Journal of Sedimentary Research*, 76(1):162–174, Jan. 2006. ISSN 1527-1404. doi: 10.2110/jsr.2005.10. URL https://pubs.geoscienceworld.org/jsedres/article/76/1/162-174/145020.

J. A. Howell, A. W. Martinius, and T. R. Good. The application of outcrop analogues in geological modelling: a review, present status and future outlook. *Geological Society, London, Special Publications*, 387(1):1–25, 2014. ISSN 0305-8719, 2041-4927. doi: 10. 1144/SP387.12. URL http://sp.lyellcollection.org/lookup/doi/10.1144/SP387.12.

C. Huang and L. Hinnov. Astronomically forced climate evolution in a saline lake record of the middle Eocene to Oligocene, Jianghan Basin, China. *Earth and Planetary Science Letters*, 528:115846, Dec. 2019. ISSN 0012821X. doi: 10.1016/j.epsl.2019.115846. URL https://linkinghub.elsevier.com/retrieve/pii/S0012821X19305382.

M. A. Jensen and G. K. Pedersen. Architecture of vertically stacked fluvial deposits, Atane Formation, Cretaceous, Nuussuaq, central West Greenland: Architecture of stacked fluvial deposits. *Sedimentology*, pages no–no, May 2010. ISSN 00370746, 13653091. doi: 10.1111/j.1365-3091.2010.01146.x. URL http://doi.wiley.com/10.1111/j.1365-3091.2010.01146.x.

D. J. Jerolmack and C. Paola. Complexity in a cellular model of river avulsion. *Geomorphology*, 91(3-4):259–270, Nov. 2007. ISSN 0169555X. doi: 10.1016/j.geomorph.2007.04.022. URL https://linkinghub.elsevier.com/retrieve/pii/S0169555X07003807.

D. J. Jerolmack and C. Paola. Shredding of environmental signals by sediment transport. *Geophysical Research Letters*, 37(19):n/a–n/a, Oct. 2010. ISSN 00948276. doi: 10.1029/ 2010GL044638. URL http://doi.wiley.com/10.1029/2010GL044638.

D. Karssenberg and J. S. Bridge. A three-dimensional numerical model of sediment transport, erosion and deposition within a network of channel belts, floodplain and hill slope: extrinsic and intrinsic controls on floodplain dynamics and alluvial architecture. *Sedimentology*, 55(6):1717–1745, Dec. 2008. ISSN 00370746, 13653091. doi: 10.1111/j.1365-3091.2008.00965.x. URL http://doi.wiley.com/10.1111/j.1365-3091.2008.00965.x.

C. Kasse, W. Z. Hoek, S. J. P. Bohncke, M. Konert, J. W. H. Weijers, M. L. Cassee, and R. M. V. D. Zee. Late Glacial fluvial response of the Niers-Rhine (western Germany) to climate and vegetation change. *Journal of Quaternary Science*, 20(4):377–394, 2005. ISSN 1099-1417. doi: 10.1002/jqs.923. URL https://onlinelibrary.wiley.com/doi/abs/10.1002/jqs.923. _eprint: https://onlinelibrary.wiley.com/doi/pdf/10.1002/jqs.923.

D. B. Kemp. Optimizing significance testing of astronomical forcing in cyclostratigraphy: Testing of Astronomical Forcing. *Paleoceanography*, 31(12):1516–1531, Dec. 2016. ISSN 08838305. doi: 10.1002/2016PA002963. URL http://doi.wiley.com/10.1002/2016PA002963.

J. F. Kennedy. The Formation of Sediment Ripples, Dunes, and Antidunes. *Annual Review of Fluid Mechanics*, 1(1):147–168, Jan. 1969. ISSN 0066-4189, 1545-4479. doi: 10. 1146/annurev.fl.01.010169.001051. URL http://www.annualreviews.org/doi/10.1146/annurev.fl.01.010169.001051.

W. Kim, S. D. Connell, E. Steel, G. A. Smith, and C. Paola. Mass-balance control on the interaction of axial and transverse channel systems. *Geology*, 39

(7):611–614, July 2011. ISSN 1943-2682, 0091-7613. doi: 10.1130/G31896. 1. URL http://pubs.geoscienceworld.org/geology/article/39/7/611/130573/ Massbalance-control-on-the-interaction-of-axial.

P. Koch, J. C. Zachost, and P. D. Gingericht. Correlation between isotope records in marine and continental carbon reservoirs near the Palaeocene/Eocene boundary. 358:4, 1992.

I. J. Kocken, I. A. Müller, and M. Ziegler. Optimizing the Use of Carbonate Standards to Minimize Uncertainties in Clumped Isotope Data. *Geochemistry, Geophysics, Geosystems*, 20(11):5565–5577, 2019. ISSN 1525-2027. doi: https://doi.org/10.1029/2019GC008545. URL https://agupubs.onlinelibrary.wiley.com/doi/abs/10.1029/2019GC008545. _eprint: https://agupubs.onlinelibrary.wiley.com/doi/pdf/10.1029/2019GC008545.

M. Kraus and S. Hasiotis. Significance of Different Modes of Rhizolith Preservation to Interpreting Paleoenvironmental and Paleohydrologic Settings: Examples from Paleogene Paleosols, Bighorn Basin, Wyoming, U.S.A. *Journal of Sedimentary Research*, 76: 633–646, Apr. 2006. doi: 10.2110/jsr.2006.052.

M. Kraus and L. Middleton. Contrasting architecture of two alluvial suites in different structural settings. pages 253–262. Jan. 1987. ISBN 978-0-918985-67-5. doi: 10.2110/pec. 87.39.0253.

M. J. Kraus. Sedimentology and tectonic setting of Early Tertiary quartzite conglomerates, northwest Wyoming. *Canadian Society of Petroleum Geologists Memoir*, 10(10):203–216, 1984.

M. J. Kraus. Paleosols in clastic sedimentary rocks: their geologic applications. *Earth-Science Reviews*, 47(1-2):41–70, July 1999. ISSN 00128252. doi: 10.1016/S0012-8252(99) 00026-4. URL https://linkinghub.elsevier.com/retrieve/pii/S0012825299000264.

M. J. Kraus. Basin-Scale changes in floodplain paleosols: implications for interpreting alluvial architecture. *Journal of Sedimentary Research*, 72(4):500–509, July 2002. ISSN 1527-1404. doi: 10.1306/121701720500. URL https://pubs.geoscienceworld.org/jsedres/ article/72/4/500-509/114086.

M. J. Kraus and A. Aslan. Eocene hydromorphic paleosols: significance for interpreting ancient floodplain processes. *SEPM Journal of Sedimentary Research*, Vol. 63, 1993. ISSN 1527-1404. doi: 10.1306/D4267B22-2B26-11D7-8648000102C1865D. URL https://pubs. geoscienceworld.org/jsedres/article/63/3/453-463/98464.

M. J. Kraus and K. S. Davies-Vollum. Mudrock-dominated fills formed in avulsion splay channels: examples from the Willwood Formation, Wyoming. *Sedimentology*, 51(5): 1127–1144, 2004. ISSN 1365-3091. doi: 10.1111/j.1365-3091.2004.00664.x. URL https: //onlinelibrary.wiley.com/doi/abs/10.1111/j.1365-3091.2004.00664.x. _eprint: https://onlinelibrary.wiley.com/doi/pdf/10.1111/j.1365-3091.2004.00664.x.

M. J. Kraus and B. Gwinn. Facies and facies architecture of Paleogene floodplain deposits, Willwood Formation, Bighorn Basin, Wyoming, USA. *Sedimentary Geology*, 114(1-4): 33–54, Dec. 1997. ISSN 00370738. doi: 10.1016/S0037-0738(97)00083-3. URL https: //linkinghub.elsevier.com/retrieve/pii/S0037073897000833.

M. J. Kraus, D. T. Woody, J. J. Smith, and V. Dukic. Alluvial response to the Paleocene–Eocene Thermal Maximum climatic event, Polecat Bench, Wyoming (U.S.A.). page 16, 2015.

K. F. Kuiper, A. Deino, F. J. Hilgen, W. Krijgsman, P. R. Renne, and J. R. Wijbrans. Synchronizing Rock Clocks of Earth History. *Science*, 320(5875):500–504, Apr. 2008. ISSN 0036-8075, 1095-9203. doi: 10.1126/science.1154339. URL https://www.sciencemag.org/lookup/doi/10.1126/science.1154339.

J. Laskar, A. Fienga, M. Gastineau, and H. Manche. La2010: a new orbital solution for the long-term motion of the Earth. *Astronomy & Astrophysics*, 532:A89, Aug. 2011. ISSN 0004-6361, 1432-0746. doi: 10.1051/0004-6361/201116836. URL http://www.aanda.org/10.1051/0004-6361/201116836.

V. Lauretano, J. C. Zachos, and L. J. Lourens. Orbitally Paced Carbon and Deep-Sea Temperature Changes at the Peak of the Early Eocene Climatic Optimum. *Paleoceanography and Paleoclimatology*, 33(10):1050–1065, 2018. ISSN 2572-4525. doi: 10.1029/2018PA003422. URL https://agupubs.onlinelibrary.wiley.com/doi/abs/10.1029/2018PA003422. _eprint: https://agupubs.onlinelibrary.wiley.com/doi/pdf/10.1029/2018PA003422.

S. F. Leclair and J. S. Bridge. Quantitative interpretation of sedimentary structures formed by river dunes. page 4, 2001.

D. S. Leigh. Terminal Pleistocene braided to meandering transition in rivers of the Southeastern USA. *CATENA*, 66(1):155–160, May 2006. ISSN 0341-8162. doi: 10.1016/j.catena.2005.11.008. URL https://www.sciencedirect.com/science/article/pii/S0341816205001943.

L. B. Leopold and M. G. Wolman. River channel patterns: Braided, meandering, and straight. Professional Paper 282-B, 1957. Series: Professional Paper.

K. Littler. A high-resolution benthic stable-isotope record for the South Atlantic: Implications for orbital-scale changes in Late Paleocene–Early Eocene climate and carbon cycling. *Earth and Planetary Science Letters*, page 13, 2014.

L. J. Lourens, A. Sluijs, D. Kroon, J. C. Zachos, E. Thomas, U. Röhl, J. Bowles, and I. Raffi. Astronomical pacing of late Palaeocene to early Eocene global warming events. *Nature*, 435(7045):1083–1087, June 2005. ISSN 1476-4687. doi: 10.1038/nature03814. URL https://www.nature.com/articles/nature03814. Number: 7045 Publisher: Nature Publishing Group.

S. D. Mackey and J. S. Bridge. Three-Dimensional Model of Alluvial Stratigraphy: Theory and Application. page 25, 1995.

M. O. Manna, C. M. d. S. Scherer, M. B. Bállico, A. D. d. Reis, L. V. Moraes, L. A. B. Ferrari, H. B. Roisenberg, and V. G. d. Oliveira. Changes in fluvial architecture induced by discharge variability, Jaicós Formation (Silurian-Devonian), Parnaíba Basin, Brazil. *Sedimentary Geology*, 420:105924, July 2021. ISSN 0037-0738. doi: 10.1016/j.sedgeo.2021.105924. URL https://www.sciencedirect.com/science/article/pii/S0037073821000762.

E. F. Mcbride. A Classification of Common Sandstones. *SEPM Journal of Sedimentary Research*, Vol. 33, 1963. ISSN 1527-1404. doi: 10.1306/74D70EE8-2B21-11D7-8648000102C1865D. URL https://pubs.geoscienceworld.org/jsedres/article/33/3/664-669/95680.

A. Miall. *Fluvial Depositional Systems*. Springer Geology. Springer International Publishing, Cham, 2014. ISBN 978-3-319-00665-9 978-3-319-00666-6. doi: 10.1007/978-3-319-00666-6. URL http://link.springer.com/10.1007/978-3-319-00666-6.

A. D. Miall. Architectural-element analysis: A new method of facies analysis applied to fluvial deposits. *Earth-Science Reviews*, 22(4):261–308, Dec. 1985. ISSN 0012-8252. doi: 10.1016/0012-8252(85)90001-7. URL https://www.sciencedirect.com/science/article/pii/0012825285900017.

A. D. Miall. Reconstructing Fluvial Macroform Architecture from Two-Dimensional Outcrops: Examples from the Castlegate Sandstone, Book Cliffs, Utah. *SEPM Journal of Sedimentary Research*, Vol. 64B, 1994. ISSN 1527-1404. doi: 10.1306/D4267F78-2B26-11D7-8648000102C1865D. URL https://pubs.geoscienceworld.org/jsedres/article/64/2b/146-158/98538.

A. D. Miall, J. M. Holbrook, and J. P. Bhattacharya. The Stratigraphy Machine. *Journal of Sedimentary Research*, 91(6):595–610, June 2021. ISSN 1527-1404. doi: 10.2110/jsr.2020.143. URL https://pubs.geoscienceworld.org/jsedres/article/91/6/595/600848/The-Stratigraphy-Machine.

D. Mohrig, P. L. Heller, C. Paola, and W. J. Lyons. Interpreting avulsion process from ancient alluvial sequences: Guadalope-Matarranya system (northern Spain) and Wasatch Formation (western Colorado). *Geological Society of America Bulletin*, page 17, 2000.

T. Muto, R. Steel, and J. Swenson. Autostratigraphy: A Framework Norm for Genetic Stratigraphy. *Journal of Sedimentary Research*, 77:2–12, Jan. 2007. doi: 10.2110/jsr.2007.005.

Métivier and Gaudemer. Stability of output fluxes of large rivers in South and East Asia during the last 2 million years: implications on floodplain processes: River stability, SE Asia. *Basin Research*, 11(4):293–303, Dec. 1999. ISSN 0950091X. doi: 10.1046/j.1365-2117.1999.00101.x. URL http://doi.wiley.com/10.1046/j.1365-2117.1999.00101.x.

J. W. Neasham and C. F. Vondra. Stratigraphy and Petrology of the Lower Eocene Willwood Formation, Bighorn Basin, Wyoming. *Geological Society of America Bulletin*, 83(7):2167, 1972. ISSN 0016-7606. doi: 10.1130/0016-7606(1972)83[2167:SAPOTL]2.0.CO;2. URL https://pubs.geoscienceworld.org/gsabulletin/article/83/7/2167-2180/7632.

J. A. Nittrouer, J. Shaw, M. P. Lamb, and D. Mohrig. Spatial and temporal trends for water-flow velocity and bed-material sediment transport in the lower Mississippi River. *Geological Society of America Bulletin*, 124(3-4):400–414, Mar. 2012. ISSN 0016-7606, 1943-2674. doi: 10.1130/B30497.1. URL https://pubs.geoscienceworld.org/gsabulletin/article/124/3-4/400-414/125770.

L. Noorbergen, H. Abels, F. Hilgen, B. Robson, E. Jong, M. Dekkers, W. Krijgsman, J. Smit, M. Collinson, and K. Kuiper. Conceptual models for short-eccentricity-scale climate control on peat formation in a lower Palaeocene fluvial system, north-eastern Montana (USA). *Sedimentology*, Jan. 2018. doi: 10.1111/sed.12405.

L. J. Noorbergen, A. Turtu, K. F. Kuiper, C. Kasse, S. v. Ginneken, M. J. Dekkers, W. Krijgsman, H. A. Abels, and F. J. Hilgen. Long-eccentricity regulated climate control on fluvial incision and aggradation in the Palaeocene of north-eastern Montana (USA). *Sedimentology*, 67(5):2529–2560, 2020. ISSN 1365-3091. doi: https://doi.org/10.1111/sed.12710. URL https://onlinelibrary.wiley.com/doi/abs/10.1111/sed.12710. _eprint: https://onlinelibrary.wiley.com/doi/pdf/10.1111/sed.12710.

H. Olsen. Astronomical forcing of meandering river behaviour: Milankovitch cycles in Devonian of East Greenland. *Palaeogeography, Palaeoclimatology, Palaeoecology*, 79(1-2):99–115, July 1990. ISSN 00310182. doi: 10.1016/0031-0182(90)90107-I. URL https://linkinghub.elsevier.com/retrieve/pii/003101829090107I.

H. Olsen. Orbital forcing on continental depositional systems - lacustrine and fluvial cyclicity in the Devonian of East Greenland. *Orbital forcing and cyclic sequences*, 19:429–438, Apr. 1994. ISSN 9781444304039. doi: 10.1002/9781444304039.ch26.

P. E. Olsen, D. V. Kent, B. Cornet, W. K. Witte, and R. W. Schlische. High-resolution stratigraphy of the Newark rift basin (early Mesozoic, eastern North America). *Geological Society of America Bulletin*, page 38, 1996.

A. Owen, A. Ebinghaus, A. J. Hartley, M. G. M. Santos, and G. S. Weissmann. Multi-scale classification of fluvial architecture: An example from the Palaeocene–Eocene Bighorn Basin, Wyoming. *Sedimentology*, 64(6):1572–1596, 2017. ISSN 1365-3091. doi: https://doi.org/10.1111/sed.12364. URL https://onlinelibrary.wiley.com/doi/abs/10.1111/sed.12364. _eprint: https://onlinelibrary.wiley.com/doi/pdf/10.1111/sed.12364.

A. Owen, A. J. Hartley, A. Ebinghaus, G. S. Weissmann, and M. G. M. Santos. Basin-scale predictive models of alluvial architecture: Constraints from the Palaeocene–Eocene, Bighorn Basin, Wyoming, USA. *Sedimentology*, 66 (2):736–763, 2019. ISSN 1365-3091. doi: https://doi.org/10.1111/sed.12515. URL https://onlinelibrary.wiley.com/doi/abs/10.1111/sed.12515. _eprint: https://onlinelibrary.wiley.com/doi/pdf/10.1111/sed.12515.

C. Paola, K. Straub, D. Mohrig, and L. Reinhardt. The "unreasonable effectiveness" of stratigraphic and geomorphic experiments. *Earth-Science Reviews*, 97(1-4):1–43, Dec. 2009. ISSN 00128252. doi: 10.1016/j.earscirev.2009.05.003. URL https://linkinghub.elsevier.com/retrieve/pii/S001282520900083X.

J. M. Paredes, N. Foix, J. O. Allard, M. N. Valle, and S. R. Giordano. Alluvial architecture and fluvial style variations determined from outcrops: example from the Cerro Ballena Anticline (Bajo Barreal Formation) of the Golfo San Jorge Basin. page 25, 2016.

S. Peirce, P. Ashmore, and P. Leduc. The variability in the morphological active width: Results from physical models of gravel-bed braided rivers. *Earth Surface Processes and Landforms*, 43(11):2371–2383, 2018. ISSN 1096-9837. doi: 10.1002/esp. 4400. URL https://onlinelibrary.wiley.com/doi/abs/10.1002/esp.4400. _eprint: https://onlinelibrary.wiley.com/doi/pdf/10.1002/esp.4400.

H. Posamentier, R. Davies, J. Cartwright, and L. Wood. Seismic geomorphology - An overview. *Geological Society, London, Special Publications*, 277:1–14, Jan. 2007. doi: 10. 1144/GSL.SP.2007.277.01.01.

E. J. Powell, W. Kim, and T. Muto. Varying discharge controls on timescales of autogenic storage and release processes in fluvio-deltaic environments: Tank experiments: controls on autogenic timescales. *Journal of Geophysical Research: Earth Surface*, 117(F2):n/a–n/a, June 2012. ISSN 01480227. doi: 10.1029/2011JF002097. URL http://doi.wiley.com/10.1029/2011JF002097.

W. A. Pryor. Cretaceous Sedimentation in Upper Mississippi Embayment. *AAPG Bulletin*, 44, 1960. ISSN 0149-1423. doi: 10.1306/ 0BDA61C4-16BD-11D7-8645000102C1865D. URL http://search.datapages.com/ data/doi/10.1306/0BDA61C4-16BD-11D7-8645000102C1865D.

M. Pyrcz and C. Deutsch. The whole story on the hole effect. *Geostatistical Association of Australasia, Newsletter*, 18, Jan. 2003.

M. Pyrcz and C. V. Deutsch. *Geostatistical reservoir modeling*. New York, New York : Oxford University Press, Oxford, second edition edition, 2014. ISBN 978-0-19-973144-2.

B. W. Romans, S. Castelltort, J. A. Covault, A. Fildani, and J. Walsh. Environmental signal propagation in sedimentary systems across timescales. *Earth-Science Reviews*, 153:7–29, Feb. 2016. ISSN 00128252. doi: 10.1016/j.earscirev.2015.07.012. URL https://linkinghub.elsevier.com/retrieve/pii/S0012825215300222.

M. Rossignol-Strick. African monsoons, an immediate climate response to orbital insolation. *Nature*, 304(5921):46–49, July 1983. ISSN 0028-0836, 1476-4687. doi: 10.1038/ 304046a0. URL http://www.nature.com/articles/304046a0.

P. M. Sadler. Sediment Accumulation Rates and the Completeness of Stratigraphic Sections. *The Journal of Geology*, 89(5):569–584, 1981. ISSN 0022-1376. URL https://www.jstor. org/stable/30062397. Publisher: The University of Chicago Press.

S. A. Schumm. Patterns of alluvial rivers. page 24, 1985.

C. Scotese, H. Song, B. Mills, and D. Meer. Phanerozoic Paleotemperatures: The Earth's Changing Climate during the Last 540 million years. *Earth-Science Reviews*, 215, Jan. 2021. doi: 10.1016/j.earscirev.2021.103503.

K. W. Shanley and P. J. McCabe. Perspectives on the Sequence Stratigraphy of Continental Strata. *Sequence Stratigraphy*, page 25, 1994.

B. A. Sheets, T. A. Hickson, and C. Paola. Assembling the stratigraphic record: depositional patterns and time-scales in an experimental alluvial basin. *Basin Research*, 14(3):287–301, 2002. ISSN 1365-2117. doi: https://doi.org/10.1046/j.1365-2117.2002.00185.x. URL https://onlinelibrary.wiley.com/doi/abs/10.1046/j.1365-2117.2002.00185.x. _eprint: https://onlinelibrary.wiley.com/doi/pdf/10.1046/j.1365-2117.2002.00185.x.

G. Skirrow, R. Smedley, R. Chiverrell, and J. Hooke. Planform change of the Río Chubut (~42°S, ~70°W, Argentina) in response to climate drivers in the southern Andes. *Geomorphology*, 393:107924, Nov. 2021. ISSN 0169555X. doi: 10.1016/j.geomorph.2021.107924. URL https://linkinghub.elsevier.com/retrieve/pii/S0169555X21003329.

R. Slingerland and N. D. Smith. River avulsions and their deposits. *Annual Review of Earth and Planetary Sciences*, 32(1):257–285, May 2004. ISSN 0084-6597, 1545-4495. doi: 10.1146/annurev.earth.32.101802.120201. URL http://www.annualreviews.org/doi/10.1146/annurev.earth.32.101802.120201.

H. Smedes and H. Prostka. Stratigraphic framework of the Absaroka Volcanic Supergroup in the Yellowstone National Park region. Report 729C, 1972. URL http://pubs.er.usgs.gov/publication/pp729C. Edition: -.

M. E. Smith, A. R. Carroll, J. J. Scott, and B. S. Singer. Early Eocene carbon isotope excursions and landscape destabilization at eccentricity minima: Green River Formation of Wyoming. *Earth and Planetary Science Letters*, 403:393–406, Oct. 2014. ISSN 0012821X. doi: 10.1016/j.epsl.2014.06.024. URL https://linkinghub.elsevier.com/retrieve/pii/S0012821X14004099.

L. Stap, A. Sluijs, E. Thomas, and L. Lourens. Patterns and magnitude of deep sea carbonate dissolution during Eocene Thermal Maximum 2 and H2, Walvis Ridge, southeastern Atlantic Ocean. *Paleoceanography*, 24(1), 2009. ISSN 1944-9186. doi: https://doi.org/10.1029/2008PA001655. URL https://agupubs.onlinelibrary.wiley.com/doi/abs/10.1029/2008PA001655. _eprint: https://agupubs.onlinelibrary.wiley.com/doi/pdf/10.1029/2008PA001655.

E. Stouthamer and H. J. Berendsen. Avulsion: The relative roles of autogenic and allogenic processes. *Sedimentary Geology*, 198(3-4):309–325, June 2007. ISSN 00370738. doi: 10.1016/j.sedgeo.2007.01.017. URL https://linkinghub.elsevier.com/retrieve/pii/S0037073807000152.

K. M. Straub and C. R. Esposito. Influence of water and sediment supply on the stratigraphic record of alluvial fans and deltas: Process controls on stratigraphic completeness. *Journal of Geophysical Research: Earth Surface*, 118(2):625–637, 2013. ISSN 2169-9011. doi: 10.1002/jgrf.20061. URL https://agupubs.onlinelibrary.wiley.com/doi/abs/10.1002/jgrf.20061. _eprint: https://agupubs.onlinelibrary.wiley.com/doi/pdf/10.1002/jgrf.20061.

K. M. Straub and B. Z. Foreman. Geomorphic stasis and spatiotemporal scales of stratigraphic completeness. *Geology*, 46(4):311–314, Apr. 2018. ISSN 0091-7613. doi: 10.1130/G40045.1. URL https://pubs.geoscienceworld.org/gsa/geology/article/46/4/311/527275/Geomorphic-stasis-and-spatiotemporal-scales-of.

K. M. Straub and D. R. Pyles. Quantifying the Hierarchical Organization of Compensation In Submarine Fans Using Surface Statistics. *Journal of Sedimentary Research*, 82(11):889–898, Nov. 2012. ISSN 1527-1404. doi: 10.2110/jsr.2012.73. URL https://pubs.geoscienceworld.org/jsedres/article/82/11/889-898/330506.

K. M. Straub, C. Paola, D. Mohrig, M. A. Wolinsky, and T. George. Compensational Stacking of Channelized Sedimentary Deposits. *Journal of Sedimentary Research*, 79 (9):673–688, Sept. 2009. ISSN 1527-1404. doi: 10.2110/jsr.2009.070. URL https://pubs.geoscienceworld.org/jsedres/article/79/9/673-688/145275.

K. M. Straub, R. A. Duller, B. Z. Foreman, and E. A. Hajek. Buffered, Incomplete, and Shredded: The Challenges of Reading an Imperfect Stratigraphic Record. *Journal of Geophysical Research: Earth Surface*, 125(3), Mar. 2020. ISSN 2169-9003, 2169-9011. doi: 10.1029/2019JF005079. URL https://onlinelibrary.wiley.com/doi/abs/10.1029/2019JF005079.

T. Sun, P. Meakin, T. Jøssang, and K. Schwarz. A Simulation Model for Meandering Rivers. *Water Resources Research*, 32(9):2937–2954, Apr. 1996. ISSN 00431397. doi: 10.1029/96WR00998. URL http://doi.wiley.com/10.1029/96WR00998.

K. A. Sundell. Sedimentation and tectonics of the Absaroka Basin of northwestern Wyoming. In: Wyoming sedimentation and Tectonics. *41st Annual Field Conference Guidebook*, page 18, 1990.

J. P. Syvitski, M. D. Morehead, D. B. Bahr, and T. Mulder. Estimating fluvial sediment transport: The rating parameters. *Water Resources Research*, 36(9):2747–2760, Sept. 2000. ISSN 00431397. doi: 10.1029/2000WR900133. URL http://doi.wiley.com/10.1029/2000WR900133.

S. C. Toby, R. A. Duller, S. De Angelis, and K. M. Straub. A Stratigraphic Framework for the Preservation and Shredding of Environmental Signals. *Geophysical Research Letters*, 46(11):5837–5845, June 2019. ISSN 0094-8276, 1944-8007. doi: 10.1029/2019GL082555. URL https://onlinelibrary.wiley.com/doi/abs/10.1029/2019GL082555.

S. M. Trampush, E. A. Hajek, K. M. Straub, and E. P. Chamberlin. Identifying autogenic sedimentation in fluvial-deltaic stratigraphy: Evaluating the effect of outcrop-quality data on the compensation statistic: Identifying Autogenic Sedimentation. *Journal of Geophysical Research: Earth Surface*, 122(1):91–113, Jan. 2017. ISSN 21699003. doi: 10.1002/2016JF004067. URL http://doi.wiley.com/10.1002/2016JF004067.

J. Tresch and A. Strasser. Allogenic and autogenic processes combined in the formation of shallow-water carbonate sequences (Middle Berriasian, Swiss and French Jura Mountains). *Swiss Journal of Geosciences*, 104(2):299–322, Oct. 2011. ISSN 1661-8734. doi: 10.1007/s00015-011-0064-2. URL https://sjg.springeropen.com/articles/10.1007/s00015-011-0064-2. Number: 2 Publisher: SpringerOpen.

J. van den Berg, A. Martinius, and R. Houthuys. Breaching-related turbidites in fluvial and estuarine channels: Examples from outcrop and core and implications to reservoir models. *Marine and Petroleum Geology*, 82:178–205, Apr. 2017. ISSN 02648172. doi:

10.1016/j.marpetgeo.2017.02.005. URL https://linkinghub.elsevier.com/retrieve/pii/S0264817217300442.

B. van der Meulen, P. D. Gingerich, L. J. Lourens, N. Meijer, S. van Broekhuizen, S. van Ginneken, and H. A. Abels. Carbon isotope and mammal recovery from extreme greenhouse warming at the Paleocene–Eocene boundary in astronomically-calibrated fluvial strata, Bighorn Basin, Wyoming, USA. *Earth and Planetary Science Letters*, 534: 116044, Mar. 2020. ISSN 0012821X. doi: 10.1016/j.epsl.2019.116044. URL https://linkinghub.elsevier.com/retrieve/pii/S0012821X19307393.

J. Vandenberghe. Timescales, climate and river development. *Quaternary Science Reviews*, 14(6):631–638, Jan. 1995. ISSN 02773791. doi: 10.1016/0277-3791(95)00043-O. URL https://linkinghub.elsevier.com/retrieve/pii/0277379195000430.

J. Vandenberghe. Climate forcing of fluvial system development: an evolution of ideas. *Quaternary Science Reviews*, 22(20):2053–2060, Oct. 2003. ISSN 02773791. doi: 10. 1016/S0277-3791(03)00213-0. URL https://linkinghub.elsevier.com/retrieve/pii/S0277379103002130.

S. Vaughan, R. J. Bailey, and D. G. Smith. Detecting cycles in stratigraphic data: Spectral analysis in the presence of red noise. *Paleoceanography*, 26(4):2011PA002195, Dec. 2011. ISSN 0883-8305, 1944-9186. doi: 10.1029/2011PA002195. URL https://onlinelibrary.wiley.com/doi/abs/10.1029/2011PA002195.

C. Wang, R. Adriaens, H. Hanlie, J. Elsen, N. Vandenberghe, L. Lourens, P. Gingerich, and H. Abels. Clay mineralogical constraints on weathering in response to early Eocene hyperthermal events in the Bighorn Basin, Wyoming (Western Interior, USA). *Geological Society of America Bulletin*, 129:B31515.1, Apr. 2017. doi: 10.1130/B31515.1.

Y. Wang, K. M. Straub, and E. A. Hajek. Scale-dependent compensational stacking: An estimate of autogenic time scales in channelized sedimentary deposits. *Geology*, 39(9):811–814, Sept. 2011. ISSN 1943-2682, 0091-7613. doi: 10. 1130/G32068.1. URL http://pubs.geoscienceworld.org/geology/article/39/9/811/130638/Scaledependent-compensational-stacking-An-estimate.

Y. Wang, T. Baars, H. Sahoo, J. Storms, A. Martinius, P. Gingerich, and H. Abels. Sandstone body character, river styles, and geomorphology of the lower Eocene Willwood Formation, Bighorn Basin, Wyoming, USA. July 2021a. URL https://eartharxiv.org/repository/view/2550/. Publisher: EarthArXiv.

Y. Wang, T. Baars, J. Storms, A. Martinius, P. Gingerich, M. Chmielewska, S. Buckley, and H. Abels. Spatial characteristics and kinematics of precession-driven floodplain aggradation cycles in the lower Eocene Willwood Formation of the Bighorn Basin, Wyoming, USA. June 2021b. URL https://eartharxiv.org/repository/view/2427/. Publisher: EarthArXiv.

Y. Wang, J. E. A. Storms, A. W. Martinius, D. Karssenberg, and H. A. Abels. Evaluating alluvial stratigraphic response to cyclic and non-cyclic upstream forcing through process-based alluvial architecture modelling. *Basin Research*,

33(1):48–65, 2021c. ISSN 1365-2117. doi: https://doi.org/10.1111/bre.12454. URL https://onlinelibrary.wiley.com/doi/abs/10.1111/bre.12454. _eprint: https://onlinelibrary.wiley.com/doi/pdf/10.1111/bre.12454.

Z. Wang, Y. Shen, A. Licht, and C. Huang. Cyclostratigraphy and Magnetostratigraphy of the Middle Miocene Ashigong Formation, Guide Basin, China, and Its Implications for the Paleoclimatic Evolution of NE Tibet. *Paleoceanography and Paleoclimatology*, 33(10):1066–1085, Oct. 2018. ISSN 25724517. doi: 10.1029/2018PA003409. URL http://doi.wiley.com/10.1029/2018PA003409.

G. S. Weissmann, A. J. Hartley, L. A. Scuderi, G. J. Nichols, A. Owen, S. Wright, A. L. Felicia, F. Holland, and F. M. L. Anaya. Fluvial geomorphic elements in modern sedimentary basins and their potential preservation in the rock record: A review. *Geomorphology*, 250:187–219, Dec. 2015. ISSN 0169-555X. doi: 10.1016/j.geomorph.2015.09.005. URL http://www.sciencedirect.com/science/article/pii/S0169555X15301409.

D. J. Went and W. J. McMahon. Fluvial products and processes before the evolution of land plants: Evidence from the lower Cambrian Series Rouge, English Channel region. *Sedimentology*, 65(7):2559–2594, 2018. ISSN 1365-3091. doi: 10.1111/sed.12478. URL https://onlinelibrary.wiley.com/doi/abs/10.1111/sed.12478. _eprint: https://onlinelibrary.wiley.com/doi/pdf/10.1111/sed.12478.

T. Westerhold, U. Röhl, J. Laskar, I. Raffi, J. Bowles, L. J. Lourens, and J. C. Zachos. On the duration of magnetochrons C24r and C25n and the timing of early Eocene global warming events: Implications from the Ocean Drilling Program Leg 208 Walvis Ridge depth transect. *Paleoceanography*, 22 (2), 2007. ISSN 1944-9186. doi: https://doi.org/10.1029/2006PA001322. URL https://agupubs.onlinelibrary.wiley.com/doi/abs/10.1029/2006PA001322. _eprint: https://agupubs.onlinelibrary.wiley.com/doi/pdf/10.1029/2006PA001322.

T. Westerhold, U. Röhl, B. Donner, H. K. McCarren, and J. C. Zachos. A complete high-resolution Paleocene benthic stable isotope record for the central Pacific (ODP Site 1209): Paleocene benthic stable isotope record. *Paleoceanography*, 26(2):n/a–n/a, June 2011. ISSN 08838305. doi: 10.1029/2010PA002092. URL http://doi.wiley.com/10.1029/2010PA002092.

T. Westerhold, U. Röhl, R. H. Wilkens, P. D. Gingerich, W. C. Clyde, S. L. Wing, G. J. Bowen, and M. J. Kraus. Synchronizing early Eocene deep-sea and continental records – cyclostratigraphic age models for the Bighorn Basin Coring Project drill cores. *Climate of the Past*, 14(3):303–319, Mar. 2018. ISSN 1814-9332. doi: 10.5194/cp-14-303-2018. URL https://cp.copernicus.org/articles/14/303/2018/.

T. Westerhold, N. Marwan, A. J. Drury, D. Liebrand, C. Agnini, E. Anagnostou, J. Barnet, S. Bohaty, D. De Vleeschouwer, F. Fabio, T. Frederichs, D. Hodell, A. Holbourn, D. Kroon, V. Lauretano, K. Littler, L. Lourens, M. Lyle, H. Pälike, and J. Zachos. An astronomically dated record of Earth's climate and its predictability over the last 66 million years. *Science (New York, N.Y.)*, 369:1383–1387, Sept. 2020. doi: 10.1126/science.aba6853.

K. Whipple, G. Parker, C. Paola, and D. Mohrig. Channel Dynamics, Sediment Transport, and the Slope of Alluvial Fans: Experimental Study. *The Journal of Geology*, 106(6):677–694, Nov. 1998. ISSN 0022-1376, 1537-5269. doi: 10.1086/516053. URL https://www.journals.uchicago.edu/doi/10.1086/516053.

K. X. Whipple. Fluvial Landscape Response Time: How Plausible Is Steady-State Denudation? *American Journal of Science*, 301(4-5):313–325, Apr. 2001. ISSN 0002-9599, 1945-452X. doi: 10.2475/ajs.301.4-5.313. URL http://www.ajsonline.org/lookup/doi/10.2475/ajs.301.4-5.313.

K. X. Whipple and G. E. Tucker. Implications of sediment-flux-dependent river incision models for landscape evolution. *Journal of Geophysical Research*, 107(B2):2039, 2002. ISSN 0148-0227. doi: 10.1029/2000JB000044. URL http://doi.wiley.com/10.1029/2000JB000044.

A. C. Whittaker and S. J. Boulton. Tectonic and climatic controls on knickpoint retreat rates and landscape response times: controls on landscape response time. *Journal of Geophysical Research: Earth Surface*, 117(F2):n/a–n/a, June 2012. ISSN 01480227. doi: 10.1029/2011JF002157. URL http://doi.wiley.com/10.1029/2011JF002157.

S. D. Willett, S. W. McCoy, J. T. Perron, L. Goren, and C.-Y. Chen. Dynamic Reorganization of River Basins. *Science*, 343(6175):1248765–1248765, Mar. 2014. ISSN 0036-8075, 1095-9203. doi: 10.1126/science.1248765. URL https://www.sciencemag.org/lookup/doi/10.1126/science.1248765.

G. P. Williams. River meanders and channel size. *Journal of Hydrology*, 88(1):147–164, Nov. 1986. ISSN 0022-1694. doi: 10.1016/0022-1694(86)90202-7. URL https://www.sciencedirect.com/science/article/pii/0022169486902027.

S. Wing and T. M. Bown. Fine Scale Reconstruction of Late Paleocene-Early Eocene Paleogeography in the Bighorn Basin of Northern Wyoming. page 13, 1985.

D. U. Wise. Laramide Structures in Basement and Cover of the Beartooth Uplift Near Red Lodge, Montana. *AAPG Bulletin*, 84, 2000. ISSN 0149-1423. doi: 10.1306/C9EBCDF1-1735-11D7-8645000102C1865D. URL http://search.datapages.com/data/doi/10.1306/C9EBCDF1-1735-11D7-8645000102C1865D.

W. A. Yonkee and A. B. Weil. Tectonic evolution of the Sevier and Laramide belts within the North American Cordillera orogenic system. *Earth-Science Reviews*, 150:531–593, Nov. 2015. ISSN 0012-8252. doi: 10.1016/j.earscirev.2015.08.001. URL http://www.sciencedirect.com/science/article/pii/S0012825215300258.

R. F. Yuretich, L. J. Hickey, B. P. Gregson, and Y.-L. Hsia. Lacustrine Deposits in the Paleocene Fort Union Formation, Northern Bighorn Basin, Montana. page 17, 1984.

J. C. Zachos, H. McCarren, B. Murphy, U. Röhl, and T. Westerhold. Tempo and scale of late Paleocene and early Eocene carbon isotope cycles: Implications for the origin of hyperthermals. *Earth and Planetary Science Letters*, 299(1):242–249, Oct. 2010. ISSN 0012-821X. doi: 10.1016/j.epsl.2010.09.004. URL https://www.sciencedirect.com/science/article/pii/S0012821X10005650.

R. E. Zeebe and L. J. Lourens. Solar System chaos and the Paleocene–Eocene boundary age constrained by geology and astronomy. *Science*, 365(6456):926–929, Aug. 2019. ISSN 0036-8075, 1095-9203. doi: 10.1126/science.aax0612. URL https://www.sciencemag.org/lookup/doi/10.1126/science.aax0612.

J. Zhang, J. Covault, M. Pyrcz, G. Sharman, C. Carvajal, and K. Milliken. Quantifying sediment supply to continental margins: Application to the Paleogene Wilcox Group, Gulf of Mexico. *AAPG Bulletin*, 102(09):1685–1702, Sept. 2018. ISSN 0149-1423. doi: 10.1306/01081817308. URL http://archives.datapages.com/data/doi/10.1306/01081817308.

Y. Zhang, M. Person, C. Paola, C. W. Gable, X.-H. Wen, and J. M. Davis. Geostatistical analysis of an experimental stratigraphy: geostatistical analysis of experimental stratigraphy. *Water Resources Research*, 41(11), Nov. 2005. ISSN 00431397. doi: 10.1029/2004WR003756. URL http://doi.wiley.com/10.1029/2004WR003756.

Curriculum Vitæ

Youwei Wang

31-05-1990   Born in Weihai, China

Education

2009-2013   BSc in Earth Sciences,
China University of Petroleum (Beijing)

2013-2016   MSc in Geological Resources and Geological Engineering,
China University of Petroleum (Beijing)

2016-2021   PhD in Applied Geology,
Delft University of Technology

Acknowledgments

Looking back the fiver-year PhD journey, I feel grateful to many people's help from various perspectives.

First of all, I would like to thank my promotor Allard Martinius for teaching me sedimentology and stratigraphy hands by hands both in the field and indoor. I appreciate your efforts that contribute to my field work in the Spanish Pyrenees Ainsa Basin. We spend tens of days together in Wyoming, and many of our ideas are sparkled there. I also want to thank you for introducing me to your friends to expand my network while we were in Quebec, Canada.

Then, my thanks go to my supervisor Hemmo Abels for accepting me as his first PhD student at Delft. Hemmo, I appreciate your continuous encouragement to promote me as an independent, objective, and brave researcher. I like your personality of being nice, considerate, and humorous, and I view you as more a friend than a supervisor. I am privileged to have weekly discussions with you in my first two years, which are really helpful for me to start my career in the realm of fluvial cyclostratigraphy. I feel fortunate to take many challenges that you have suggested, and now I really value the progress I have made. Also thank you for including me in the Norwegian Equinor ROBUST project.

My sincere gratitude goes to Joep Storms who have helped me on all the chapters to keep the contents clean and objective. Besides field geology, your background in hydrodynamics and numerical modelling guide me through a unique way, which helps me learn more about the power and weakness of models and thus enables me to apply them better.

My three visits to the Bighorn Basin, Wyoming, are more than perfect, where I spent more than 10 weeks in three successive years. I wish to first thank Philip Gingerich for his knowledge based on his 50-year experience in the basin and help in offering us all kinds of logistic support. I really enjoy all the conversations with you, Philip, on the fossils and mammal evolution besides the astronomical cycles. When I was infected by some unknown plants, you rushed me to the emergency at the hospital, which is really appreciated. I also would like to thank Holly for her company, which makes us feel at home after days of hard work in the Peaks.

The field work was enjoyable due to the company by many friends. I would like to first thank Chaowen Wang for helping me in many ways. We work hard together in the field, and we cook good Chinese dinner that Philip even made a toast! My thanks also go to Dirk-Jan Walstra for his company and humor in the field. Hiranya Sahoo, thank you for helping me to characterize sandstone bodies in the Peaks, and I am also glad to fly the drone for you to prepare for the photogrammetric model. I like your Indian-style cooking, although you claimed you never did that at home. Tim Baars, you are the buddy I communicate with most in both field and office time. Your joining in the group brings a lot of fun and knowledge. We were worrying about each other while we were working alone in hills without phone reception. We prepared decent FRESCO reports and wrote cool papers together. Magda Chmielewska, thank you for your hard work that contributes

to the beautiful drone model that helps me a lot. I also want to thank the Churchill family for helping us from various aspects and hosting us for the last dinner of every year's field campaign. You are all cool fossil hunters while extremely skilled in farming.

My special thanks go to my Dissertation Committee for providing sharp and constructive suggestions. Thank you, Chris, Esther, Giovanni, Gary, and Klaudia, and I definitely learn a lot from your comments. I would like to thank Frits Hilgen for allowing me to take his course–Astronomical Climate Forcing and Time Scales, which helps a lot in the first year of my Ph.D. although the final exam is super difficult! I also want to thank Imran Hasan for leading me more efficiently in the programming world that combines geological modelling and Python-based GIS techniques. Collaboration with Derek Karssenberg on the alluvial numerical modelling is exciting and inspiring. Thank you, Derek, for helping me from various aspects. My gratitude goes to Kyle Straub for critically reviewing my first paper and coming up with a lot of questions that help better constrain my model setup. Communications with Simon Buckley from the very beginning of LIME operation are pleasant and fruitful, which contributes to the results in the third chapter.

Being in the PROMS group is always enjoyable. I appreciate all the meetings with Helena, Maria, Aulia, Remi, Akeel, Emillio, Alam, Andrea, and other field crews I have mentioned above. Weekly FAMOUS meeting is another wonderful stage to interact with fluvial guys on outcrops, modelling, and subsurface cases. I also want to thank three master students I have guided, Abenezier Feleke, Jasper de Lanoy, and Tess Oude Essink, for exploring many interesting topics with me. My thank also goes to the section head Giovanni Bertotti for continuously encouraging me to finish my book as soon as possible.

Our working conditions are carefully maintained and continuously improved by the support staff. Thank you, Ralf, Marlijn, Margot, Marijke, Lydia, Myrthe, Anke,and Nancy!

During the journey of five years at Delft, I am grateful to have many nice colleagues with me, including Alex, Amin, Anne, Atsushi, Aukje, Baptise, Billy, Bingkun, Boris, Carlos, Chris, Cong, Diego, Feng, Florencia, Gill, Hamed, Helena, Iris, Jan-Willem, Jan-Kees, Jiakun, Jianhuan, Jingming, Jinyu, Joery, Johno, Junhai, Karim, Karlien, Kevin, Koen, Lele, Liang, Lisanne, Martha, Matteo, Max, Menno, Milad, Musab, Myrna, Navid, Nicolas, Pierre-Olver, Quinten, Rahul, Ranjani, Reuben, Rick, Runhai, Samantha, Santosh, Shahar, Shan, Shohei, Shotaro, Siddarth, Sixue, Stephen, Xu, Yang, Youhei, and Yuhang.

I appreciate the encouragement from my former supervisors: Xiongqi Pang, Dongxia Chen, and Fujie Jiang. I also benefit a lot from discussion with my senior fellows: Chenliang, Fengtao, Haipeng, Hongbo, Jianguo, Jigang, Jinyu, Junhui, Pengwei, Weilong, Yingchun, and Senlin. Special thanks go to Suihong Song for his help on reservoir modelling and geostatistics and hosting me for a few days at Stanford University. Our friendship of a decade never fades thanks to your continuous dirty jokes.

Almost finally, I thank my elder sister, Jing, to take care of our parents while I am abroad for study. I appreciate the unselfish and unconditional support from my parents, although I may not explicitly express this to you in person. Lastly, I would like to thank Didi for her persistent encouragement and love through this long journey. I look forward to our upcoming adventure in Virginia.

Youwei Wang
Delft, April 2021

List of Publications

Journal Publications of This Project

4. **Y. Wang**, T.F. Baars, J.E.A. Storms, A.W. Martinius, P.D. Gingerich, H.A. Abels, *Variation of Fluvial Styles in a Climatically-Controlled Stratigraphy in the Lower Eocene Willwood Formation, Bighorn Basin, Wyoming, USA*, In preparation for *Geology*.

3. **Y. Wang**, T.F. Baars, H. Sahoo, J.E.A. Storms, A.W. Martinius, P.D. Gingerich, H.A. Abels, *Characterization and classification of fluvial deposits in the lower Eocene Willwood Formation, Bighorn Basin, Wyoming, USA*, Submitted to *Sedimentology*.

2. **Y. Wang**, T.F. Baars, J.E.A. Storms, A.W. Martinius, P.D. Gingerich, M. Chmielewska, S.J. Buckley, H.A. Abels, *Spatial persistency and variability of precession-driven floodplain aggradational cycles in the lower Eocene Willwood Formation of the Bighorn Basin, Wyoming, USA*, Submitted to *Earth and Planetary Science Letter*.

1. **Y. Wang**, J.E.A. Storms, A.W. Martinius, D. Karssenberg, H.A. Abels (2021) *Evaluating alluvial stratigraphic response to cyclic and non-cyclic upstream forcing through process-based alluvial architecture modelling*, *Basin Research*, 33, 48-65.

Conference Proceedings

8. T.F. Baars, **Y. Wang**, A.W. Martinius, H.A. Abels. *Implementation of astronomical climate forcing in subsurface predictive models for floodplain-rich, low N/G alluvial stratigraphy*, 35th IAS Meeting of Sedimentology, Prague, Czech Republic, 2021.

7. **Y. Wang**, T.F. Baars, J.E.A. Storms, A.W. Martinius, H.A. Abels. *Tracing paleosols in a UAV-based photogrammetric model of alluvial stratigraphy in the Bighorn Basin, Wyoming*, 35th IAS Meeting of Sedimentology, Prague, Czech Republic, 2021.

6. H.A. Abels, T.F. Baars, **Y. Wang**, A. Akeel, J.E.A. Storms, A.W. Martinus. *Implementing Orbital Climate Control on Alluvial Stratigraphy in Subsurface Predictive Models*, 82nd EAGE Annual Conference & Exhibition, Amsterdam, The Netherlands, 2020.

5. H.A. Abels, **Y. Wang**, T.F. Baars, A. Alharbi, J.E.A. Storms, A.W. Martinius. *Precession-driven river avulsion cycles shaping alluvial architecture in the interaction with autogenic depositional controls*, IAS, Rome, Italy, 2019.

4. H. Sahoo, **Y. Wang**, J.E.A. Storms, H.A. Abels, and A.W. Martinius. *Alluvial analysis of the Palaeocene-Eocene Thermal Maximum: Bighorn Basin, Wyoming, USA*. IAS, Rome, Italy, 2019.

3. **Y. Wang**, J.E.A. Storms, D. Karssenberg, A.W. Martinius, H.A. Abels. *Numerical modeling of precession–driven deposition and erosion in alluvial settings: Analogue to the lower Eocene Willwood Formation of the Bighorn Basin, Wyoming, USA*. NAC, Utrecht, The Netherlands, 2019.

2. **Y. Wang**, H.A. Abels, J.E.A. Storms, A.W. Martinius. *Modelling orbital climate signals in fluvial stratigraphy.* ISC Quebec, Canada, 2018.

1. **Y. Wang**, J.E.A. Storms, A.W. Martinius, D. Karssenberg, H.A. Abels. *Testing the impact of astronomical climate forcing on fluvial architecture in process-based numerical modelling.* IAS meeting, Toulouse, France, 2017.

Journal Publications Outside This Project

6. J. Zhang, Z. Jiang, H. Wu, T.F. Baars, **Y. Wang**, H.A. Abels (2021) *Precession-dominance of middle Eocene east Asian climate: implication for mudrock deposition and shale reservoir quality,* AAPG, under revision

5. X. Pang, C. Jia, K. Zhang, M. Li, **Y. Wang**, J. Peng, B. Li, and J. Chen (2020) The dead line for oil and gas and implication for fossil resource prediction. Earth Syst. Sci. Data, 12, 577–590.

4. D. Chen, X. Pang, **Y. Wang**, Y. Dong, F. Jiang, L. Li, H. Pang, H. Bai, B. Pang, R. Qin, and H. Jiang (2019) *Palaeoenvironmental periodisms of middle Eocene terrestrial sediments in Bohai Bay Basin, eastern China, and their implications for organic matter accumulation.* Marine and Petroleum Geology, 104060.

3. H. Huang, W. Sun, W. Ji, R. Zhang, K. Du, S. Zhang, D. Ren, **Y. Wang**, L. Chen, X. Zhang (2018) *Effects of pore-throat structure on gas permeability in the tight sandstone reservoirs of the Upper Triassic Yanchang formation in the Western Ordos Basin, China.* Journal of Petroleum Science and Engineering, 162, 602–616.

2. W. Peng, G. Hu, **Y. Wang**, D. Liu, Y. Lv, X. Luo (2018b) *Geochemical characteristics of light hydrocarbons and their influencing factors in natural gases of the Kuqa Depression, Tarim Basin, NW China.* Geological Journal, 53, 2863–2873.

1. W. Peng, G. Hu, Z. Feng, D. Liu, **Y. Wang**, Y. Lv, R. Zhao (2018a) *Origin of Paleogene natural gases and discussion of abnormal carbon isotopic composition of heavy alkanes in the Liaohe Basin, NE China.* Marine and Petroleum Geology, 92, 670–684.

Datasets

1. **Y. Wang**, J.E.A. Storms, A.W. Martinius, D. Karssenberg, H.A. Abels (2020) *Evaluating alluvial stratigraphic response to cyclic and non-cyclic upstream forcing through process-based alluvial architecture modelling,* 4TU.Center for Research Data.